Investigations of Surface Reconstructions and Inverse Stranski Krastanov Growth in InGaAs Films

by

Lee E Sears

A dissertation submitted in partial fulfillment
of the requirements for the degree of
Doctor of Philosophy
(Materials Science and Engineering)
in The University of Michigan
2009

Doctoral Committee:

Associate Professor Joanna Mirecki Millunchick, Chair
Associate Professor Roy Clarke
Associate Professor Christopher A. Pearson
Assistant Professor Anton van der Ven

Lee E. Sears

© ________________________ 2009

All Rights Reserved

Acknowledgements

First of all I would like to thank God, without whom nothing is possible. I also would like to thank my family, in particular my mother and father for instilling in me the value of an education and the financial and moral support to pursue my wildest dreams unencumbered by the constrains often felt by so many African Americans. I could have never done any of this without their constant motivation. Their pride in what I have accomplished pushes me to be a better person every day.

I am grateful and blessed to have had such an intelligent, understanding, beautiful and supportive wife by my side throughout my entire postsecondary career. Brenda was there to encourage me when I questioned my ability to be an engineer, she stayed up with me during the numerous late nights while pursuing my degrees, and she was there to make me laugh when the only thing I wanted to do was cry. My parents helped me get into a position to succeed, but it is my wife who ensured that I successfully made it through. Brenda, I love you more than words can express and I am eternally grateful to you for just being the wonderful person that you are and my soulmate.

I would like to extend my gratitude to my colleagues in Dr. Joanna Mirecki Millunchick's lab for helping me to understand the many things that I had no clue about when I first entered this doctoral program. Thank you Dr. Catalina Dorin for encouraging me to join the Millunchick research group when I came to visit the department of Materials Science and Engineering. At the time I could not fully comprehend how important it was to pick the "right" research group and research advisor, but in the years since joining this group I have learned that I probably would not have successfully made it through this experience as a member of any other group. I would also like to thank Dr. Alex Riposan for helping me learn how to use the MBE equipment and how to successfully grow InGaAs films. I owe a debt of gratitude to Dr. Chris Pearson and Dr. Alex Riposan for their patience in teaching me everything that I know about using the STM to produce high quality images. I would like to thank Dr. Benny Perez Rodriguez for being a friend to me in the lab and passing along his experience and advice to me. He brought clarity to the often confusing world of graduate research and I will always consider him my friend.

I would also like to thank all of the current members of Dr. Joanna Mirecki Millunchick's research group and in particular Jessica Bickel, John Thomas, and Kevin Grossklaus for helping out with all of the MBE related tasks and for also being my friends, I will never forget you guys (and gal). I would also like to send a special shout out to Tacarra Andrade for being there

to help me acclimate to Michigan and helping me have a good time and get my mind off academia. We were good friends in undergrad and I feel as though I am leaving Michigan with a great friend for life. Lastly I would like to thank my beagle Kali for her unquestioned love and obedience, she is the best canine pal that I have ever had.

TABLE OF CONTENTS

Acknowledgements ii
List of Figures vii
List of Tables xiii
List of Appendices xiv
Chapter 1. Introduction 1
Chapter 2. Experimental Techniques and Procedures 7
Chapter 3. Coexistence of Surface Reconstruction Domains on Strained Heteroepitaxial Films 20
3.1 Introduction 20
3.2 Background 22
3.3 Experimental procedure 41
3.4 Coexistence of surface reconstructions on $In_{0.81}Ga_{0.19}As$/InP(001) films 45
3.4.1 Dependence on film thickness 50
3.4.2 Dependence on growth temperature 55
3.4.3 Summary of results 57
3.5 Discussion 60
3.5.1 Strain relief in $In_{0.81}Ga_{0.19}As$/InP(001) films 60
3.5.2 Influence of surface morphology on coexistence 64
3.6 Conclusions 68
Chapter 4. Thermodynamic Model of the Coexistence of (nx3) and β2(2x4) Reconstructions 69
4.1 Introduction 69
4.2 Background 71
4.3 Experimental procedure 77
4.4 Thermodynamic model 78
4.5 Discussion 82
4.5.1 Importance of elastic relaxation in the thermodynamic model 83
4.5.2 Anisotropy in the boundary energy term 88
4.6 Conclusion 92

Chapter 5. Pit Nucleation During the Growth of Compressively Strained $In_{0.81}Ga_{0.19}As$/InP(001) Layers 93
5.1 Introduction 93
5.2 Background 95
5.3 Experimental procedure 106
5.4 Pit nucleation during the growth of $In_{0.81}Ga_{0.19}As$/InP(001) layers 107
5.4.1 Dependence on film thickness 108
5.4.2 Dependence on growth temperature 114
5.4.3 Dependence on growth rate 116
5.5 Discussion 118
5.6 Conclusions 124
Chapter 6. Summary and Conclusions 126
Appendices 129
References 145

List of Figures

Figure

2.1 Polishing/Etching setup [25] 10

2.2 SEM image of the apex of the STM tip [25] 11

2.3 STM Image of the β2(2x4) reconstructions highlighted using SPIP image analysis software. 17

2.4 RHEED oscillations 18

3.1: (a) Side view of the β2(2x4) reconstruction and (b) a top view of the same reconstruction. Both the topmost arsenic (empty sphere) layer and the second (cation) layer are incomplete, and the former one contains two As-As dimers with their bond axis oriented along the $(1\bar{1}0)$ direction. The dimer bonds are shown in black. The incomplete surface layer results in trenches running in the $(1\bar{1}0)$ direction where As atoms from the third layer are visible and form a third As-As dimer (seen in top view).[33] 24

3.2 200 Å x 200 Å STM image of the surface of $In_{0.27}Ga_{0.73}As(001)$ showing the β2(2x4) reconstruction. [43] 25

3.3 Ball and stick model of the (2x3) reconstruction unit cell as proposed by Sauvage-Simkin.[17] 27

3.4 (a) RHEED patterns after deposition of the $In_{0.53}Ga_{0.47}As$ film. (b)-(c) STM images of the surface of the same film grown at T = 465 °C, R = 0.5 ML/s, F_{As} = 2 ML/s, and V/III ratio = 4. The RHEED pattern shows a (4x3) and this is confirmed by STM images showing a (4x3)

reconstruction with a 4a spacing in the $[1\bar{1}0]$ and a 3a spacing along the [110].[18] 29

3.5 Ball and stick model of the (4x3) reconstruction unit cell in agreement with the RHEED and STM images shown in Fig. 3.4.[18] 31

3.6 STM image of $In_{0.81}Ga_{0.19}As$ showing that the surface is comprised of areas of β2(2x4) surrounded by a disordered matrix of (4x3). 32

3.7 Temperature dependence of indium surface segregation length on strained $In_xGa_{1-x}As$ films. The dashed lines are guides to the eye.[56] 34

3.8 (a) RHEED oscillations of $In_{0.2}Ga_{0.8}As$ grown on GaAs at 520 °C. Dashed lines represent the best fits of the maxima of the RHEED data.[62] (b) RHEED intensity data during the deposition of $In_{0.2}Ga_{0.8}As$ films grown at different temperatures, as noted.[62] 36

3.9 AFM images of $In_{0.1}Ga_{0.9}As$/GaAs(001) showing the surface morphologies above the critical thickness for film grown at 450 °C. 40

3.10 RHEED oscillations showing the film was grown to a thickness of 20 ML at a growth rate of 1.1 ML/sec. 43

3.11 Omega-2theta scan confirming that the $In_{0.53}Ga_{0.47}As$ buffer layer is latticed matched to the InP(001) substrate. RADS simulation data confirms peak at -2400 arcsecs corresponds to an $In_xGa_{1-x}As$ films with a x=0.81 indium composition. 45

3.12 (a) Filled state in vacuo 500 x 500 Å STM (-2.99 V, 100 pA) image of a h=40 ML $In_{0.81}Ga_{0.19}As$/InP film deposited at T=475°C, R=0.5 ML/s, F_{As4}=2.5 ML/s, and V/III flux ratio=5. (4x3)/(nx3) reconstructions are denoted by hash marks with regions of β(2x4) domains of circled. (b) Line scan of the surface of the $In_{0.81}Ga_{0.19}As$ indicated by the black hashed line on the STM image in part (a). 47

3.13 RHEED patterns after the deposition of latticed matched $In_{0.53}Ga_{0.47}As$/InP exhibiting a weak (4x3) reconstruction (A) and $In_{0.81}Ga_{0.19}As$ immediately after growth (B) and upon cooling (C) showing a (2x4) reconstruction. 49

3.14 Filled states STM images of several 20 ML thick $In_{0.81}Ga_{0.19}As$ films used in analyzing the β2(2x4) surface coverage. 52

3.15 In situ STM (-2.88 V, 100 pA) images of $In_{0.81}Ga_{0.19}As$/InP. If growth temperature is kept constant and the total thickness of the $In_{0.81}Ga_{0.19}As$ layer is allowed to vary from 10 ML $< h < 60$ ML, a mixture of (4x3)/(nx3) and β2(2x4) are observed on the growing surface. All sample were grown with T= 495 °C, R_{Ga}= 0.5 ML/s, and V/III flux= 4 (after twenty minute anneal). 54

3.16 In situ STM (-2.88 V, 100 pA) images of $In_{0.81}Ga_{0.19}As$/InP. Temperature is the only growth condition varied from 465 °C $\leq T \leq$ 515 °C. A mixture of (4x3)/(nx3) and β2(2x4) domains are stable on the growing surface of $In_{0.81}Ga_{0.19}As$/InP(001) across a range of growth temperature. All samples are 10 ML thick with R_{Ga}= 0.5 ML/s, and V/III flux= 4 (after five minute anneal). 56

3.17 A plot of the β2(2x4) surface coverage as a function of film thickness and growth temperature. The dashed lines are guides for the eye with different temperatures highlighted in different colors to better illustrate the β2(2x4) coverage pattern. 59

3.18 RHEED intensity oscillation for $In_{0.81}Ga_{0.19}As$ films grown at 485 °C (blue dashed oscillations at top) and 505 °C (solid red oscillations at bottom). The magnitude of the decay in intensity oscillations for films grown at 505 °C is greater than the magnitude of decay in intensity oscillations for films grown at 485 °C. 63

3.19 Plot of the surface coverage of the β2(2x4) reconstructions (blue) and surface roughness data (red) for $In_{0.81}Ga_{0.19}As$

films. AFM micrographs of the surface at 20 ML and 70 ML are also shown. 66

4.1 Image of the surface of Si(111) showing a (7x7) domain in a (1x1) background on large step-free terraces. The difference in surface stress between the two domains results in force monopoles at the phase boundaries (arrows).[19] 72

4.2 Graph of the area of a rectangular shaped domain versus length or width derived using Eqn. 4.2. Small domains have a square geometry but above a critical size the shape will always transform into a rectangle of width *s* and length *t*.[19] 75

4.3 STM image of $In_{0.81}Ga_{0.19}As$ showing that the surface is comprised of areas of β2(2x4) surrounded by a disordered matrix of (4x3). 79

4.4 Schematic of a rectangular shaped reconstruction in a background matrix of a dissimilar reconstruction. 82

4.5 (a) Contour plot of the total free energy as a function of the domain width and length for $\Delta\gamma$=1 meV/Å^2, β=1 meV/Å, F_0=10 meV/Å. The darker shades represent lower total free energies. (b) Plot of the total free energy as a function of the length (or width) for increasing domain areas (D=20 Å^2, 55 Å^2, 100 Å^2). These values were chosen arbitrarily in order to illustrate the behavior of these equations. Black squares and gray triangles on the plot indicate where the domain shape is square and rectangular, respectively. 85

4.6 (a) Contour plot of the total free energy as a function of the domain width and length for $\Delta\gamma$=1 meV/Å^2, β=1 meV/Å, F_0=30 meV/Å. The darker shades represent lower total free energies. (b) Plot of the total free energy as a function of the length (or width) for increasing domain areas (D=20 Å^2, 55 Å^2, 100 Å^2). These values were chosen arbitrarily in order to illustrate the behavior of these equations. Black squares and gray triangles on the plot indicate where the domain shape is square and rectangular, respectively. 87

4.7 Plot of the experimental data (dots) for the dependence of the length and width of the domains as a function of area for films deposited at T=505°C, R_{Ga}= 0.5 ML/s, h=20 ML, and V/III flux= 5. The solid line was produced using the model for isotropic domains with $\Delta\gamma$=1 meV/Å^2, β_x=1 meV/Å, β_y=1 meV/Å, F_0=30 meV/Å, a=1.9 Å, ν=0.3. Dashed lines were produced using the model for anisotropic boundary energies ($B_{x/}$ B_y=10 and $B_{x/}$ B_y=30). 89

4.8 Plot of the boundary energy anisotropy as a function of growth temperature. The points were obtained by fitting the experimental data to Eqn. 4.5, assuming that $\Delta\gamma$=1 meV/Å^2, β_y=1 meV/Å and F_0=30 meV/Å. 91

5.1 3D AFM image of pits forming on the surface of $In_{0.25}Ga_{0.75}As$ /GaAs(001) above t_{SK}.[91] 97

5.2 Cross-sectional view of the shape assumed for islands or pits on the surface of moderately strained films above t_{SK}. Length and height are denoted by s and h, respectively. Edges are oriented at an angle θ with respect to the surface of the film.[88] 98

5.3 1x1 μm AFM images of $In_{0.27}Ga_{0.73}As$/GaAs films grown at grown at T=485°C, R=1.1 ML/s, and V/III flux ratio=4 at film thicknesses as noted. The height scale is 15 nm for (a) and (b) and 20 nm for (c).[95] 100

5.4 Graph showing the variation of the adatom concentration η between two islands separated by a distance 2*l*, as a function of position.[87] 102

5.5 Graph showing predicted domains of several morphological regimes as a function of surface and strain energy. Two experimental systems are denoted for comparison, $In_{0.27}Ga_{0.73}As$/GaAs and InSb/InAs. The geometry of the pits is accounted for in the evaluation of the surface energy. [87] 104

5.6 Graph showing various predicted morphology regimes as a function of growth temperature and deposition rate.[87] 105

5.7 A series of 1x1μm AFM images comparing the development of the surface morphology on the surface of $In_{0.81}Ga_{0.19}As$ grown at T=515°C, R=1.2 ML/s, and V/III flux ratio=4 for various thicknesses as noted. Dashed line (b) denotes the location of line scan shown in Fig. 5.8. 111

5.8 Line scan of the island and pits denoted by the dashed line in Fig. 5.7(b). Facets are indicated in blue. 113

5.9 Cross-sectional TEM image of a 0.5 μm thick $In_{0.81}Ga_{0.19}As$ layer grown at T=505°C, R=1.2 ML/s, and V/III flux r atio=4. 114

5.10 1x1μm AFM images of $In_{0.81}Ga_{0.19}As$ films grown at h=60 ML, R=1.2 ML/s, and V/III flux ratio=4, for (a) T=475°C (b) T=495°C (c) T=505°C. 116

5.11 1x1μm AFM images of $In_{0.81}Ga_{0.19}As$ films grown at T=505°C, h=55 ML, and V/III flux ratio=4, for (a) R=0.5 ML/sec and (b) R=1.25ML/sec. 117

5.12 Plot of the lattice parameter obtained by measuring the separation of the RHEED diffraction rods during the deposition of an $In_{0.81}Ga_{0.19}As$ film grown at T=475 °C and R=1.2 ML/sec. Arrows denote the beginning and end of growth. Inset is a 1x1μm AFM image taken after growth showing pits on the surface of this sample. 121

5.13 Filled state (-2.88 V, 100 pA) 500 x 500 Å STM images of a h=50ML $In_{0.81}Ga_{0.19}As$/InP film deposited at T=505°C, R=0.5 ML/s, F_{As4}=2.2 ML/s, and V/III flux ratio=4. Images were taken (a) near island/pit formations and (b) isolated from any 3D growth. 123

List of Tables

Table

3.1 Details about the surface coverage of the β2(2x4) reconstructions shown in Fig 3.15 including the dimer length, domain area, and total surface coverage. 55

3.2 Details about the surface coverage of the β2(2x4) reconstructions shown in Fig 3.16 including the dimer length, domain area, and total surface coverage. 57

5.1 Comparison of islands on the surface of $In_{0.27}Ga_{0.73}As$ shown in Figure 5.3 (a)-(c). 109

5.2 Comparison of pits on the surface of $In_{0.81}Ga_{0.19}As$ shown in Figure 5.7. 111

5.3 Comparison of pits on the surface of $In_{0.81}Ga_{0.19}As$ shown in Figure 3. 116

5.4 Comparison of pits on the surface of $In_{0.81}Ga_{0.19}As$ shown in Figure 4. 118

List of Appendices

Appendix

A. Mathematica code for a thermodynamic model that outputs a contour plot of the total free energy as a function of the domain width and length. 129

B. Mathematica code for a thermodynamic model that outputs a contour plot of the total free energy as a function of 142

Chapter 1

Introduction

Ternary alloys such as $In_xGa_{1-x}As$ are important components of many electronic and optical devices.[1-3] Understanding surface reconstructions is an important aspect of controlling the quality of these devices because the type of domains present can alter the morphology and adversely affect the formation of abrupt heterointerfaces.[4] A lack of abrupt heterointerfaces can cause deviations in the composition profile in the direction of primary growth. This deviation may give rise to distortions of the conduction and valence band edge profiles and these distortions can adversely affect the desired properties of the device. Ternary alloys such as $In_xGa_{1-x}As$ are ideally suited for studying surface reconstructions because the composition of the resulting film can be altered allowing for the nucleation of many different types of surface reconstructions.

Surface reconstructions play a crucial role in the epitaxial growth of III-V compound semiconductors. Surface reconstructions occur when the surface atoms rearrange themselves in a way that minimizes the free energy of the

system. The free energy of the surface is high relative to the bulk due to the large density of dangling interatomic bonds with unpaired electrons. Most III-V compound semiconductors like GaAs ideally have a zinc-blend structure.[5] While one hybridized atom from each type combine, some hybrid atoms cannot form a bond at the surface. This leads to unreconstructed surfaces with unsaturated dangling bonds. In order to eliminate such dangling bonds, the surface undergoes complex reconstructions.[6] Annealing semiconductor surface at high temperature provides the energy necessary for the atoms to rearrange themselves and results in a variety of similar surface reconstructions.[5]

Extensive research has gone into understanding semiconductor surface reconstructions resulting in well over 100 experimental and theoretical reconstruction types.[6-12] From this research a set of general principles can be formulated in relation to semiconductor surface reconstructions. Of these the ones of most importance to this research include the principle that the surface reconstruction observed will be the lowest energy structure that is kinetically available under the conditions used for sample preparation.[11] Also, in many cases semiconducting surfaces can lower their energy via atomic relaxation.[11]

The goal of this work is the study of surface reconstructions on ternary alloy films. $In_xGa_{1-x}As$ is a convenient ternary alloy to study due to its importance in optoelectronic and heterojunction devices as well as the ability to grow this structure at multiple compositions and on different substrates including InAs, GaAs, and InP.[1, 13-15] The $In_{0.81}Ga_{0.19}As$ films possess a 1.9% lattice mismatch when grown on an InP substrate. This introduces enough strain to allow for the study of the effect of strain on the stability of surface reconstructions while not being so high that it severely hampers the range of growth temperatures and film thicknesses that can be studied prior to roughening in the film.

Although a large volume of research has gone into investigating surface reconstructions on binary III-V semiconductors, not nearly as much time has been spent studying these domains on ternary alloys such as $In_xGa_{1-x}As$. This can be problematic given the importance of $In_xGa_{1-x}As$ films in applications such as those mentioned previously. A parameter that is critical to the growth of these high quality devices is the presence of abrupt interfaces. Surface reconstructions are thought to affect the composition of the topmost layers due to surface segregation, although the exact mechanics remain unclear.[16, 17] One would not expect to see multiple domains coexisting on the surface of compound semiconductors, however there is evidence of this occurring.[18, 19] It is unclear what mechanisms allow for the coexistence of multiple

reconstruction domains although research indicates it could be related to either surface thermodynamics or film composition.[19, 20] The structural anisotropy of the reconstructions can affect the kinetic factors for adsorption, diffusion and desorption of different species. It is known that the anisotropy is related to residual strain in the film but the full effect of strain remains unclear. Finally, surface reconstructions have been shown affect the film morphology by providing nucleation points for islands but theoretically pits should also work as an initial stress relaxation mechanism.[21]

The aforementioned phenomena have not been consistently studied previously and represent the impetus of my investigation. As a result, the focus of this research entails the study of the coexistence of surface reconstruction domains on strained heteroepitaxial films (Chapter 3), a thermodynamic model of the coexistence of (nx3) and β2(2x4) reconstructions (Chapter 4), and pit nucleation during the growth of compressively strained $In_{0.81}Ga_{0.19}As$/InP(001) layers (Chapter 5). The ultimate goal of the research is to develop a quantitative understanding of the connection between surface reconstructions on $In_{0.81}Ga_{0.19}As$/InP and film thickness, growth conditions, surface energy, and morphological evolution. The content of this thesis is organized as follows:

Chapter 2 – "Experimental techniques and procedures" This chapter presents the process used to setup the experiments, as well as the general

experimental procedures used for analyzing the data. More details about specific experimental procedures are provided in each subsequent chapter as it relates to the specific experiments being discussed.

Chapter 3 – "Coexistence of Surface Reconstruction Domains on Strained Heteroepitaxial Films" The coexistence of β2(2x4) and (nx3) reconstructions on the surface of $In_{0.81}Ga_{0.19}As$ films is discussed in this chapter. Surfaces of $In_{0.81}Ga_{0.19}As$/InP thin films grown by molecular beam epitaxy (MBE) and imaged by *in vacuo* scanning tunneling microscopy (STM), was observed to consist of small anisotropic regions of a β2(2x4) reconstruction in a matrix of a disordered (nx3) reconstruction. The presence of β2(2x4) reconstructions is stable across a range of growth conditions, and surface coverage data indicates that film thickness and growth temperate may affect the nucleation and growth of the β2(2x4) reconstruction. Specifically, the surface coverage of the β2(2x4) was found to vary depending on the film thickness and it was observed that growth temperature also affects the β2(2x4) surface coverage. The dependence of these phenomena on surface morphology and indium segregation is discussed.

Chapter 4 – "Thermodynamic Model of the Coexistence of (nx3) and β2(2x4) Reconstructions" This chapter discusses the thermodynamics of the stability of β2(2x4) and (nx3) reconstructions on the growing surface of

$In_{0.81}Ga_{0.19}As/InP$. A thermodynamic model that incorporates elastic relaxation, unit strain energy, and anisotropy at the boundaries is used to determine the free energy on the surface. The shape and size distribution of these domains is consistent with anisotropic elastic relaxation at the domain boundaries. A correlation between the thermodynamic model and experimental results is also discussed.

Chapter 5 – "Pit Nucleation During the Growth of Compressively Strained $In_{0.81}Ga_{0.19}As/InP(001)$ Layers" This chapter presents new observations regarding the transition to three-dimensional (3D) growth for $In_{0.81}Ga_{0.19}As$ films grown on InP(001) substrates. In particular, thin films of $In_xGa_{1-x}As$ are observed to develop either islands or pits on the surface to relieve lattice mismatch strain after some critical thickness depending on the composition. A correlation between the film composition and the surface energy is presented. Once the pits form, their behavior is similar to that of islanding, resulting in an "inverse" Stranski Krastanov growth mode. Analysis of the atomic surface structure near and far away from formed pits is considered and correlated to island formation.

Chapter 6 – "Summary and Conclusions" This chapter summarizes the main results of this research and the conclusions reached therein.

Chapter 2

Experimental Techniques and Procedures

In this chapter the experimental techniques used for sample analysis as well as growth procedures are briefly discussed. More detailed information about specific techniques and procedures will be provided in subsequent chapters as needed.

Molecular Beam Epitaxy (MBE)

Molecular beam epitaxy is an extremely versatile tool used in the growth of metal, semiconducting, and insulating films.[22-24] Molecular beam refers to the unidirectional flow of the atoms of the individual elements that make up the film, while epitaxy describes the ordered deposition of the epilayer upon the substrate in a manner that results in the epilayer growing with the same crystalline orientation as the substrate. The high degree of precision in the control of the beam flux makes MBE ideal for electronic and optoelectronic device fabrication where precision growth is essential.

All samples discussed in this work were grown using a solid sourced EPI 930 MBE system equipped with Ga, In, As, Al, Sb, Bi, Si, and Be cells with

valved crackers for Sb and As. This MBE system consists of five main chambers: a load-lock sample introduction chamber, a growth chamber where film deposition occurs, an *in vacuo* scanning tunneling microscopy chamber, an *in vacuo* focused ion beam chamber, and a buffer chamber that is used transfer samples between the various chambers. A pressure of approximately 10^{-11} torr is maintained in the growth chamber using a Physical Electronics ion pump combined with a CTI Cryogenics High Vacuum cryo pump.

Scanning Tunneling Microscopy (STM)

Scanning tunneling microscopy (STM), based on the concept of quantum tunneling, can resolve electronic structures on an angstrom length scale on the solid surfaces of clean conducting materials.[5] STM is a short range order tool that has proven useful in the understanding of mixed reconstruction domains since the individual domains can be imaged and analyzed unlike long range order techniques such as RHEED.

The STM images used in this work are from a modified UHV-400 RHK beetle-type microscope. Initially, Pt-Ir tips manufactured by Materials Analytical Services were used without modification. Later, tungsten tips chemically etched on site were used employing an etching technique outlined later in this section. All samples analyzed using the STM are filled states images with a constant 100 pA current and bias voltages typically ranging

between -2.65 and -3.30 V. Scan sizes used for this work range from 200 to 5000 Å. Typical base pressures in the STM chamber during imaging ranged from $9x10^{-11}$ to $9x10^{-9}$ torr.

Etching of Tungsten Tips

This procedure is intended to produce sharper, more stable tips than the mechanically sharpened Pt-Ir tips commercially available from Materials Analytical Services. For this procedure the STM tips were made from 99.9% pure polycrystalline tungsten wire with a diameter of 0.25mm. The wires are initially cut to a length of 2 cm, long enough to ensure that the final etched STM tip is of sufficient length. The tungsten wires are then cleaned with acetone and deionized water to remove any residual oils from handling. Next, the tungsten wires are electropolished in a bath of 2M NaOH to remove the native oxide layer. The electropolishing occurs with the NaOH solution heated to 70-80 degrees while being mechanically agitated. A stainless steel ring is also placed in the solution to act as a cathode during electropolishing. The tungsten wires are placed in the center of the stainless steel ring to ensure an even electric field is applied and immersed 1.5 cm into the solution as shown in Figure 2.1.

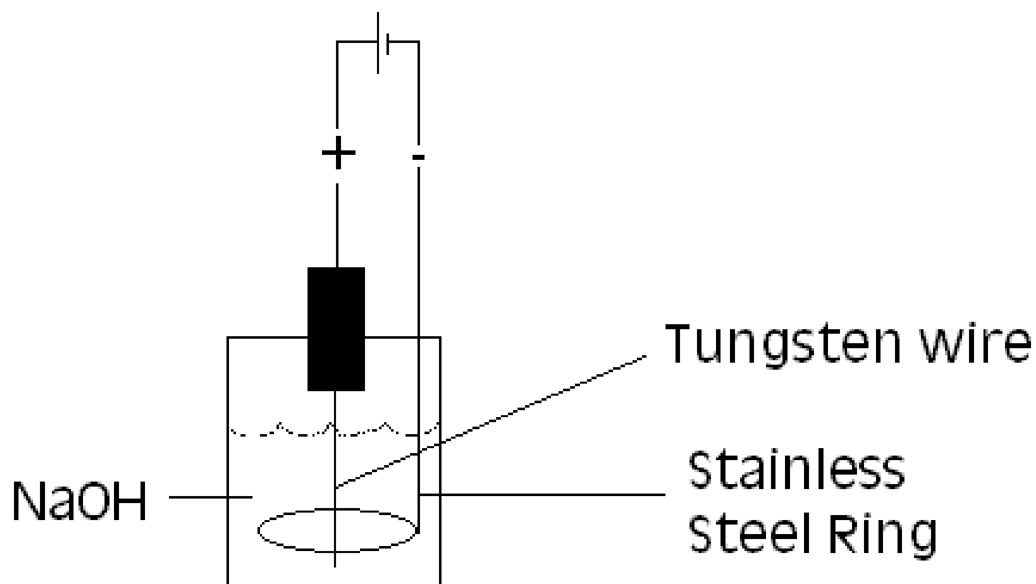

Figure 2.1: Polishing/Etching setup [25]

A 5 mA DC voltage is applied and the wires are allowed to polish for approximately 5 minutes. The outer surface of the tungsten wires will appear bright and shiny following this procedure if the native oxide layer has been successfully removed. This same technique is used in conjunction with shutoff circuitry to electrochemically etch the STM tips.[25]

This technique has been shown to produce STM tips with a radius of curvature of ~7 nm at the apex as shown in Figure 2.2.[25] The large radius of curvature is likely due to the reformation of the native oxide layer prior to SEM analysis and therefore should have a much smaller radius of curvature when

installed in the STM due to the shorter time period left at atmospheric pressure. Anecdotal evidence using these STM tip during the latter part of the research presented in this work indicated that the electrochemically etched tips are more stable and need less conditioning prior to use when scanning the surface of $In_{0.81}Ga_{0.19}As$ films.

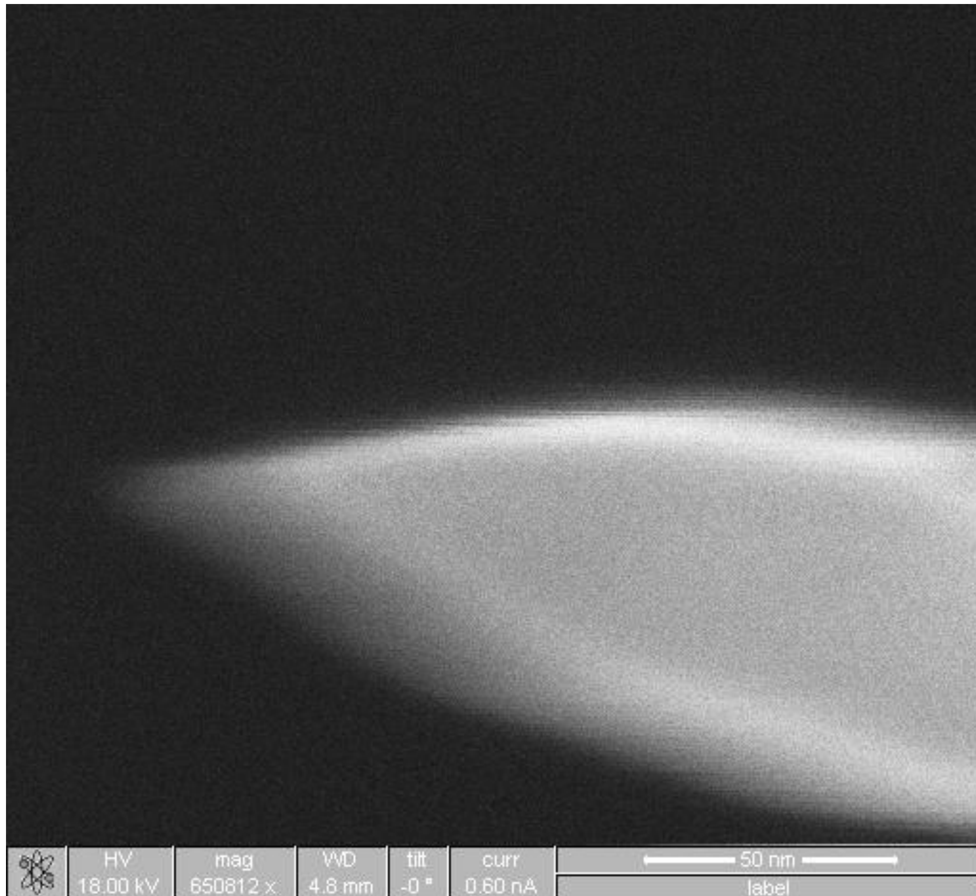

Figure 2.2: SEM image of the apex of the STM tip [25]

Reflection High Energy Electron Diffraction (RHEED)

Some information concerning the surface morphology, ordering, and sample growth rates was obtained using a RH15 Reflection high Energy electron Diffraction (RHEED) manufactured by Staib Instruments. Typical operating conditions are with the electron gun producing a high energy beam at 15 kV and 1.6 A.

Diffracted electrons interfere constructively at specific angles based on the surface structure and atomic spacing. Different reconstructions on the surface can be identified due to differences in the intensity of fractional order spots in the diffraction pattern. Phase diagrams using RHEED have been mapped out for several kinds of semiconducting materials including GaAs and InAs.[7, 26]

Despite the advantages of using RHEED to analyze surface reconstructions, there are drawbacks to this technique that limits its use. RHEED averages the surface structure over a relatively large area making it difficult to discern disorder on the surface as well as periodic changes in the atomic ordering due to the presence of more than one reconstruction. Furthermore, RHEED fails to describe the physical atomic surface structure.

The reconstructions found on the surface of ternary alloys are not well understood at this time. RHEED investigations looking at the surface of

$In_xGa_{1-x}As$ films have shown that the surface is comprised of commensurate (2x3) as well as incommensurate (2xn) diffraction patterns.[16] By assuming that the (2x3) reconstruction constitutes a uniform phase on the surface the author was able to conclude that the commensurate (2x3) surface composition was approximately $In_{0.67}Ga_{0.33}As$ while the incommensurate (2xn) phase appears as the (2x3) phase transitions to a c(4x4). However, this assumption is not necessarily true and several other models have also been suggested for this reconstruction.[27, 28]

X-Ray Diffraction (XRD)

Verification of the $In_{0.81}Ga_{0.19}As$ film's composition post growth was carried out using a Bede D1 High Resolution X-Ray Diffractometer. In this study omega-2theta scans were carried out over the (004). Dynamic simulations were used to fit the data and determine film composition and, in some cases, the strain relaxation in the film.

Atomic Force Microscopy (AFM)

Larger scale images of the surface of the $In_{0.81}Ga_{0.19}As$ films were obtained using a Digital Instruments NanoScope IIIa AFM in the tapping mode. Typical scan sizes were 1-10 μm. AFM measurements were used primarily to analyze surface morphology including roughening, islanding, and pitting.

Quantitative Determination of Feature Statistics

Analysis of the surface coverage of the β2(2x4) reconstructions on STM images was obtained using Image Metrology's Scanning Probe Image Processor (SPIP) software. This software is intended primarily for processing nano and micro scale microscopy. In order to process STM images for use in surface coverage analysis the raw SM3 file format native to RHK's XPMPro STM software must first be opened in SPIP. SPIP can read and process SM3 files so there is no need to convert the raw image file to another image format (e.g. tiff). Leaving the STM files in the SM3 format preserves scan area and z-depth information. Also, the ideal STM image will contain flat terraces with no step edges. Since the surface coverage technique used in SPIP relies on the fact that the β2(2x4) lies 1.5 Å above the (nx3) background the STM images with step edges will not be able to select β2(2x4) reconstructions sitting on the lower step.

After opening the SM3 file in SPIP the image must be flattened. Failure to properly flatten the image prior to processing will make it more difficult for the software to select the β2(2x4) domains and leads to more noise in the data. After flattening activate the grain analysis dialog window. In this window there are several grain analysis options that you must select from. Set the "segment type" to "grains" if analyzing β2(2x4) domains or "pores" if pits are

being processed. Then set the "detection method" to "threshold". In threshold mode only pixels that lie above the detection level if processing β2(2x4) domains or below the detection level if processing pits. The "detection level" defines the minimum z-value needed for a pixel to be regarded as part of a segment. Adjust the detection level until the domains of interest are highlighted. Alternatively, the domains can be selected by adjusting the color limit in the color scale editor. In grain mode the lower color limit of the color bar reflects the detection level and in pore mode the upper color limit marker indicates the threshold value.

Select the result dialog box to show size statistics related to the domains selected. The kinds of statistics shown can be selected in the preferences section. After selecting the optimal detection level there will likely still be some noise in the form of smaller features that are not part of the domains you are analyzing. Remove them by deselecting all data points in the results dialog box that have an area less than 1.28 nm^2, the area of a single β2(2x4) dimer as measured on a STM image using SPIP. There may also be a need to manually deselect certain larger features such as nucleating islands by setting the pointer to the "deselect" mode and clicking on the highlighted regions that need to be removed from the size statistics. The surface coverage data shown in the results dialog box is now ready to be analyzed. The overall surface coverage is given at the top of the dialog box and underneath this is more detailed size

information about the individual features selected. All of the data from the dialog box can be imported into a spreadsheet by pressing the "copy all" button at the top of the dialog box and pasting this data into the spreadsheet of your choice.

Figure 2.3 is a STM image with the β2(2x4) domains highlighted using SPIP. Even though all of the extraneous features highlighted in Fig. 2.3 are deselected in the results dialog box, they still remain highlighted on the image. These extra features include the nucleating island as well as small bits of the (nx3) background.

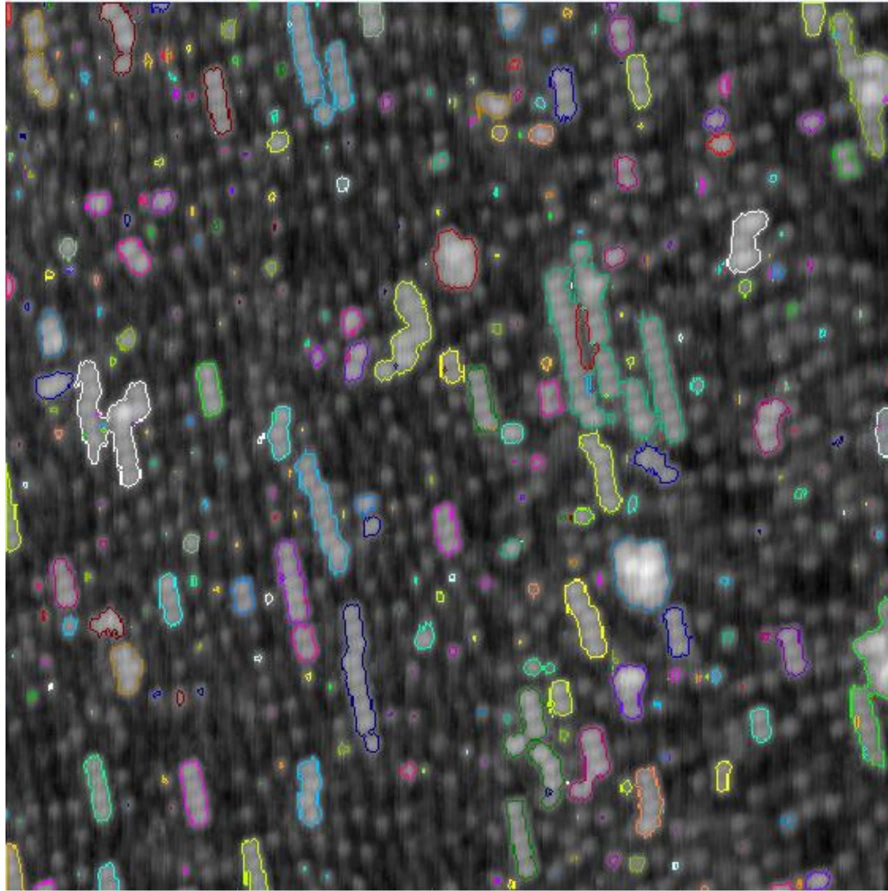

Figure 2.3: STM Image of the β2(2x4) reconstructions highlighted using SPIP image analysis software.

General Growth Procedures

Samples were grown using an EPI 930 molecular beam epitaxy system with solid source In and Ga cells and a valved cell for As_4. The growth rates were calibrated using RHEED intensity oscillations, and the growth temperature was monitored using a pyrometer, calibrated by observing the temperature at which the oxide desorption for an InP(001) substrate occurs.

The growth rate of each of the alloy components were calibrated using RHEED oscillations. All $In_{0.81}Ga_{0.19}As$ samples presented in this work are grown on top of a 0.5 µm thick $In_{0.53}Ga_{0.47}As$ buffer layer lattice matched to InP(001). This buffer layer is deposited at a total group III growth rate R=0.5 ML/s. Growth rates for the buffer layer are verified using RHEED intensity oscillations during deposition. An example of a typical set of RHEED intensity oscillations is shown in Figure 2.4.

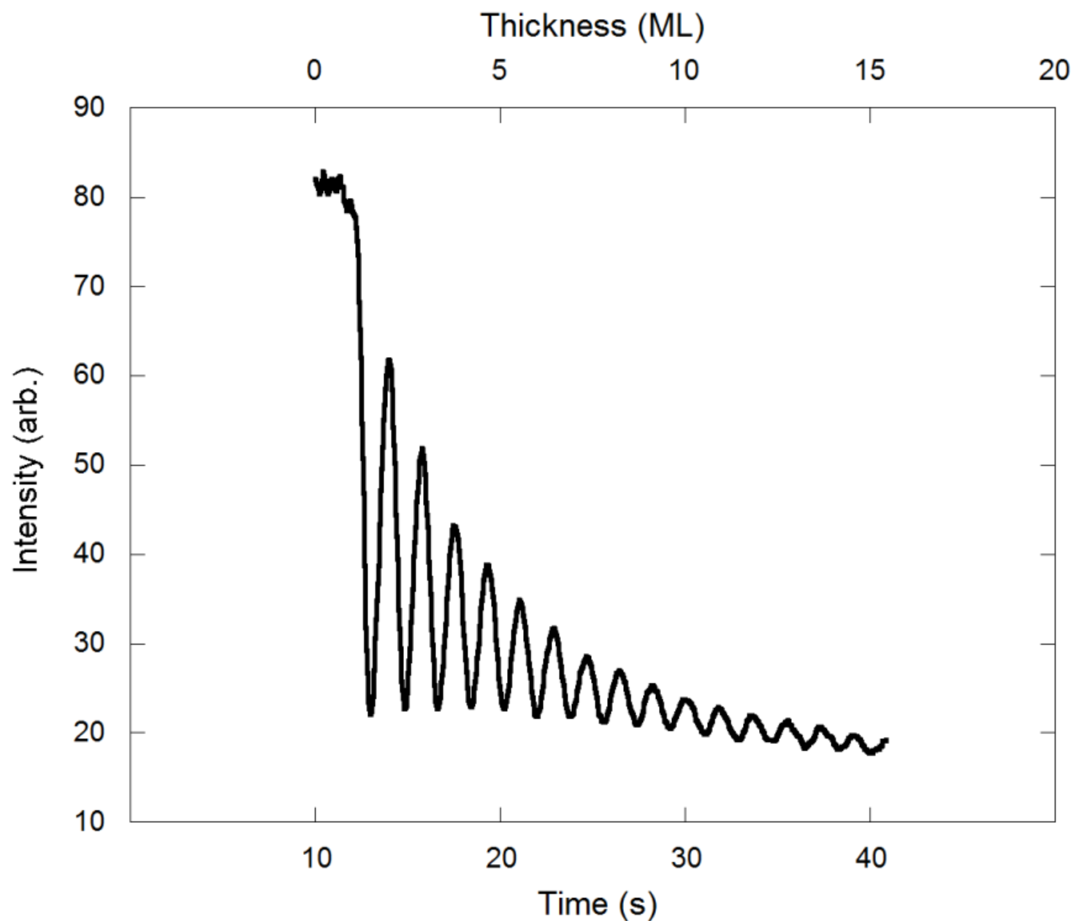

Figure 2.4: RHEED oscillations

After deposition of the buffer layer the sample was annealed for 25 minutes while ramping to the In cell temperature required for the deposition of an $In_{0.81}Ga_{0.19}As$ film. The $In_{0.81}Ga_{0.19}As$ films, which possess a lattice mismatch of 1.9% in compression with respect to the substrate, were grown to thicknesses $10<h<60$ ML, as noted. These films were also grown under conditions that maintained layer-by-layer growth ($465 \leq T \leq 515$°C, $0.5 \leq R \leq 1.1$ML/s, $2 \leq F_{As4} \leq 4$ML/s). At the end of growth, all samples were quenched under the same As_4 flux used during growth, after which the samples were transferred *in vacuo* to a STM. This procedure has been shown to result in a surface morphology that is planar with occasional 2D islands, having an RHEED pattern that possesses the same symmetry as during deposition.[29]

Chapter 3

Coexistence of Surface Reconstruction Domains on Strained Heteroepitaxial Films

3.1 Introduction

This chapter details the coexistence of reconstructions on the surface of $In_{0.81}Ga_{0.19}As$. Surface reconstructions play a crucial role in the epitaxial growth of III-V compound semiconductors. Understanding surface reconstructions is an important aspect of controlling the quality of electronic and optical devices because the type of domains present can alter the morphology and adversely affect the formation of abrupt heterointerfaces.[4] A lack of abrupt heterointerfaces can cause deviations in the composition profile in the direction of primary growth. This deviation may give rise to distortions of the conduction and valence band edge profiles and these distortions can adversely affect the desired properties of the device. Ternary alloys such as $In_xGa_{1-x}As$ are ideally suited for studying surface reconstructions because the composition of the resulting film can be altered allowing for the nucleation of many different types of surface reconstructions. Understanding

what types of reconstructions form on the surface and under what conditions will aid in the design of optoelectronic devices and increase production quality.

The primary goal of this work is to show that surfaces of $In_{0.81}Ga_{0.19}As/InP$ thin films grown by molecular beam epitaxy and imaged by *in vacuo* scanning tunneling microscopy, are observed to consist of small anisotropic regions of a β2(2x4) reconstruction in a matrix of a disordered (nx3) reconstruction. The presence of β2(2x4) is stable across a range of growth conditions, and surface coverage data indicates that film thickness and growth temperate may affect the nucleation and growth of the β2(2x4) reconstruction, indicating that film roughness and indium segregation length may play a role in domain stability and the resulting surface coverage of β2(2x4).

The contents of this chapter are organized in the following manner: **Section 3.2 ("Background")** discusses the β2(2x4) and (nx3) surface reconstructions and where they are most commonly found on semiconducting thin films. This section also discusses indium surface segregation on strained $In_xGa_{1-x}As$ alloys. **Section 3.3 ("Experimental Procedure")** details the methods used to grow high quality InGaAs films used for this study. **Section 3.4 ("Coexistence of surface reconstructions on $In_{0.81}Ga_{0.19}As/InP(001)$ films")** presents in detail the surface reconstructions seen on the 1.9% lattice

mismatched $In_{0.81}Ga_{0.19}As$ films when imaged using STM. Particular attention is given to the surface coverage of the β2(2x4) reconstruction and its dependence on growth temperature (Section 3.4.1) and total film thickness (Section 3.4.2). The results are summarized in Section 3.4.3. The experimental results from Section 3.4 are the discussed in detail in **Section 3.5 ("Discussion")** paying particular attention to the influence of indium segregation (Section 3.5.1) and surface morphology (Section 3.5.2) on the surface coverage of the β2(2x4). The main conclusions of this chapter are summarized in **Section 3.6 ("Conclusions")**.

3.2 Background

This section provides information regarding some of the reconstructions found on the surface of III-V semiconductors including under what conditions they appear. Proposed atomic structures are discussed and related to STM images of the surface. This section also provides information relevant to phenomena observed in mismatched films including segregation and surface roughening.

The effect of strain on the formation of surface reconstructions is not well understood. The $In_xGa_{1-x}As$/InP system is an ideal way to study growth the effect of strain on surface reconstructions because samples can be grown either lattice matched to the substrate or with a lattice mismatch that is either

positive (tensively strained) or negative (compressively strained). 25 ML of $In_{0.27}Ga_{0.73}As$ was grown on GaAs(001) resulting in films possessing a 1.9% lattice mismatch.[29] This film resulted in the coexistence of two different reconstructions on the surface, namely α2(2x4) and (4x3) reconstructions. $In_{0.81}Ga_{0.19}As$ films of the same thickness grown on InP(001) also shows two different reconstructions on the surface, a β2(2x4) and a disordered (nx3) that is similar to those found on (4x3) reconstructed surfaces observed for III-Sb(001) binary compounds.

The β2(2x4) is a reconstruction commonly found on binary surfaces such as InAs or GaAs.[30-32] The β2(2x4) structure consists of two As dimers in the top atomic layer and one As dimer in the second sublayer per unit cell.[32] Figure 3.1 shows the side and top view of a ball-and-stick model for the β2(2x4) reconstruction. Both the topmost arsenic layer and the second cation layer are incomplete, and the former one contains two As-As dimers with their bond axis oriented along the $(1\bar{1}0)$ direction. The incomplete surface layer results in trenches running in the $(1\bar{1}0)$ direction where As atoms from the third layer are visible and form a third As-As dimer that can be seen in Fig. 3.1b.[33]

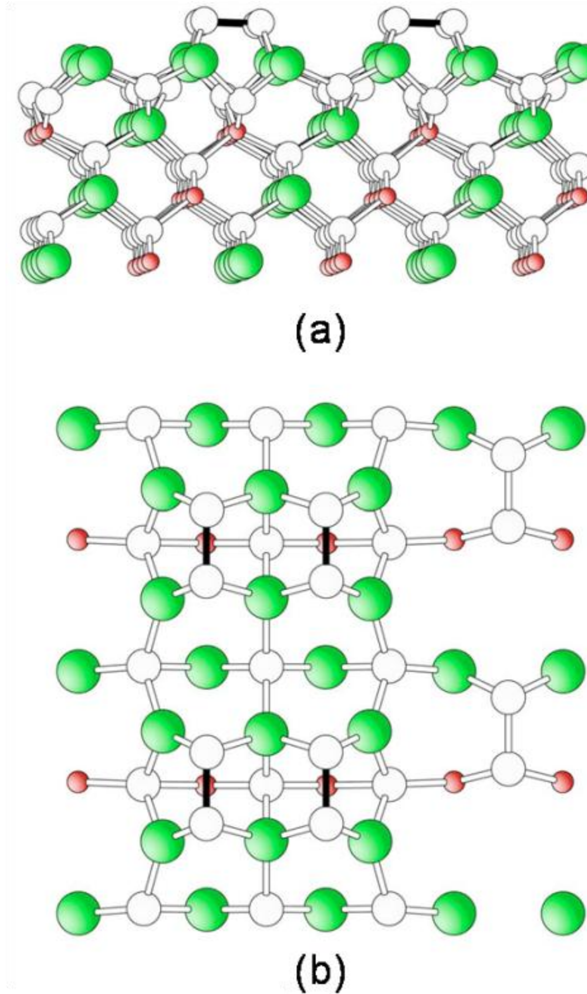

Figure 3.1: (a) Side view of the β2(2x4) reconstruction and (b) a top view of the same reconstruction. Both the topmost arsenic (empty sphere) layer and the second (cation) layer are incomplete, and the former one contains two As-As dimers with their bond axis oriented along the $[1\bar{1}0]$. The dimer bonds are shown in black. The incomplete surface layer results in trenches running in the $[1\bar{1}0]$ where As atoms from the third layer are visible and form a third As-As dimer (seen in top view).[33]

The β2(2x4) model was confirmed by STM, which showed the topmost row consisting of two As-As dimer separated by a row of two missing dimers. Figure 3.2 is a line scan and STM image of $In_{0.27}Ga_{0.73}As$/GaAs(001) showing the β2(2x4) reconstruction after growth. Line scans show that the β2(2x4) sits

on top of the background (nx3) reconstruction. This STM image clearly suggests that the β2(2x4) reconstruction consists of row of two As-As dimers separated by a rows of two missing As dimers. Figure 3.2 shows a faint dark line across the center of each cluster, which is indicative of the separation of the two dimers within each unit cell. The large white features are believed to be extra arsenic atoms condensed on the surface with missing dimer rows running parallel to the $[1\bar{1}0]$.[34] The β2(2x4) model was also later confirmed by X-ray diffraction and RHEED experiments, and was also found to be stable according to first principle calculations.[35-43]

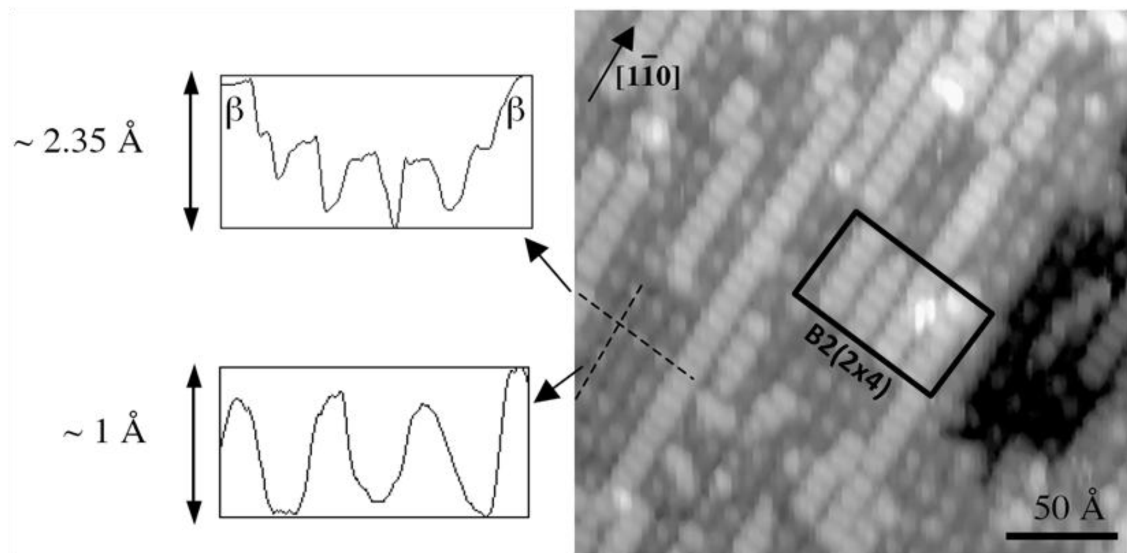

Figure 3.2: 200 Å x 200 Å STM image of the surface of $In_{0.27}Ga_{0.73}As$/GaAs(001) showing the β2(2x4) reconstruction.[44]

The (nx3) reconstruction is not well understood at this time although it is generally accepted that a x3 reconstruction is formed over a wide range of growth conditions on $In_xGa_{1-x}As$ surfaces.[28] One reconstruction model proposed primarily on the basis of XRD studies is a (2x3) model. This model, shown in figure 3.3, consists of a topmost layer of As dimers with the first cation layer having a composition of 67% indium and 33% gallium being fixed by a preferential occupancy.

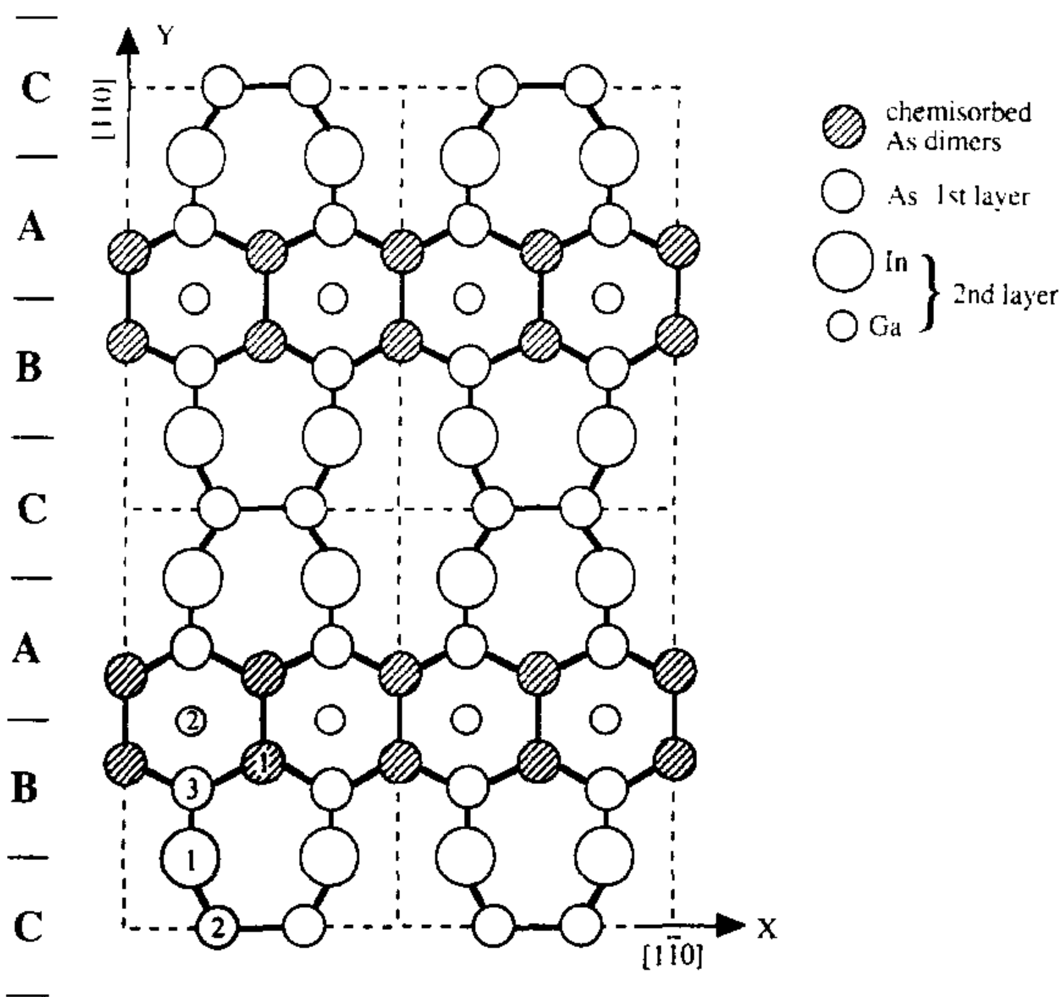

Figure 3.3: Ball and stick model of the (2x3) reconstruction unit cell as proposed by Sauvage-Simkin.[17]

Theoretical models such as ab initio calculation of the (2x3) reconstruction have found that this is the most stable among several reasonable 3x structures.[45] However, this model does not account for the high degree of local disorder found in STM images of the 3x surface and isn't consistent with

observations.[46] Furthermore, the (2x3) model does not obey the electron counting rule (ECR).[47]

A second x3 model based on a voltage dependent STM study proposes a disordered (4x3) structure with three cation-cation dimer rows in the upper layer and a cation-anion heterodimer offset by one surface unit spacing in the [110] direction. This unique alloy reconstruction is closely related to the (4x3) reconstructions observed on III-Sb(001) binary compounds.[48]

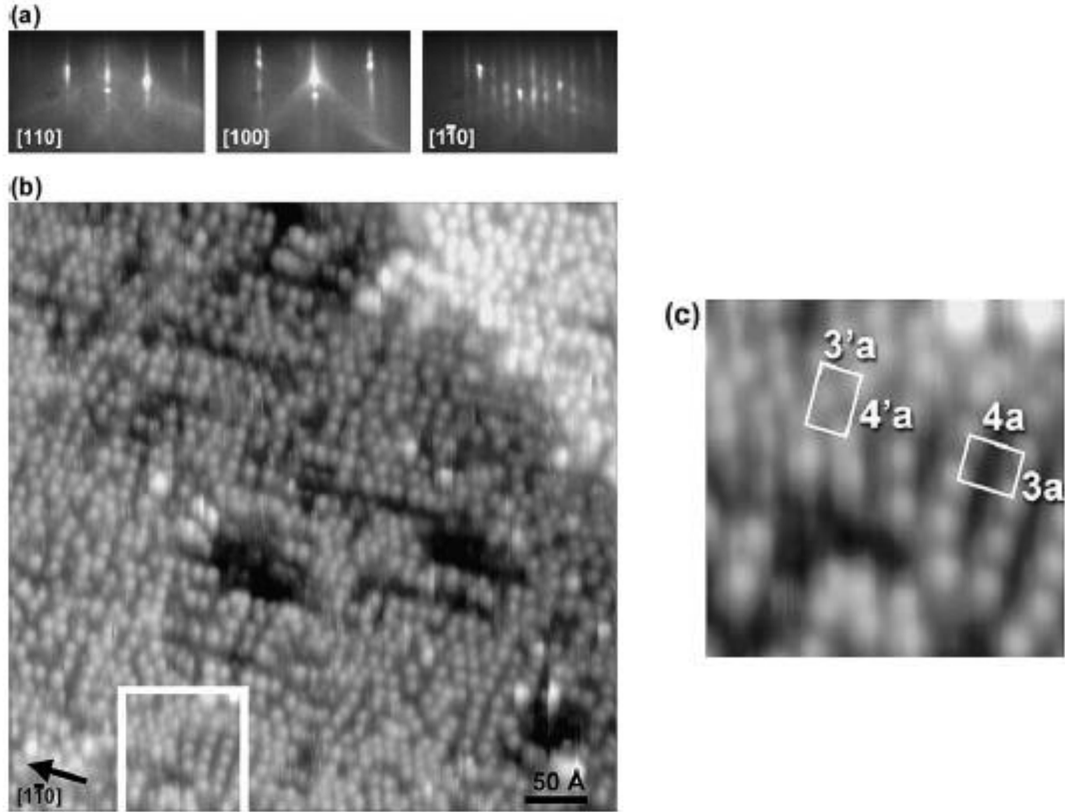

Figure 3.4: (a) RHEED patterns after deposition of the $In_{0.53}Ga_{0.47}As$ film. (b)-(c) STM images of the surface of the same film grown at T = 465 °C, R = 0.5 ML/s, F_{As} = 2 ML/s, and V/III ratio = 4. The RHEED pattern shows a (4x3) and this is confirmed by STM images showing a (4x3) reconstruction with a 4a spacing in the [$1\bar{1}0$] and a 3a spacing along the [110].[18]

Figure 3.4 shows the RHEED pattern and STM images of an $In_{0.53}Ga_{0.47}As$ film that is lattice matched to the InP(001) substrate. The RHEED pattern shows very weak streaks separated by a d/4 spacing in the [110] direction, where d is the spacing of the primary diffraction rods. The RHEED pattern in the [$1\bar{1}0$] azimuth exhibits very strong streaks separated by a d/3 spacing. The filled states (-2.3 V, 100 pA) STM images shown in Fig. 3.4 (b)-(c) shows a highly disordered array of equiaxed spots with some local

symmetry apparent upon closer inspection in Fig. 3.4(c). In particular, there is a reconstruction domain that possesses a 4a spacing along the $[1\bar{1}0]$ and a 3a spacing in the [110], where a = 4.1 Å is the bulk lattice spacing along the {110} family of directions.[18] This arrangement forms the (4x3) pattern observed by RHEED.

Figure 3.5 is a proposed ball and stick model for the disordered (4x3) reconstruction shown in Fig. 3.4 with some atoms omitted for clarity. The small black atoms are the bulk As, the white are the bulk metal, the larger black atoms are the surface As, and the white crosshatched atoms are the surface metal. In this model the (4x3) structure contains three cation-cation dimer rows in the topmost layer, with a cation-anion heterodimer offset by one surface unit spacing in the [110] direction.[18] The raised dot features observed in the STM image in Fig. 3.4 are produced by the heterodimer. This model is in agreement with observed RHEED and STM images and also obeys the electron counting rule while allowing for semiconducting surfaces. However, questions have been raised about the energy costs related to forming metal dimers in an arsenic rich environment.[49]

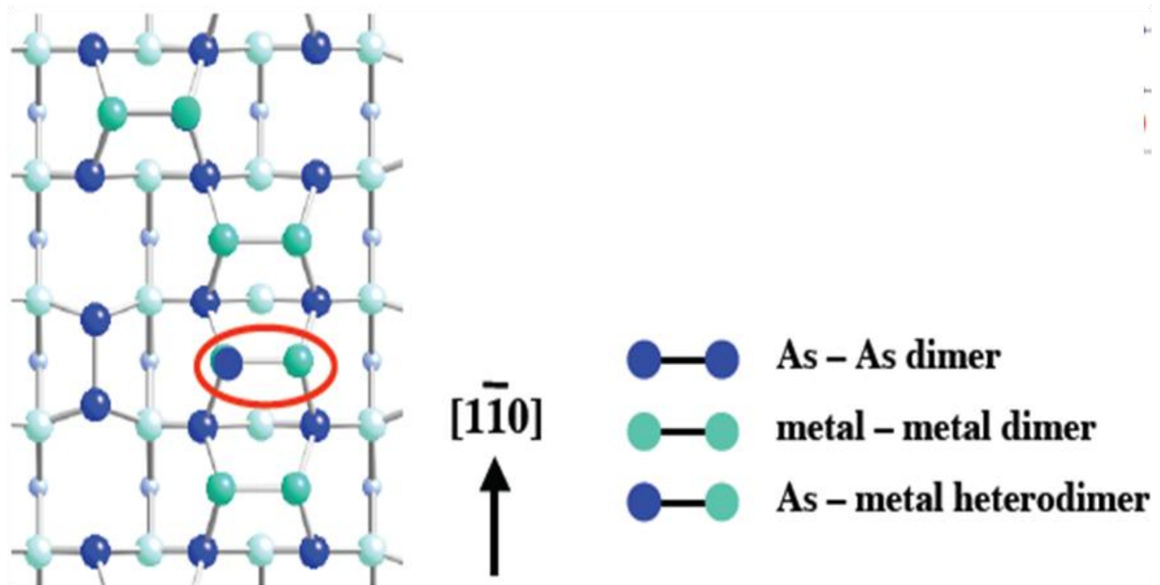

Figure 3.5: Ball and stick model of the (4x3) reconstruction unit cell in agreement with the RHEED and STM images shown in Fig. 3.4.[44]

Recently, surfaces of $In_xGa_{1-x}As$ have been observed with multiple reconstruction domains coexisting on the surface. In the case of $In_{0.27}Ga_{0.73}As$/GaAs(001), the surface contains a mixture of disordered (4x3) and α2(2x4) reconstructions.[29] These reconstructions are stable on the surface across a wide range of film thicknesses. The stability of the surface reconstructions with increasing film thickness was attributed to indium enrichment of the surface via indium segregation as well as strain.[29]

Changing the indium composition significantly alters the types of reconstructions present on the growing surface. Figure 3.6 shows a filled state (-3.15 V, 100pA) STM image of a 25 ML thick $In_{0.81}Ga_{0.19}As$/InP film grown

at T = 465 °C, R = 1.1 ML/s, F_{As4} = 2.4 ML/s, and V/III flux ratio = 2.2. The $In_{0.81}Ga_{0.19}As$/InP(001) film is observed with multiple reconstruction types coexisting on the surface, but in this case the α2(2x4) seen on the surface of $In_{0.27}Ga_{0.73}As$ is replaced with β2(2x4) reconstructions on the surface of the $In_{0.81}Ga_{0.19}As$ films.[18] This β2(2x4) reconstruction is one of the most pronounced features on the surface comprising 55% of the surface. Defects along the rows such as kinks or trench-filling defects are also occasionally observed.

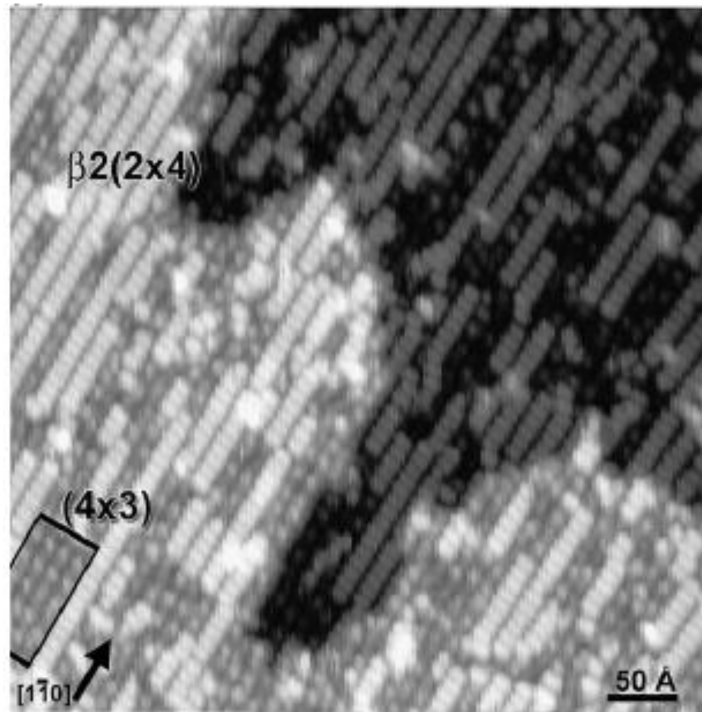

Figure 3.6: STM image of $In_{0.81}Ga_{0.19}As$ showing that the surface is comprised of areas of β2(2x4) surrounded by a disordered matrix of (4x3).[18]

Surface segregation is an important fundamental problem in materials science since it is vital to understanding the atomic scale structure and roughness of III–V heterostructure interfaces. Surface segregation can affect the composition profile of thin epitaxial layers of ternary and quaternary III-V compounds resulting in a deviation from abrupt interfaces.[50] Segregation is the process where binding and elastic energy differences between different atomic species from the same periodic group, and between surface and bulk sites, result in the migration to the surface of one species.[51] This results in the enrichment of the growth surface by a given species relative to the bulk and a delayed incorporation of the species at the onset of a ternary compound growth[52, 53]. Many attempts have been made, both experimentally[54-58] and theoretically[59-61], to understand the mechanisms and general trends in surface segregation. However, a high sensitivity of segregation to the growth conditions, temperature, V-III ratio, strain in the epitaxial layer due to lattice constant mismatch and a large number of factors influencing this process make it difficult to describe the segregation adequately.[62] In the MBE growth of III–V compound semiconductors containing indium, it has been reported that a considerable amount of In segregates at the surface.[50]

Recent studies suggest the presence of β2(2x4) on the surface is related to indium segregation from the sublayer to the surface.[58] Surface segregation in strained $In_xGa_{1-x}As$ films has been shown to lead to an enrichment of indium

at the surface relative to the bulk composition.[29, 50, 51, 62] Experimental evidence suggests that the indium segregation length in strained $In_xGa_{1-x}As$ films is related to the growth temperature. Figure 3.7 summarizes the temperature dependence of the In surface segregation length obtained using secondary-ion mass spectroscopy (SIMS). The In segregation length decreases with decreasing growth temperature due to the kinetically limited exchange of atoms from the bulk to the surface.[57] Indium desorption, as seen from the integrated ion count of SIMS, was also observed to decrease by an order of magnitude above 500 °C for $In_xGa_{1-x}As$ films grown with a V/III ratio = 4 in this study. This is most likely due to indium desorption from the surface.

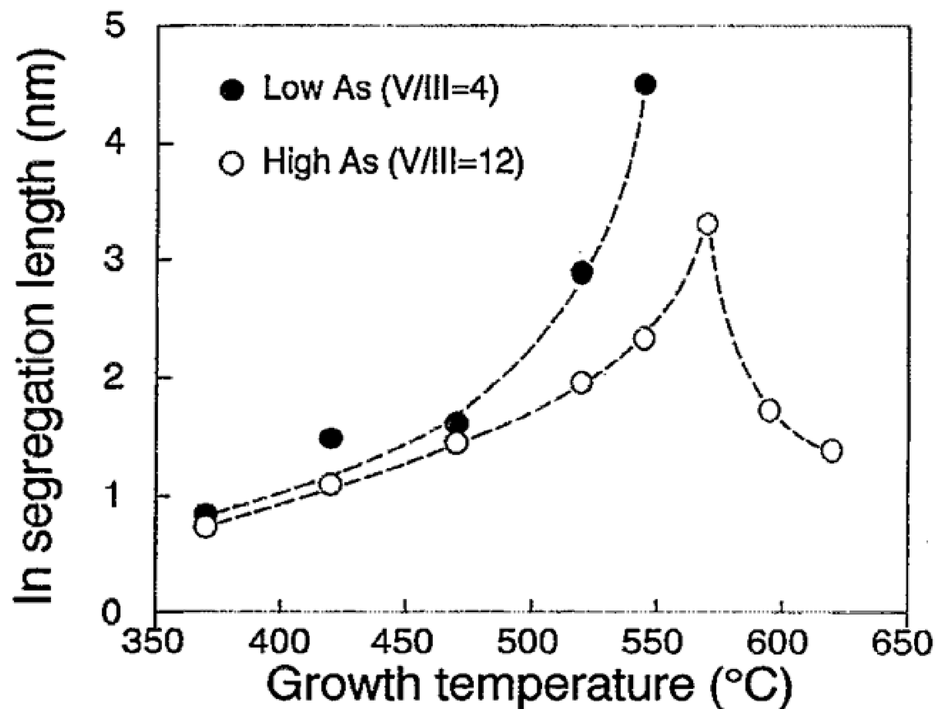

Figure 3.7: Temperature dependence of indium surface segregation length on strained $In_xGa_{1-x}As$ films. The dashed lines are guides to the eye.[57]

Recent experiments have suggested that the In segregation length in strained $In_xGa_{1-x}As$ alloys can also be calculated by observing the magnitude of the decrease in RHEED intensity oscillations during deposition. Figure 3.8(a) shows a typical RHEED oscillation recorded during the deposition of $In_{0.2}Ga_{0.8}As$ films on GaAs(001) substrates at 520 °C. The strong dampening in the magnitude of the intensity oscillations observed in Fig. 3.8(a) is usually associated with the strained growth of $In_{0.2}Ga_{0.8}As$ on GaAs due to a lattice mismatch. This mismatch results in quicker roughening of the surface as the film thickness increases. Such an argument fails to adequately explain why the dampening also occurs during deposition on vicinal substrates where the step-flow mode is dominate (resulting in an almost constant step density).[63]

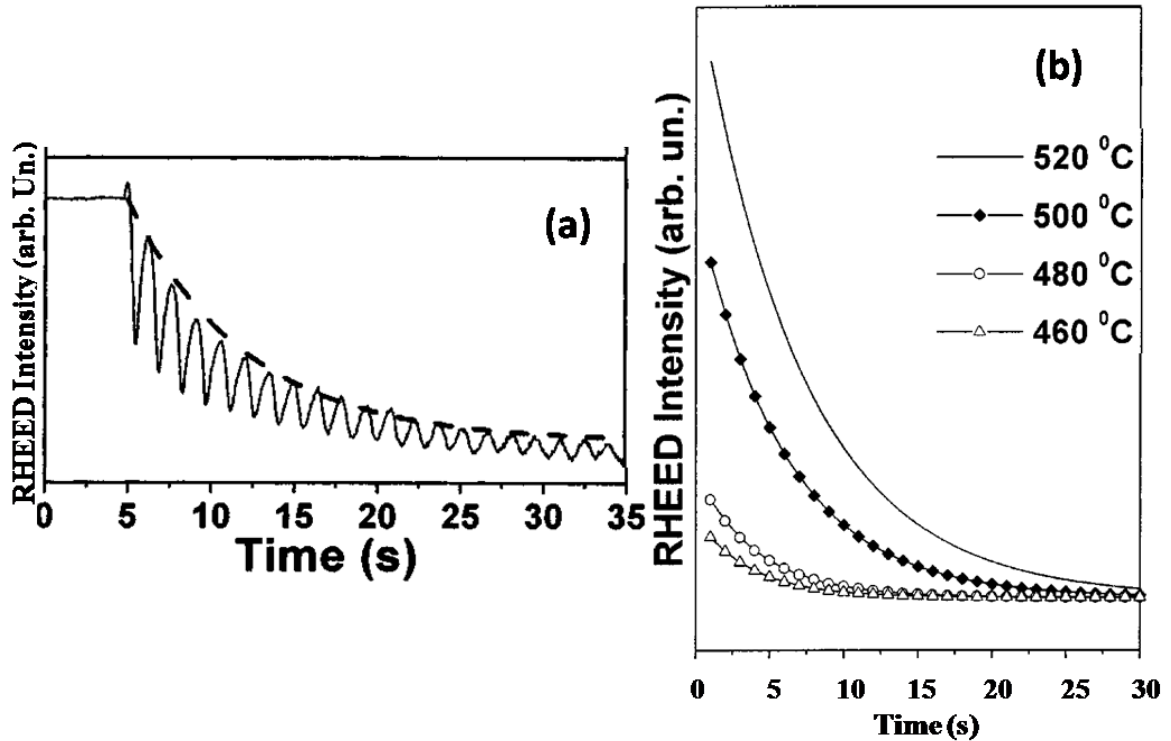

Figure 3.8: (a) RHEED oscillations of $In_{0.2}Ga_{0.8}As$ grown on GaAs at 520 °C. Dashed lines represent the best fits of the maxima of the RHEED data.[63] (b) RHEED intensity data during the deposition of $In_{0.2}Ga_{0.8}As$ films grown at different temperatures, as noted.[63]

RHEED measurements have confirmed that when $In_{0.2}Ga_{0.8}As$ films are deposited on GaAs at high growth temperatures the dampening in the RHEED intensity oscillations increases with respect to films grown at lower substrate temperatures.[63] Figure 3.8(b) is the best fits of the RHEED intensity data of $In_{0.2}Ga_{0.8}As$ layers grown at 460 °C $\leq T_g \leq$ 520 °C with a growth rate of 0.96 ML/s. The magnitude of the decrease in RHEED intensity oscillations during growth for the film grown at 520 °C is much larger than the decrease in

RHEED intensity at 500 °C. Relating the decay constant in the RHEED intensity oscillations to the characteristic length over which the effects of indium segregation can be effectively felt as defined by Muraki *et al*[57] results in a calculation of the segregation coefficient (R) that is in excellent agreement with the R calculations obtained by Kaspi and Evans[53] using temperature-programmed desorption mass spectroscopy. The segregation coefficient was calculated using the envelope function from the decrease in the magnitude of the RHEED Intensity. By measuring the dampening of the magnitude in RHEED intensity (I), a segregation coefficient may be calculated. In particular, the expression:

$$I = I_0 + I_1 \exp(-t / \tau) \qquad \textbf{Equation 3.1}$$

was used to express the dampening of the magnitude of the RHEED intensity.[63] In this expression I_0 and I_1 are constants, t is the growth time, and τ is the decay constant that is most important in the analysis of the RHEED intensity (t and τ can be expressed in MLs by multiplying them by the growth rate).[63] The physical meaning of τ can be better understood in relation to the characteristic length introduced in the Muraki et. al.[57] equation for the segregation coefficient written as:

$$R = \exp(-1 / \delta) \qquad \textbf{Equation 3.2}$$

where δ is a characteristic length over which the effects of the segregation phenomenon can be effectively sensed. If it is assumed that the strong dampening in the magnitude of the InGaAs RHEED oscillations is somehow related to the presence of a population of In atoms on the surface that are generated by the segregation process, then it is possible to calculate the segregation coefficient in terms of τ (in MLs) instead of δ.[63]

The validity of the RHEED model was also checked using photoluminescence (PL) spectroscopy measurements at 1.4 k of the quantum well structures formed on the surface. Noting that indium segregation produces a blueshift of the quantum well optical emission due to lower In content in the well, the electron and heavy-hole confinement energies of the quantum well can be related to the segregation coefficient. The values of R obtained using this method were also in excellent agreement with the results obtained by interpreting RHEED intensity decay coefficients.[63]

The growth of strained epitaxial films has many uses including the creation of metastable thin films with properties that differ from the bulk material. The use of ternary alloys like $In_xGa_{1-x}As$ allow for flexibility in tailoring the electrical and optical properties of the final devices. However, surface roughening is a serious obstacle to producing high quality devices because the surface roughening partially releases the stress in strained

heterostructures resulting in deleterious effects to their electronic and optical properties.[64] The mechanisms of surface roughening have been extensively studied with particular emphasis on the critical thickness. Critical thickness refers to the thickness above which the growth mode changes from vicinal to a three-dimensional growth on a roughened surface. This results in an incoherent interface and partial relaxation of the film.[65, 66] Beyond the critical thickness a network of dislocations can act to relieve the misfit while growth continues three-dimensionally on a roughened surface.

Figure 3.9 are a series of AFM images showing the development of the growing surface of $In_{0.1}Ga_{0.9}As$/GaAs(001) above the critical thickness as a function of film thickness.[67] The surface becomes increasingly grainy as the film thickness increases, contributing to increased surface roughening. Also, the size of the grains increase with increasing thickness and the shape of the grains elongate in the $[1\bar{1}0]$. At higher thicknesses, the elongated grains coalesce into ripple formations suggesting that the interface between the film and substrate is heavily dislocated.[68]

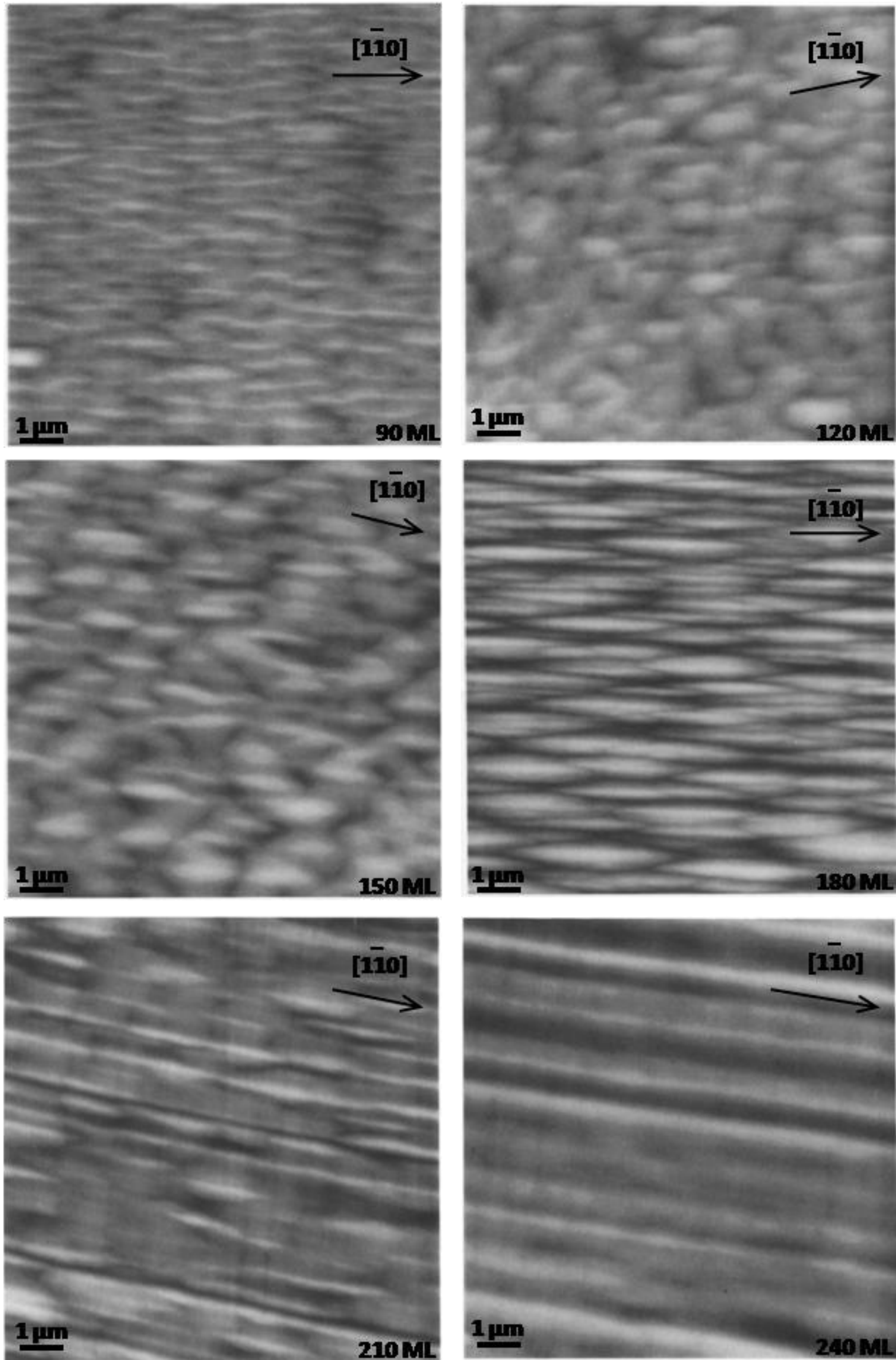

Figure 3.9: AFM images of $In_{0.1}Ga_{0.9}As$/GaAs(001) showing the surface morphologies above the critical thickness for film grown at 450 °C.

Investigations in surface roughening on lattice mismatched $In_xGa_{1-x}As$ have found that the critical thickness depends on both the growth temperature and amount of lattice mismatch (i.e. misfit strain). Several studies have noted that increasing the amount of strain decreases the critical thickness of $In_xGa_{1-x}As$ films since strain is a primary driving force of roughening.[69, 70] Growth temperature has a similar effect on the critical thickness decreasing the critical thickness at higher temperatures, presumably due to the creation of kinetic barriers to generation of dislocations.[71] Hence, thicker pseudomorphic films can be grown at lower temperatures or with a lower lattice mismatch.

Surface roughening and indium segregation are important during the growth of lattice mismatched films because they can affect the types of reconstructions that nucleate on the surface and the subsequent behavior. This chapter will investigate the behavior of β2(2x4) and (nx3) reconstructions on the surface of $In_{0.81}Ga_{0.19}As$ and how indium segregation and roughening of the surface contribute to the trends observed.

3.3 Experimental procedure

The substrates were initially heated to a temperature T=550 °C under a typical As_4 growth flux of $2 \leq F_{As4} \leq 4$ monolayers per second (ML/s) to remove the oxide layer, after which the temperature was immediately lowered

to T=485 °C. The growth rate of each of the alloy components were calibrated using RHEED oscillations. A 0.5 μm thick $In_{0.53}Ga_{0.47}As$ buffer layer lattice matched to InP(001) was deposited at a total group III growth rate R=0.5 ML/s. After deposition of the buffer layer the sample was annealed for 25 minutes while ramping to the In cell temperature required for the deposition of an $In_{0.81}Ga_{0.19}As$ film. The $In_{0.81}Ga_{0.19}As$ films are grown on the $In_{0.53}Ga_{0.47}As$ buffer layer, leading to a lattice misfit of 1.9% (misfit = $(a_f-a_s)/a_f$, where a_f = 5.9801 Å and a_s = 5.8686 Å are the lattice parameters of the $In_{0.81}Ga_{0.19}As$ film and InP(001) substrate, respectively) in compression. These films were grown to thicknesses of $10 \leq h \leq 60$ ML and growth temperatures of $465 \leq T_g \leq 515$ °C, as noted. These films were also grown under conditions that maintained layer-by-layer growth (R_{tot} = 1.1 ML/s, F_{As4} = 4 ML/s). Film thickness and growth rate are confirmed with RHEED oscillations during growth. Figure 3.10 is a RHEED image from a $In_{0.81}Ga_{0.19}As$ film grown at 495 °C showing the deposition of 20 pseudomorphic monolayers grown layer-by-layer. The RHEED also indicates that the samples growth rate is 1.1ML/sec.

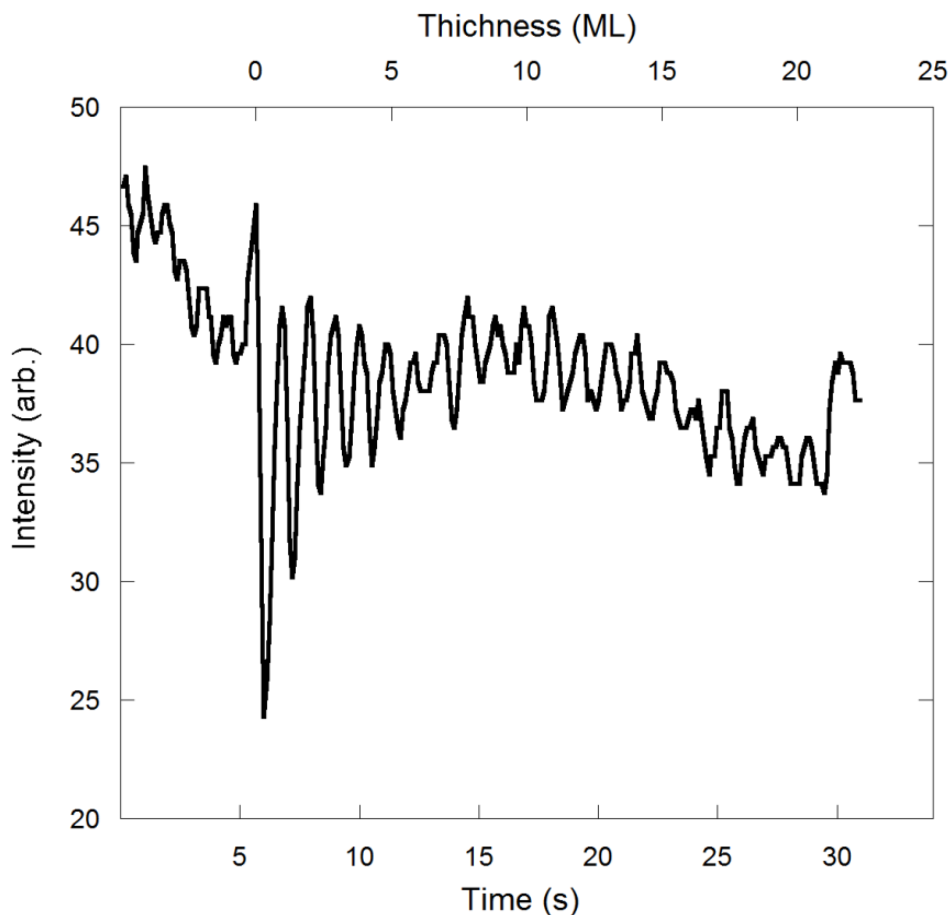

Figure 3.10 RHEED oscillations showing the film was grown to a thickness of 20 ML at a growth rate of 1.1 ML/sec.

Composition for both the lattice-matched buffer layer and the $In_{0.81}Ga_{0.19}As$ film was verified post growth using X-ray diffraction. Figure 3.11 is a XRD Ω-2θ scan taken of a thick (~300 ML) $In_{0.81}Ga_{0.19}As$ film grown at a growth temperature of T_g = 485 °C. The $In_{0.53}Ga_{0.47}As$ buffer layer is lattice matched to the InP substrate. As a result the peak corresponding to the buffer layer is hidden behind the stronger InP substrate peak. Using the BEDE

PeakSplit software, the $In_xGa_{1-x}As$ peak found at -2400 arcsecs was estimated to correspond to a film composition of x=0.81. This compositional analysis was repeated for each growth temperature used in the experiments presented in this chapter.

At the end of growth, all samples were quenched under the same As_4 flux used during growth, after which the samples were transferred *in vacuo* to a STM. This procedure has been shown to result in a surface morphology that is planar with occasional 2D islands, having an RHEED pattern that possesses the same symmetry as during deposition.[29]

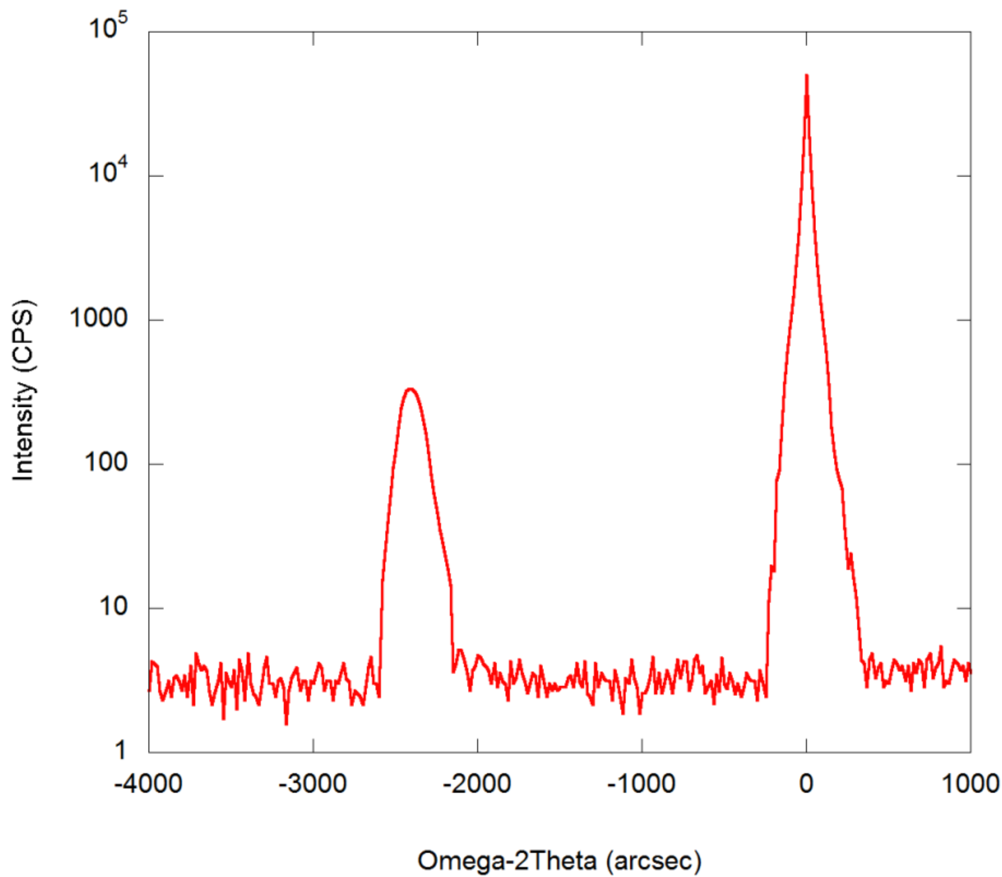

Figure 3.11: Omega-2theta scan confirming that the $In_{0.53}Ga_{0.47}As$ buffer layer is latticed matched to the InP(001) substrate. RADS simulation data confirms peak at -2400 arcsecs corresponds to an $In_xGa_{1-x}As$ films with a x=0.81 indium composition.

3.4 Coexistence of Surface Reconstructions on $In_{0.81}Ga_{0.19}As$/InP(001) Films

A mixture of different reconstruction domains are known to coexist on the surface of $In_{0.81}Ga_{0.19}As$/InP. Figure 3.12 is a filled state (-2.99 V, 100 pA) 500 x 500 Å STM image and corresponding line scan of a h=40 ML

$In_{0.81}Ga_{0.19}As/InP$ film deposited at T=475°C. The atomic surface structure consists of a disordered (nx3) surface with domains of β2(2x4). The (nx3) domain is denoted by white hash marks in Fig. 3.12. It is characterized by parallel rows that have a 3a spacing along the [110], where a=4.1 Å is the bulk lattice spacing along the {110} directions. Spots are also visible along the rows, which have some regularity in the spacing of dimers along the rows in the $[1\bar{1}0]$ approximately equal to a 4a spacing, although defects such as kinks along the reconstruction rows disrupt the long range order along the $[1\bar{1}0]$. A β2(2x4) reconstruction is also apparent (circled in Fig. 3.12). This reconstruction consists of a pair of dimers along the $[1\bar{1}0]$ separated by an As-dimer terminated trench. The line scan in Fig. 3.12 shows that the β2(2x4) appears to lay ~1-1.5 Å above the (nx3) surface reconstruction. The resolution of the β2(2x4) regions changes with bias and this is consistent with other published reports.[72] However, the apparent height of the β2(2x4) reconstructed regions does not change when the bias is reversed suggesting that the apparent height of the β2(2x4) domains is indeed half a monolayer above the (nx3) reconstructions, and is not simply due to chemical differences between the various regions.[73] Therefore, it is reasonable to assume that the β2(2x4) domains do nucleate on top of the (nx3) surface. This would also be consistent with experiments and models that suggest that there is an indium

floating layer at the surface of strained $In_xGa_{1-x}As$ alloys.[74] The floating layer is believed to be the β2(2x4) reconstruction.

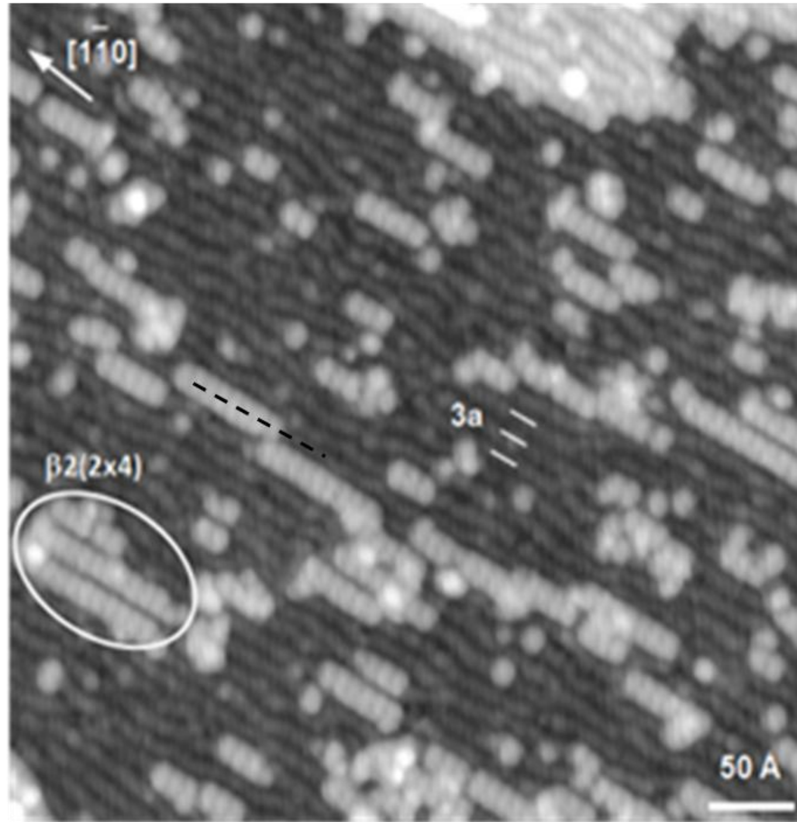

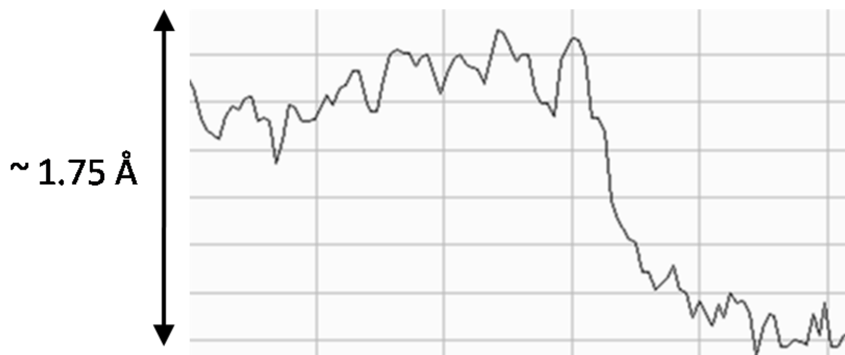

Figure 3.12: (a) Filled state in vacuo 500 x 500 Å STM (-2.99 V, 100 pA) image of a h=40 ML $In_{0.81}Ga_{0.19}As$/InP film deposited at T=475°C, R=0.5 ML/s, F_{As4}=2.5 ML/s, and V/III flux ratio=5. (4x3)/(nx3) reconstructions are denoted by hash marks with regions of β(2x4) domains of circled. (b) Line scan of the surface of the $In_{0.81}Ga_{0.19}As$ indicated by the black hashed line on the STM image in part (a).

Figure 3.13 shows the RHEED patterns during growth and upon cooling of the $In_{0.81}Ga_{0.19}As$/InP film. The <110> azimuths of the lattice matched $In_{0.53}Ga_{0.47}As$/InP buffer layer are shown in Fig. 3.13(a). The buffer layer RHEED pattern exhibits very weak streaks separated by *d*/4 along the [110] azimuth (*d* is the spacing of the primary diffraction rods), while the pattern along the $[1\bar{1}0]$ displays streaks separated by *d*/3. Thus, the reconstruction for the buffer layer is a (4x3), in agreement with published reports.[18, 75] The RHEED pattern is somewhat different for the $In_{0.81}Ga_{0.19}As$ film immediately after growth (Fig. 3.13(b)). Along the [110] azimuth, strong streaks are separated by *d*/2, while along the $[1\bar{1}0]$ streaks are separated by *d*/4 resulting in a (2x4) reconstruction. Upon cooling (Fig. 3.13(c)), the [110] azimuth remains unchanged, as do the *d*/4 and 3*d*/4 streaks in the $[1\bar{1}0]$ azimuth, but the *d*/2 streak disappears. All of this indicates an asymmetric (2x3) reconstruction that arises due to scattering from different sized domains formed from the same basic building blocks.[46] In other words, the surface is comprised of a mixture of the (nx3) and β2(2x4) reconstructions as seen in the STM data (Fig. 3.12). It is likely that domains of (nx3) are present at the growth temperature as well, but are not visible in the RHEED pattern due to the high degree of disorder within the domains compared to that of the (2x4).

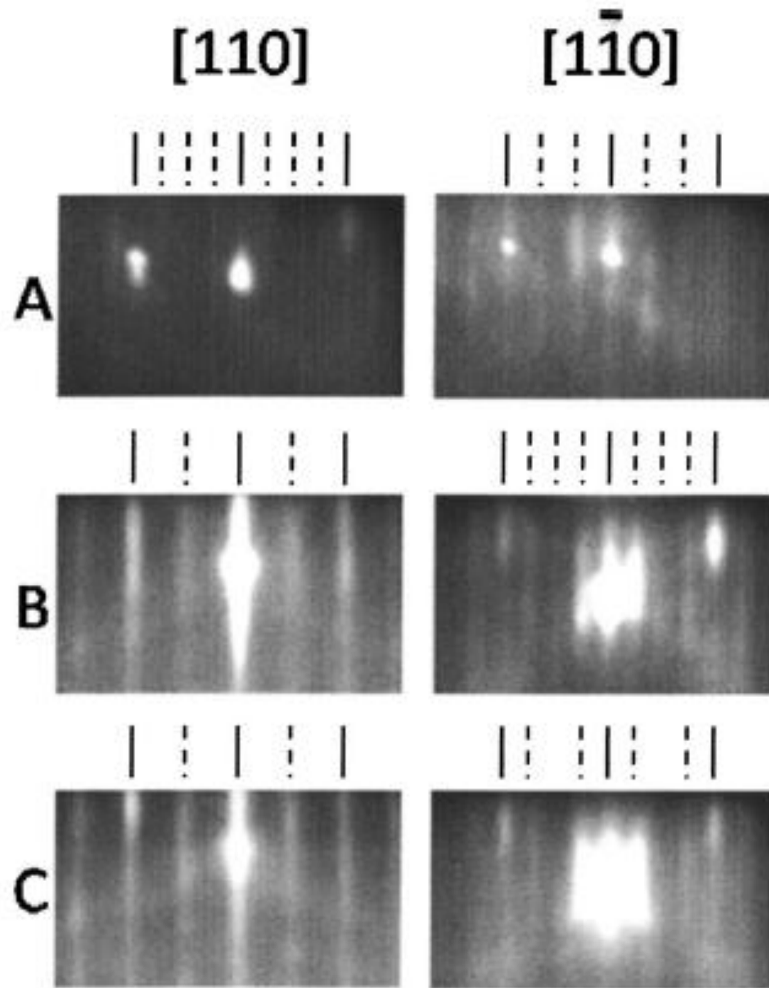

Figure 3.13: RHEED patterns after the deposition of latticed matched $In_{0.53}Ga_{0.47}As/InP$ exhibiting a weak (4x3) reconstruction (A) and $In_{0.81}Ga_{0.19}As$ immediately after growth (B) and upon cooling (C) showing a (2x4) reconstruction.

Considering only the difference in the surface energy of the two reconstructions, the fact that both the (2x4) and (nx3) reconstructions are present on the surface is surprising. Although there is still some uncertainty as to the details of the atomic arrangement of the (nx3) reconstruction, it has been suggested that the (nx3) phase has a somewhat higher surface energy than the

β2(2x4) phase across a wide range of surface energy conditions.[33] In this case, the (nx3) domain's surface energy should equal that of the β2(2x4) only for one chemical potential (or set of growth conditions). However, many groups report that the coexistence of β2(2x4) and (nx3) domains is robust over a large range of temperatures and compositions in InGaAs films.[18, 33, 49, 76]

It may be possible that the coexistence of these two reconstructions is due to the fact that the surface is rapidly quenched. That is, the mixture of the two phases represents a nonequillibrium condition. Annealing experiments show a decrease in the coverage of the (2x4) reconstruction as a function of annealing time and temperature.[29] However, XPS on those surfaces show that the In composition at the surface also decreases presumably due to desorption of In.[29] Thus, it is unclear from those experiments whether the change in coverage is a result of equilibration, or a change in the surface composition, and thus a change in the equilibrium conditions more generally.

3.4.1 β2(2x4) Surface Coverage Correlated with Film Thickness

Little is known about the correlation between film thickness and the surface coverage of the β2(2x4) reconstruction. The residual strain energy in

the film increases with increasing film thickness. If strain energy affects the development of reconstructions then a set of experiments growing $In_{0.81}Ga_{0.19}As$ films of varying thicknesses would help to elucidate any connections.

At a given thickness, the sample experiment was often repeated several times in order to verify surface coverage. This was also necessitated by the difficulty in producing high resolution images without significant noise using the *in vacuo* STM. Multiple samples were also prepared in order to improve the statistical significance of the data obtained. Experiments were repeated using an InP substrate cut from the same wafer with $In_xGa_{1-x}As$ layers grown under the same conditions as other samples for a given data point. Care was taken to use the same mounting puck for each experiment and at least four, but sometimes as many as ten, samples were prepared for STM analysis for every data point. Figure 3.14 is a series of STM images all grown to a thickness of 20 ML. Although there is some variance in the β2(2x4) surface coverage all of the coverage data falls within 1% of the mean surface coverage of 15.98%.

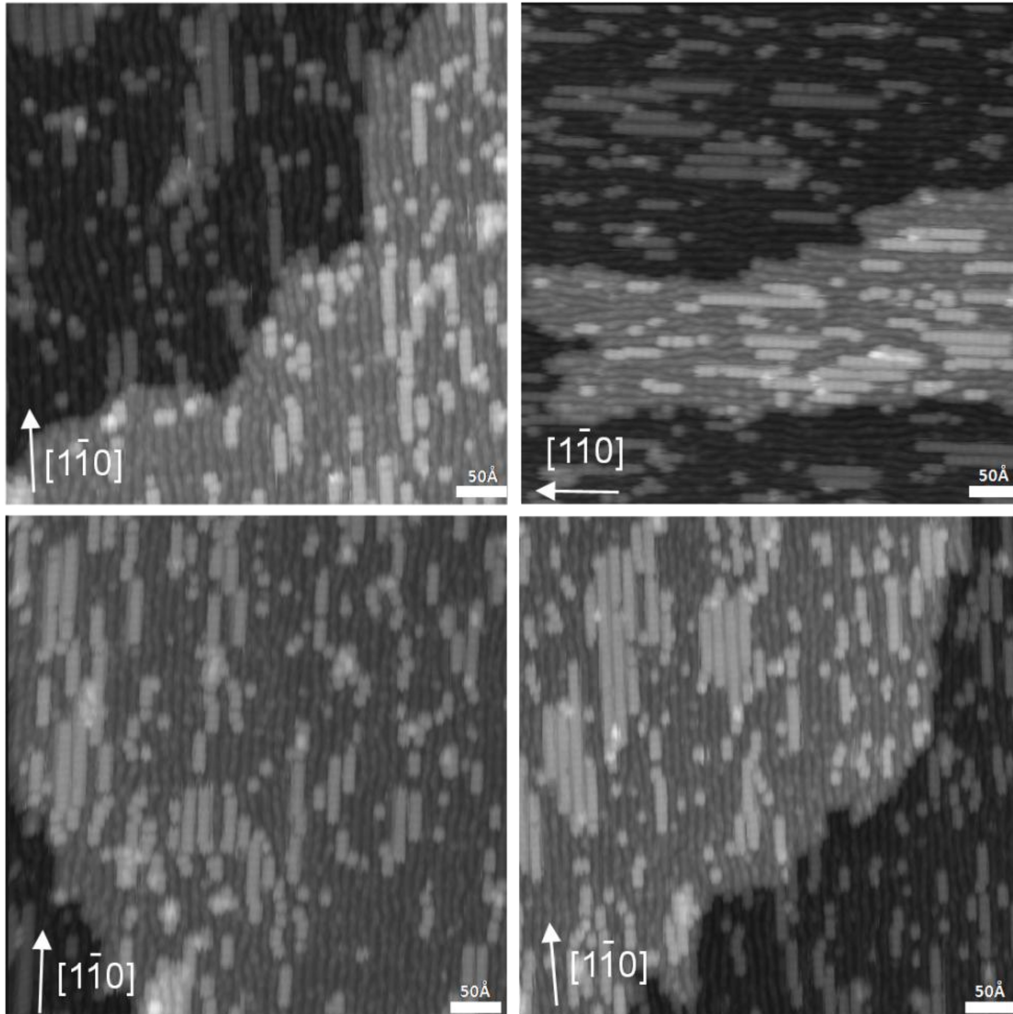

Figure 3.14: Filled states STM images of several 20 ML thick $In_{0.81}Ga_{0.19}As$ films used in analyzing the β2(2x4) surface coverage.

Figure 3.15 is a series of STM images of $In_{0.81}Ga_{0.19}As/InP(001)$ with thicknesses between $10 \leq h \leq 60$ML. All other growth parameters remain constant. A mixture of (4x3)/(nx3) and β2(2x4) reconstructions are seen on the growing surface of the films across a range of film thicknesses with the surface coverage of the β2(2x4) reconstruction increasing between 10 ML and 20 ML

before tailing off at higher thicknesses. Details about the surface coverage of the β2(2x4) in Fig. 3.15 are summarized in Table 3.1. At 10 ML the β2(2x4) reconstructions comprises approximately 9.31% of the surface while the remainder of the surface is covered in (nx3). When the film thickness is increased to 20 ML the resulting surface structure still consists of β2(2x4) and (nx3) reconstructions. The surface coverage of the β2(2x4) has increased to 15.98% and these reconstructions appear to align in a denser array of rows that are parallel to the $[1\bar{1}0]$. At 10 ML individual rows of β2(2x4) dimmers tend to form with an average chain length of 3±2 dimers. On the 20 ML STM image in Fig. 3.15 there are several spots where four or more rows are aligned parallel to each other and the average chain length has risen to 5±3 dimers. The β2(2x4) surface coverage begins to decrease with increasing thickness above 20 ML and by 30 ML the surface coverage has fallen to 8.21%. The surface coverage continues to decrease as the thickness increases up to the critical thickness. A decrease in the β2(2x4) surface coverage at higher thicknesses has been attributed to an increase in roughening in the layer, which is seen in the AFM images of thicker films.[29] This suggests that the two reconstructions are stable across a wide range of film thicknesses.

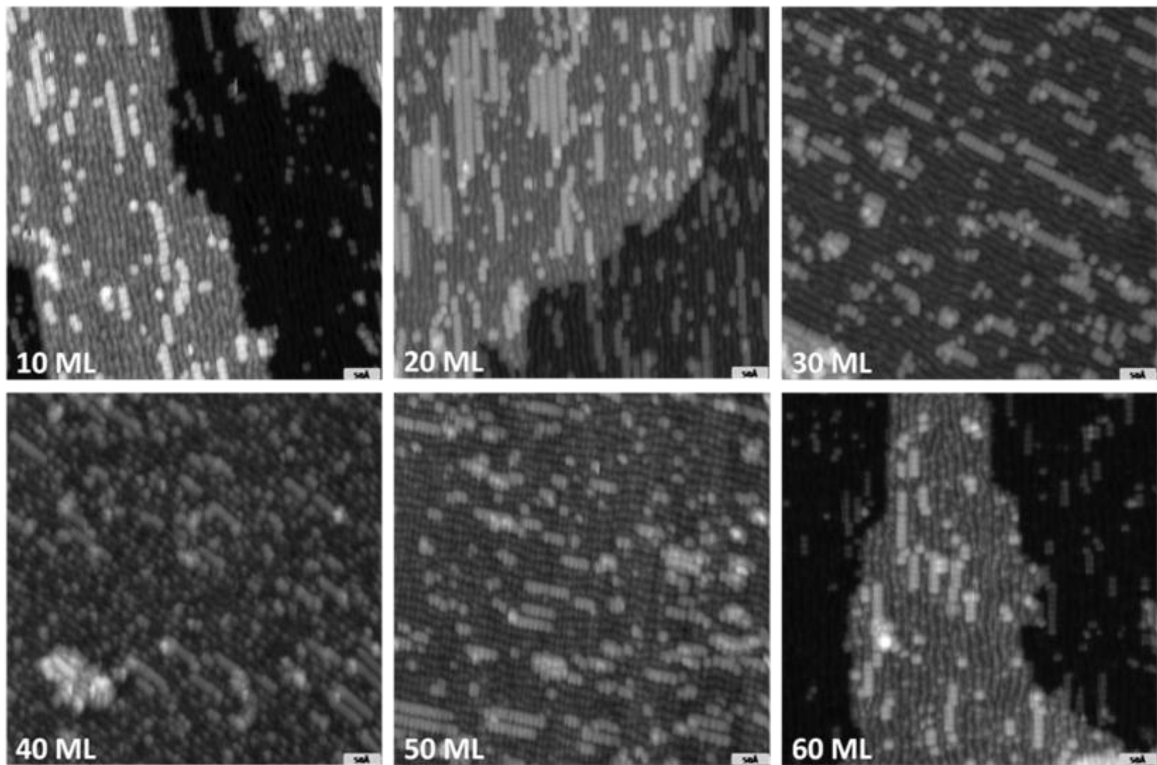

Figure 3.15: In situ STM (-2.88 V, 100 pA) images of $In_{0.81}Ga_{0.19}As$/InP. If growth temperature is kept constant and the total thickness of the $In_{0.81}Ga_{0.19}As$ layer is allowed to vary from 10 ML < h < 60 ML, a mixture of (4x3)/(nx3) and β2(2x4) are observed on the growing surface. All sample were grown with T_g= 495 °C, R_{Ga}= 0.5 ML/s, and V/III flux= 4 (after twenty minute anneal).

Thickness	β2(2x4) Length	β2(2x4) Area	Coverage
10 ML	3±2 dimers	11.25±1.31 nm^2	9.56±0.32%
20 ML	11±3 dimers	33.44±4.77 nm^2	15.89±0.61%
30 ML	8±4 dimers	17.83±1.59 nm^2	8.21±0.27%
40 ML	3±2 dimers	10.89±2.81 nm^2	5.43±0.19%
50 ML	5±2 dimers	17.36±6.75 nm^2	4.82±0.14%
60 ML	4±2 dimers	13.53±8.32 nm^2	5.01±0.12%

Table 3.1: Details about the surface coverage of the β2(2x4) reconstructions shown in Fig 3.15 including the dimer length, domain area, and total surface coverage.

3.4.2 Coexistence as a function of growth temperature

A set of experiments varying the growth temperature would be useful in proving that the two reconstructions are stable across a range of growth temperatures, in agreement with previously published reports for reconstructions found on other semiconducting alloys.[33, 76, 77] Figure 3.16 is a series of *in vacuo* STM images of $In_{0.81}Ga_{0.19}As$/InP(001) where the growth temperatures varies between 465 °C ≤ T ≤ 515 °C.

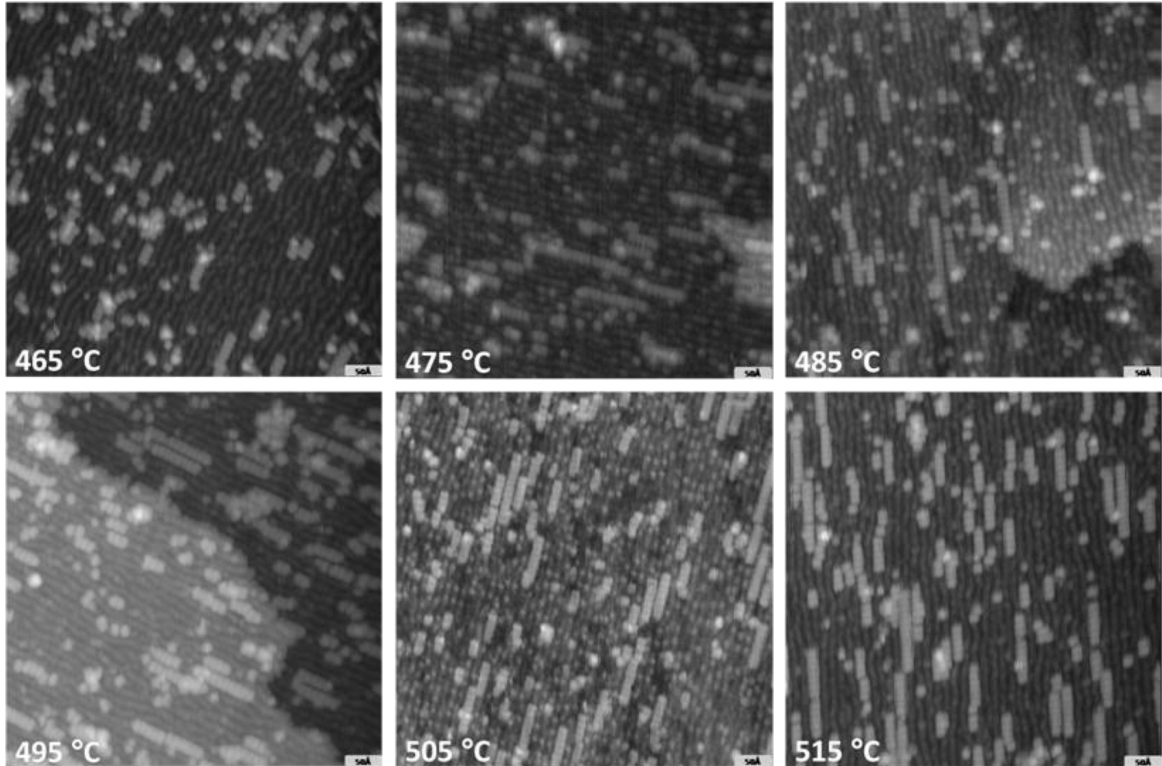

Figure 3.16: In situ STM (-2.88 V, 100 pA) images of $In_{0.81}Ga_{0.19}As$/InP. Temperature is the only growth condition varied from 465 °C ≤ T ≤ 515 °C. A mixture of (4x3)/(nx3) and β2(2x4) domains are stable on the growing surface of $In_{0.81}Ga_{0.19}As$/InP(001) across a range of growth temperature. All samples are 10 ML thick with R_{Ga}= 0.5 ML/s, and V/III flux= 4 (after five minute anneal).

Details about the surface coverage of the β2(2x4) in Fig. 3.16 are summarized in Table 3.2. At 465 °C, the STM image in Fig. 3.16 is comprised of approximately 2% β2(2x4) with the remainder of the surface covered in (nx3). The β2(2x4) reconstruction aligns in isolated chains of 3±2 dimers long. When the growth temperature is increased 475 °C the chain length has risen to 5±3 dimers and a few parallel chains of β2(2x4) reconstructions are beginning to appear. Surface coverage of the β2(2x4) continues to increase with

increasing temperature through 515 °C. At higher temperatures film roughening prevents quantitative analysis of the surface reconstructions using a STM. As the temperature increases the β2(2x4) clusters into larger adjacent rows and the average chain length also continues to increase. These images show that there is a mixture of (4x3)/(nx3) and β2(2x4) reconstructions that are stable across a range of growth temperatures.

Temperature	β2(2x4) Length	β2(2x4) Area	Coverage
465 °C	3±2 dimers	8.02±0.73 nm^2	1.83±0.08%
475 °C	5±3 dimers	11.41±1.09 nm^2	5.20±0.14%
485 °C	5±4 dimers	10.60±0.92 nm^2	6.87±0.21%
495 °C	5±3 dimers	14.13±0.87 nm^2	9.31±0.31%
505 °C	7±4 dimers	16.05±2.04 nm^2	10.36±0.51%
515 °C	9±5 dimers	19.19±3.63 nm^2	13.98±0.55%

Table 3.2: Details about the surface coverage of the β2(2x4) reconstructions shown in Fig 3.16 including the dimer length, domain area, and total surface coverage.

3.4.3 Summary of Results

The coexistence of the β2(2x4) and (nx3) reconstructions is robust over a wide range of growth conditions. Figure 3.17 is a plot of the surface coverage

data of β2(2x4) reconstructions on $In_{0.81}Ga_{0.19}As$ as a function of film thickness. Experimental data for different temperatures are plotted. Across the growth temperatures studied the maximum film thickness was limited by the roughening of the film, which inhibits the ability of the STM tip to remain stable enough to successfully image the surface. At T_g = 465 °C the surface coverage of the β2(2x4) slowly increases from approximately 1.9% at 10 ML to almost 9% at 50 ML. This is followed by a decrease to just over 7% above 50 ML. This trend of the surface coverage increasing followed by a decrease at higher thicknesses is consistent across the growth temperatures presented. At T_g = 475 °C the maximum β2(2x4) surface coverage of 11% occurs at 35 ML, 15 ML less than the thickness of the maximum surface coverage at T_g = 465 °C. The thickness where the maximum surface coverage is observed continues to decrease as the growth temperature is increased and at T_g = 515 °C the maximum surface coverage is 10 ML.

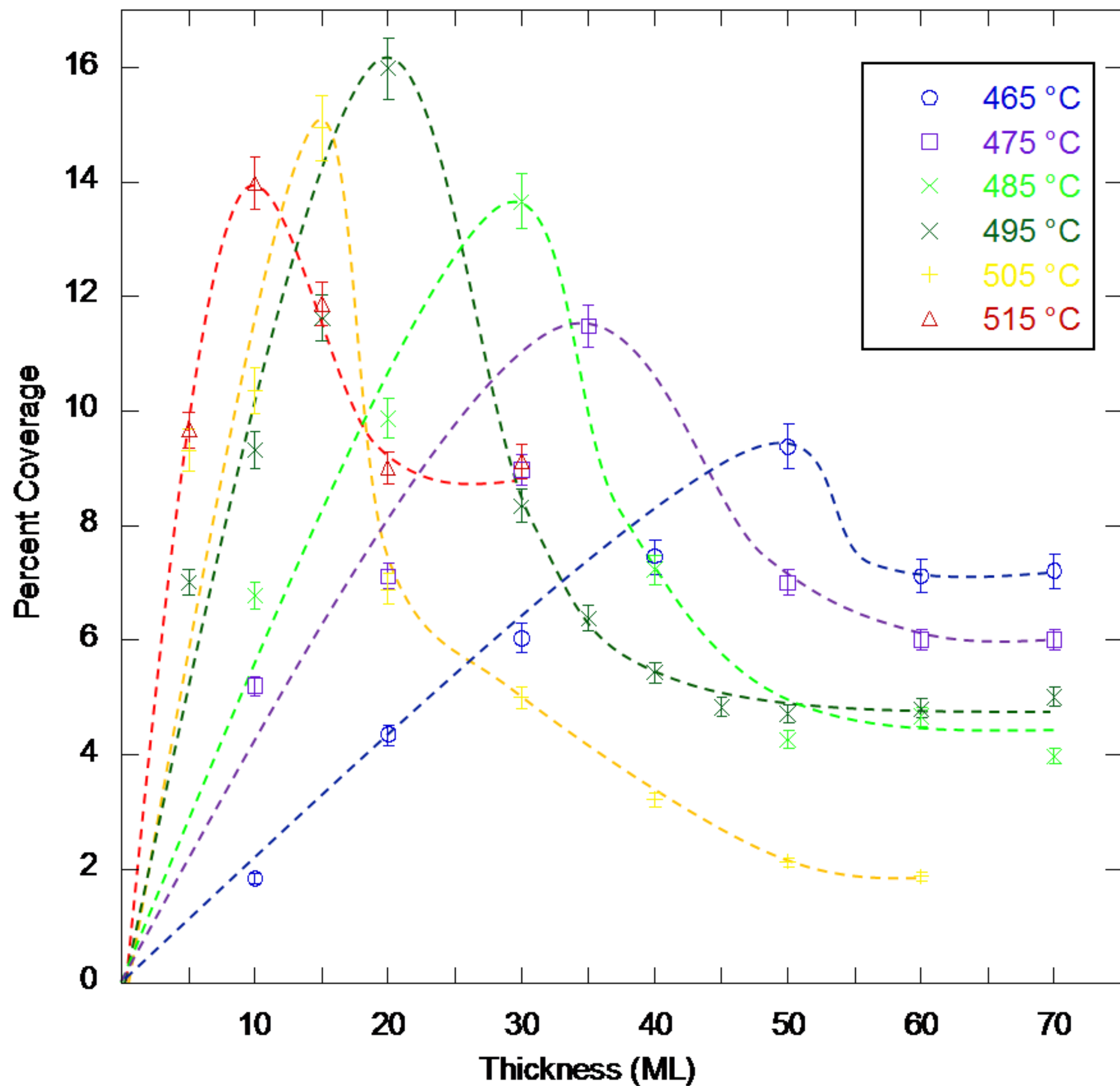

Figure 3.17: A plot of the β2(2x4) surface coverage as a function of film thickness and growth temperature. The dashed lines are guides for the eye with different temperatures highlighted in different colors to better illustrate the β2(2x4) coverage pattern.

3.5 Discussion

In general, the coverage of the β2(2x4) increases with increasing film thickness, followed by a decrease in coverage at the highest thicknesses. This decrease at higher thicknesses has been attributed to increased roughening of the layer.[78] The thickness at which the maximum coverage is observed is related to the growth temperature. Indium segregation is also related to the surface coverage of the β2(2x4).[58] In this section the influence of indium surface segregation and surface morphology are discussed in more detail.

3.5.1 Indium Segregation in $In_{0.81}Ga_{0.19}As$/InP(001) Films

The surface coverage of the β2(2x4) is related to the growth temperature, as shown in Fig. 3.17. The maximum surface coverage for a given temperature series increases with increasing temperature to 495 °C before tailing off at higher temperatures. It is proposed that the formation of β2(2x4) domains is related to indium segregation.[49, 58, 79] There is also experimental evidence that suggests that the magnitude of dampening in RHEED intensity oscillations is related to the indium segregation coefficient.[63] Figure 3.18 shows a set of two RHEED intensity oscillations during the depositions of $In_{0.81}Ga_{0.19}As$ at 485 °C(blue dashed oscillations at top) and 505 °C(solid red oscillations at

bottom). The magnitude of the decay in intensity oscillations for films grown at 505 °C (measured by subtracting the minimum RHEED intensity from the maximum intensity of the oscillations at the beginning and end of growth) is greater than the initial magnitude of the decay for films grown at 485 °C as measured using Eqn. 3.1 and Eqn. 3.2. In other words the magnitude of the decay in intensity during growth is the parameter that is being examined as evidence of indium segregation, not the global maximum intensity relative to another sample grown at a different temperature.

It is well known that the indium segregation length is larger at high temperature because the exchange of atoms between the sublayers and the surface becomes more kinetically limited as the growth temperature is decreased.[57] The decrease in the initial magnitude of the RHEED intensity oscillations at lower temperature in Figure 3.18 is evidence of a corresponding decrease in the indium segregation length. This result is consistent with the maximum β2(2x4) surface coverage trends on $In_{0.81}Ga_{0.19}As$, which increase through 495 °C. Therefore it is reasonable to expect that the increase in the global maximum surface coverage of the β2(2x4) with increasing growth temperature is related to indium segregation.

The decay constant for the RHEED oscillations shown in Fig. 3.18 was obtained using Eqn. 3.1 and then multiplied by the growth rate to obtain a value

of the decay constant expressed in MLs. The segregation coefficient and segregation length can now be calculated using the decay constant instead of the characteristic length. The results show that a segregation coefficient of R = 0.84 at T_g = 505 °C and R = 0.74 at T_g = 495 °C. Therefore, the effective length over which the effects of the segregation phenomena can occur rises from 3.3 ML at T_g = 495 °C to 5.7 ML at T_g = 505 °C, resulting in an increase of ~73%.[63] This is consistent with the coverage trends shown in Fig. 3.17 where the maximum β2(2x4) surface coverage increases 81% over the same temperature range.

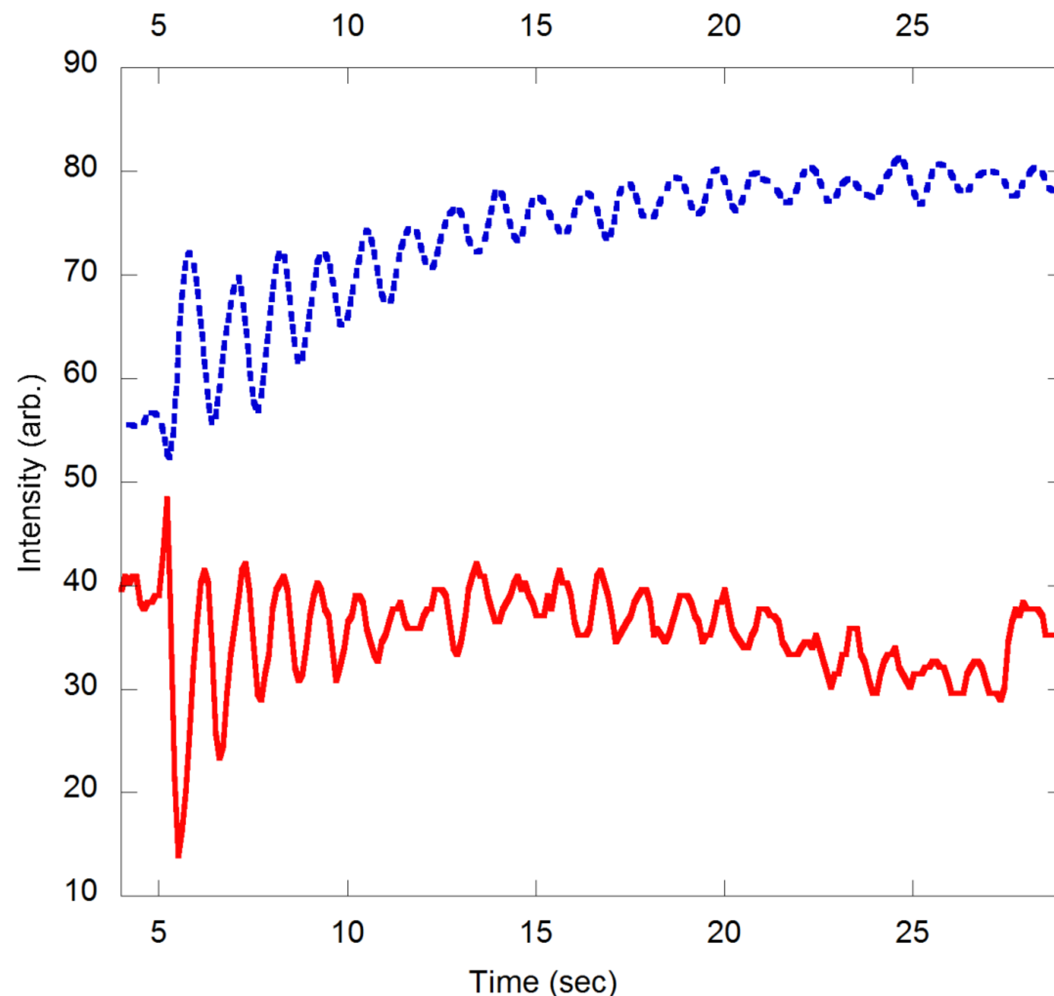

Figure 3.18: RHEED intensity oscillation for $In_{0.81}Ga_{0.19}As$ films grown at 485 °C (blue dashed oscillations at top) and 505 °C (solid red oscillations at bottom). The magnitude of the decay in intensity oscillations for films grown at 505 °C is greater than the magnitude of decay in intensity oscillations for films grown at 485 °C.

A decrease in the β2(2x4) surface coverage above 495 °C as observed in STM images is likely due to indium desorption from the surface. Indium desorption is more dominant at higher temperatures, particularly above

500°C.[57] Desorption reduces the surface population of indium atoms, resulting in a corresponding decrease in the indium segregation length.

Indium segregation also plays a role in the relationship between β2(2x4) surface coverage and film thickness. Across all of the temperature regimes studied the β2(2x4) surface coverage initially increases with increasing film thickness. As the film get thicker there are additional indium atoms available in the bulk to segregate to the surface layer. In other words, the segregation of indium to the surface for thin film is limited by the number of indium atoms available in the bulk. At T_g = 465 °C, the indium segregation length in InGaAs films has been measured at 1.4 nm.[57] At this temperature only a few monolayers below the surface would be available to contribute indium atoms. By T_g = 495 °C, the indium segregation length has increased to 2.1 nm.[57] This increase in the segregation length is consistent with the maximum β2(2x4) surface coverage, which increases from 8.8% to 15.9% over the same temperature range.

3.5.2 Influence of Surface Morphology on Coexistence

Analysis of the β2(2x4) surface coverage with increasing thickness shows that the coverage initially increases with film thickness followed by a decrease at higher thicknesses. While the initial increase in β2(2x4) coverage

can be attributed to indium segregation, the mechanisms behind the decrease in the surface coverage at higher thicknesses are not well understood at this time.

Figure 3.19 shows a graph of the surface coverage of the β2(2x4) reconstructions (blue) and surface roughness data (red) for $In_{0.81}Ga_{0.19}As$ films grown at 485 °C for thicknesses 10 ML ≤ h ≤ 70 ML. The roughness data was obtained from ten point roughness analysis. Initially, the surface coverage of the β2(2x4) domains increases with increasing thickness up to 20 ML before decreasing at higher thicknesses.

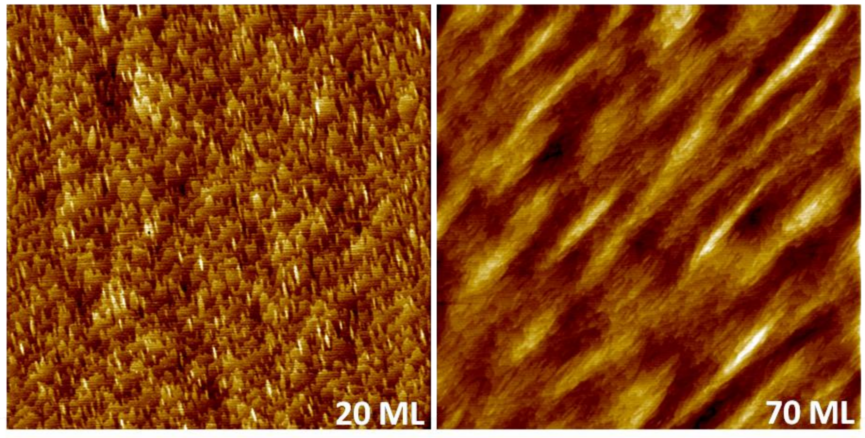

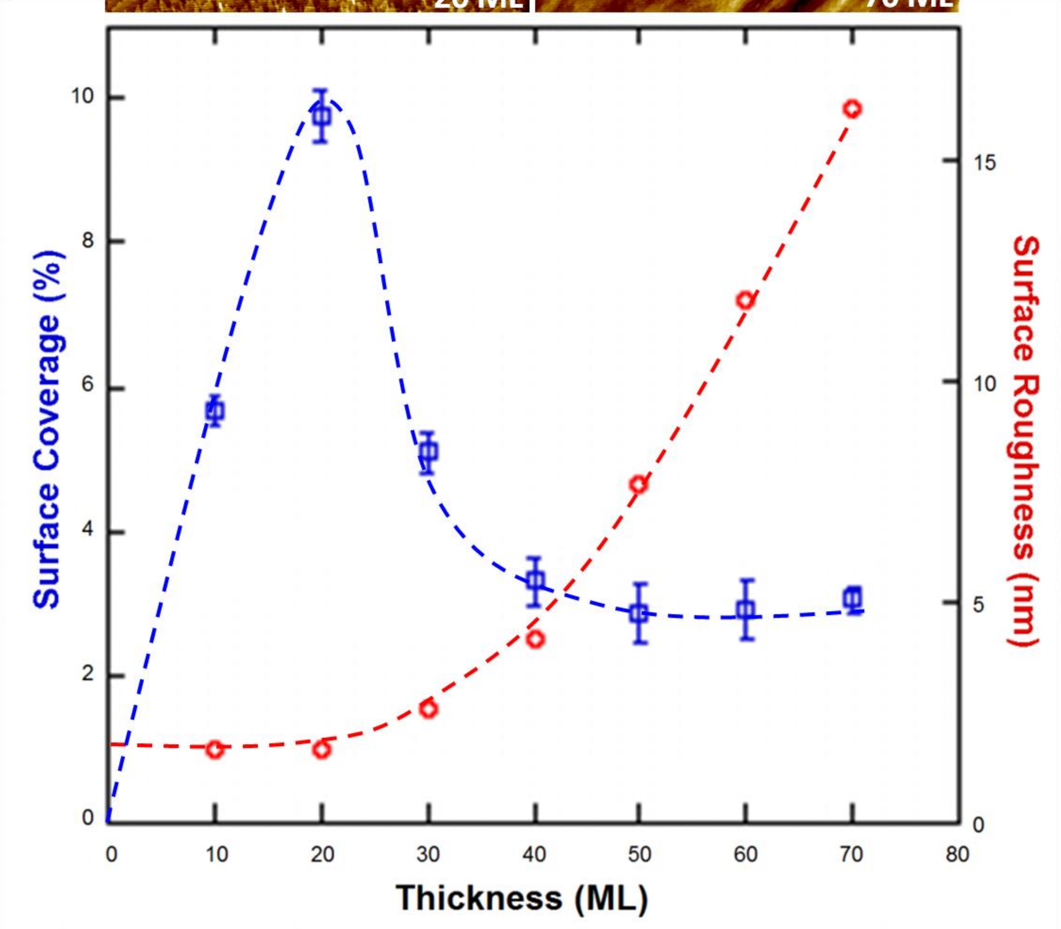

Figure 3.19: Plot of the surface coverage of the β2(2x4) reconstructions (blue) and surface roughness data (red) for $In_{0.81}Ga_{0.19}As$ films. AFM micrographs of the surface at 20 ML and 70 ML are also shown.

β2(2x4) reconstructions are thought to be stabilized by strain in the film as a result of a lattice mismatch.[80] It is well known that surface roughening is a common strain relief mechanism in films grown with a high lattice mismatch, especially at or near the critical thickness. The driving force behind roughening is that although the surface area increases the roughening allows for the partial relaxation of strain due to elastic deformation of the film. AFM images taken at each thickness plotted in Fig. 3.19 show a change in surface morphology at 60 ML and above. At lower thickness the $In_{0.81}Ga_{0.19}As$ surface is vicinal and characterized by layer-by-layer growth similar to 20 ML AFM image shown in Fig. 3.19. At 60 ML AFM micrographs show that the surface morphology has transitioned to a mounded three-dimensional growth mode like the AFM of the surface shown at 70 ML in Fig. 3.19. This evidence suggests that there is roughening in the film that is relieving residual strain in the film. This is consistent with the surface coverage data that shows that as the surface roughness increases the β2(2x4) coverage decreases. If the β2(2x4) domains are indeed stabilized by strain then their surface coverage should decrease if the strain is somehow relieved.

3.6 Conclusions

Surfaces of $In_{0.81}Ga_{0.19}As$/InP grown by molecular beam epitaxy and imaged by *in vacuo* scanning tunneling microscopy were studied in this chapter. The main conclusions are summarized as follows:

(1) The surface of $In_{0.81}Ga_{0.19}As$ films was observed to consist of small anisotropic regions of a β2(2x4) reconstruction in a matrix of a disordered (nx3) reconstruction.

(2) The presence of β2(2x4) is stable across a range of growth conditions and material properties including growth temperature and total film thickness.

(3) Indium segregation length plays a role in domain stability and the resulting surface coverage of β2(2x4). Surface coverage data shows that growth temperate affects the nucleation and growth of the β2(2x4) reconstruction.

(4) The β2(2x4) domains are strain stabilized. Surface coverage data of films shows that the total film thickness plays a role in the stability of β2(2x4) domains. AFM images and surface roughness analysis shows that there is a transition from vicinal to mounded growth at thicknesses coinciding with a decrease in the β2(2x4) coverage.

Chapter 4

Thermodynamic Model of the Coexistence of (nx3) and β2(2x4) Reconstructions

4.1 Introduction

As seen in Chapter 3, multiple reconstruction domains can coexist on the surface of $In_{0.81}Ga_{0.19}As$ across a wide range of growth conditions. It is believed that elastic relaxation at the boundaries of the β2(2x4) reconstruction and strain energy play a role in thermodynamically stabilizing the surface reconstruction domains. Anisotropy at the boundaries can affect the final shape of stable reconstruction domains. This chapter presents a thermodynamic model originally developed by Tromp *et. al.*[19] for triangular shaped domains on Si(11) and modified in order to help understand the stability of the β2(2x4) and (nx3) reconstructions on the surface of $In_{0.81}Ga_{0.19}As$. This model incorporates elastic relaxation, unit strain energy, and anisotropy at the boundaries to determine the free energy on the surface. The thermodynamic model is used to analyze experimental results for $In_{0.81}Ga_{0.19}As$/InP and the model fits the data reasonably well.

The contents of this chapter are structured in the following manner. **Section 4.2 ("Background")** discusses the energetics of a mixed reconstruction surface with rectangular shaped domains under stress. Consideration will also be given to the effects of anisotropy in the elastic relaxation term. **Section 4.3 ("Experimental Procedure")** details the methods used to grow the $In_{0.81}Ga_{0.19}As$ films used to fit the model. **Section 4.4 ("Thermodynamic model")** presents in detail the thermodynamic model paying particular attention to a free energy equation incorporating elastic relaxation of rectangular shaped domains and the inclusion of anisotropy in the elastic relaxation term of the model. The thermodynamic model derived in Section 4.4 is discussed in detail in **Section 4.5 ("Discussion")** paying particular attention to the influence of surface energy (Section 4.5.1), the geometry of the domains (Section 4.5.2), and the importance of elastic relaxation when modeling the domains seen on the surface of $In_{0.81}Ga_{0.19}As$ (Section 4.5.3). The effects of anisotropy in the boundary energy term is also discussed (Section 4.5.4) and a comparison to the experimental data is presented (Section 4.5.5). The main conclusions of this chapter are summarized in **Section 4.6 ("Conclusions")**.

4.2 Background

The nucleation and growth of surface reconstructions at low temperature is often discussed in terms of kinetics. In the past few years, studies utilizing STM and AFM have greatly improved the understanding of kinetic processes such as the adsorption of atoms onto a surface, the diffusion of these atoms once on the surface, and their attachment to a growing nucleus. At low temperature adatom diffusion is slow and a deposition flux will usually result in adatom concentrations that far exceed the equilibrium concentration of atoms on the surface. These conditions are not necessarily true at higher deposition temperatures. At higher temperatures the equilibrium adatom concentration on the surface can be so high that an incoming growth flux may only slightly increase the surface concentration. For high temperature growths reversible collective phenomena are more important than individual atomic events and thermodynamics have a larger impact on the nucleation and growth of reconstructions than kinetics.

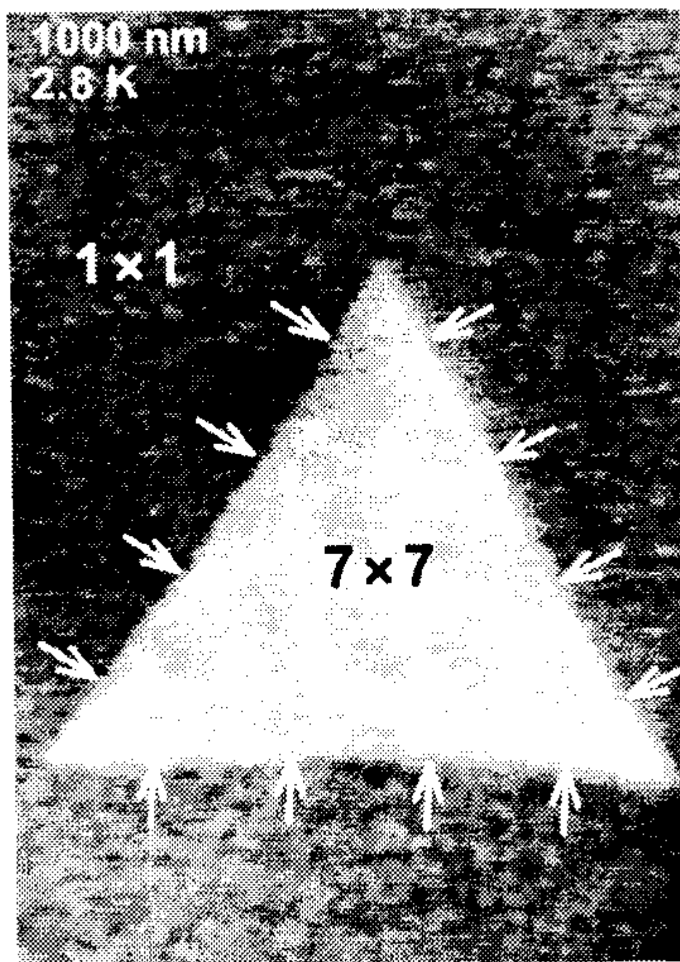

Figure 4.1: Image of the surface of Si(111) showing a (7x7) domain in a (1x1) background on large step-free terraces. The difference in surface stress between the two domains results in force monopoles at the phase boundaries (arrows).[19]

Recently, research has gone into understanding the nucleation and growth of mixed reconstruction domains on the surface of semiconducting surfaces via a thermodynamic model.[19] The surface free energy of the Si(111) surface was analyzed with respect to the (7x7) and disordered (1x1)

reconstructions observed on the surface and shown in Fig. 4.1. The surface stresses of these two reconstructions differ with the (7x7) reconstruction being tensile relative to the (1x1). As a result of these different reconstructions the surface of Si will lower its overall strain energy by elastic relaxation. In this case the more compressive regions will tend to elastically expand while tensile regions will contract. The free energy costs associated with forming a single triangular shaped (7x7) domain with sides of length L in a matrix of (1x1) is given by:

$$\Delta G = 3L\beta + \frac{\sqrt{3}}{4}L^2\Delta\gamma + U(L) + E_c \text{ [19]} \qquad \textbf{Equation 4.1}$$

The first term in Eq. 4.1 represents the energetic cost of the boundary between the (7x7) and (1x1) boundary. β represents the boundary energy per unit length and 3L represents the total length of the (7x7) boundary. The second term in Eq. 4.1 accounts for the differences in the surface energy between the two reconstructions. Δγ represents the difference in energy between to two domains per unit area with the area of the (7x7) equal to $\frac{\sqrt{3}}{4}L^2$. U(L) is the energy gained through elastic relaxation at the boundaries and E_c represents the energy costs associated with the corners of the triangular domain.

The same general approach used for the triangular (7x7) domains found on Si(111) can also be applied more generally to the coexistence of multiple

rectangular shaped domains. Taking into account the boundary energy, surface energy, elastic energy and rectangular geometry yields a change in the free energy equal to:

$$\Delta G = 2(s + t)\beta + st\Delta\gamma + U(s,t) + E_c \text{ [19]} \qquad \textbf{Equation 4.2}$$

where s and t represent the length and width of the rectangular domain. For a given rectangular domain it is useful to consider the energy associated with a domain with a given area A=st. Given a fixed area the domain can optimize its shape by varying the value of s and t under the constraint A=st in order to minimize the elastic and boundary energy. Using Eqn. 4.2 to analyze this shape distribution yields some interesting results. Figure 4.2 is a plot of the area of a rectangular domain versus length or width calculated using Eqn. 4.2. When the area of the domain is kept small the equilibrium shape is always square (s=t). As the domain area increases the square shape becomes energetically unfavorable, eventually leading to a bifurcation above a critical area as depicted in Fig. 4.2.

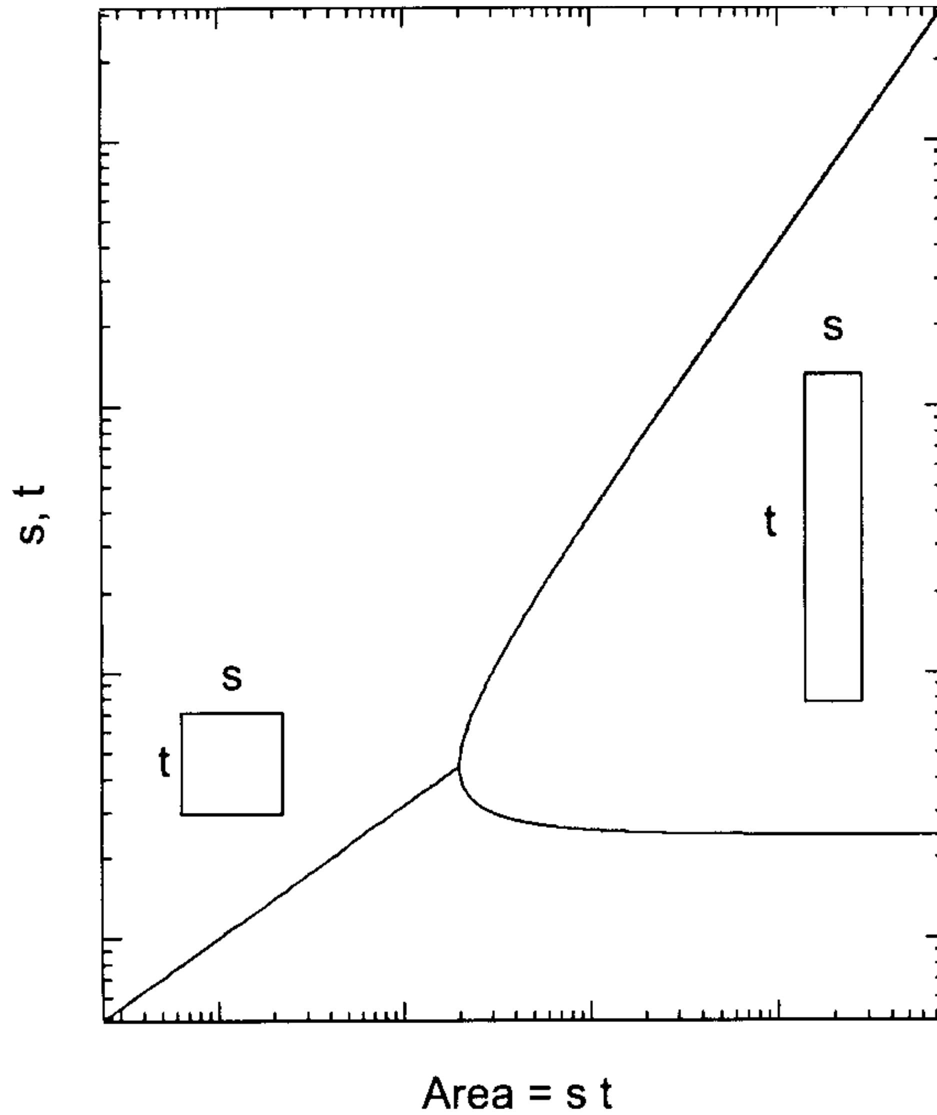

Figure 4.2: Graph of the area of a rectangular shaped domain versus length or width derived using Eqn. 4.2. Small domains have a square geometry but above a critical size the shape will always transform into a rectangle of width *s* and length *t*.[19]

The exact value of the critical area depends on the ratio of the boundary energy to the elastic relaxation energy per unit length (F_0). As the boundary energy increases, the square shape remains stable at higher sizes as it minimizes the boundary length for a given area. But as the squares increase in

size elastic relaxation becomes less effective eventually leading to a bifurcation regardless of the ratio of β to F_0.

The form of U(x,y), the elastic relaxation energy, has been determined by continuum elasticity theory for the case where an isolated rectangular domain is subjected to an isotropic biaxial stress.[81] Li and coworkers[81] have shown that under these conditions, the elastic relaxation energy of a rectangular domain is given by:

$$U(x,y) = 2U_1(x) + 2U_1(y) + 2U_2(x,y) + 2U_3(x,y) + 2U_3(y,x)$$

Equation. 4.3

where $U_1(x)$ is the energy contained in an isolated boundary, $U_2(x,y)$ is the interaction between the sides of a domain that meet at a corner, and $U_3(x,y)$ is the interaction between parallel sides of the isolated boundary. The terms that make up Eqn. 2 are as follows:

$$U_1(x) = F_0\left[(1-\upsilon)x\ln\frac{x}{ea} - 1\right]$$

$$U_2(x,y) = F_0\left[x + y - \sqrt{x^2+y^2}\right]$$

$$U_3(x,y) = 2F_0\left[(1-2\upsilon)\left(x - \sqrt{x^2+y^2}\right) + y(1-\upsilon)\ln\frac{\sqrt{x^2+y^2}+y}{\sqrt{x^2+y^2}-y}\right]$$

where υ is Poisson's ratio, a is the lower limit of integration (i.e. a approaches the lattice parameter), F_0 is the unit strain energy given by $F_0 = \frac{(1+\upsilon)f^2}{2\pi M}$, where f is the magnitude of the difference in the stress between the reconstruction domains, and M is the Young's modulus.[81]

The free energy costs associated with the formation of a mixed reconstruction domain as shown by Tromp et. al. can be extended to include the coexistence of the β2(2x4) and (nx3) domains found on the surface of $In_{0.81}Ga_{0.19}As$ if the free energy equation is modified to include the rectangular geometry of the reconstructions and the biaxial stress found on these films. What follows is a discussion of the role thermodynamics plays in the nucleation and growth of β2(2x4) reconstructions in a matrix of (nx3).

4.3 Experimental Procedure

Samples were grown using an EPI 930 molecular beam epitaxy system with solid source In and Ga cells and a valved cell for As_4. The growth rates were calibrated using reflection high-energy electron diffraction (RHEED) intensity oscillations, and the growth temperature was monitored using a pyrometer, calibrated by observing the temperature at which the oxide desorption for an InP(001) substrate occurs. The substrates were initially

heated to a temperature T=550°C under a typical As_4 growth flux of $2 \leq F_{As4} \leq 4$ monolayers per second (ML/s) to remove the oxide layer, after which the temperature was immediately lowered to T=485°C. The growth rate of each of the alloy components were calibrated using RHEED oscillations. A 0.5 μm thick $In_{0.53}Ga_{0.47}As$ buffer layer lattice matched to InP(001) was deposited at a total group III growth rate R=0.5 ML/s. After deposition of the buffer layer the sample was annealed for 25 minutes while ramping to the In cell temperature required for the deposition of an $In_{0.81}Ga_{0.19}As$ film. These films were also grown under conditions that maintained layer-by-layer growth. At the end of growth, all samples were quenched under the same As_4 flux used during growth, after which the samples were transferred *in vacuo* to a Scanning Tunneling Microscope (STM). This procedure has been shown to result in a surface morphology that is planar with occasional 2D islands, having an RHEED pattern that possesses the same symmetry as during deposition.[29]

4.4 Thermodynamic Model

The deposition of strained $In_{0.81}Ga_{0.19}As$ on top of an InGaAs buffer layer lattice matched to InP(001) has been shown to lead to the formation of a mixture of distinct surface reconstructions.[18, 33, 49, 73, 76] Figure 4.3 is a filled state (-2.99 V, 100 pA) 500 x 500 Å STM image of a h=30 ML

$In_{0.81}Ga_{0.19}As$/InP film deposited at T=485°C, R=0.5 ML/s, F_{As4}=2.5 ML/s, and V/III flux ratio=5. The atomic surface structure consists of a disordered (nx3) surface with domains of β2(2x4).

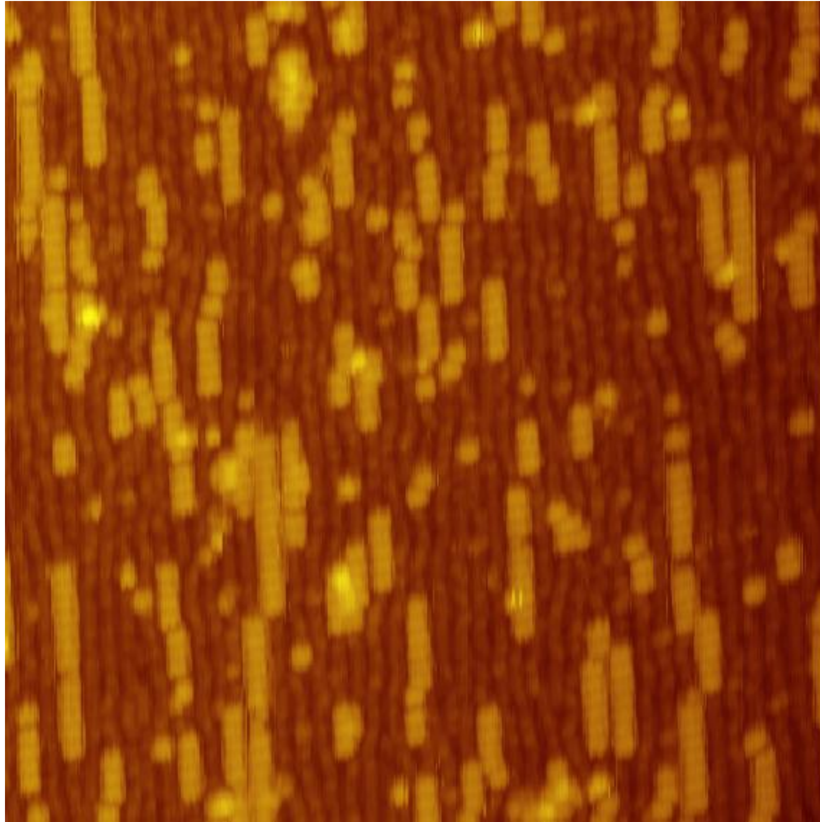

Figure 4.3: STM image of $In_{0.81}Ga_{0.19}As$ showing that the surface is comprised of areas of β2(2x4) surrounded by a disordered matrix of (4x3).

Considering only the difference in the surface energy of the two reconstructions, the fact that both the (2x4) and (nx3) reconstructions are present on the surface is surprising. Although there is still some uncertainty as to the details of the atomic arrangement of the (nx3) reconstruction, it has been suggested that the (nx3) phase has a somewhat higher surface energy than the

$\beta 2(2x4)$ phase across a wide range of surface energy conditions.[33] In this case, the (nx3) domain's surface energy should equal that of the $\beta 2(2x4)$ only for one chemical potential (or set of growth conditions). However, many groups report that the coexistence of $\beta 2(2x4)$ and (nx3) domains is robust over a large range of temperatures and compositions in InGaAs films.[18, 33, 49, 76]

It may be possible that the coexistence of these two reconstructions is due to the fact that the surface is rapidly quenched. That is, the mixture of the two phases represents a nonequillibrium condition. Annealing experiments show a decrease in the coverage of the (2x4) reconstruction as a function of annealing time and temperature.[29] However, XPS on those surfaces show that the In composition at the surface also decreases, presumably due to desorption of In.[29] Thus, it is unclear from those experiments whether the decrease in coverage is a result of equilibration, or a change in the surface composition, and thus a change in the equilibrium conditions more generally.

Instead we propose that the coexistence of these reconstructions is thermodynamically stabilized by the elastic relaxation between the reconstruction domains. The free energy of the surface containing multiple reconstruction domains has been shown to be $\Delta G = 2(x+y)\beta + xy\Delta\gamma + F_0 U(x,y)$ (Eqn. 4.5).[19] $F_0U(x,y)$ is the elastic relaxation energy, where F_0 is

the unit strain energy given by $F_0 = \frac{(1+\upsilon)f^2}{2\pi M}$, f is the magnitude of the difference in the stress between the reconstruction domains, M is the Young's modulus, and v is Poisson's ratio.[19, 81] The form of U(x,y) has been determined by Li and coworkers[81] using continuum elasticity for the case where an isolated rectangular domain is subjected to an isotropic biaxial stress and taking into account the elastic interactions of each of the domain boundaries, and is only a function of x and y.

Figure 4.4 represents a rectangular shaped domain similar to the β2(2x4) in a matrix of a different surface reconstruction like the disordered (nx3). In Fig. 4.4 x and y are the width and length of one of the β2(2x4) reconstruction along the [110] and $[1\bar{1}0]$ directions, respectively. The energy to form the boundary between the β2(2x4) and (nx3) domains (β) is highlighted in beige. The surface energy difference between the domain and the surrounding surface (Δγ) is highlighted in orange while the constant energy associated with the corners of the domain is highlighted in purple (E_c). The black arrows represent the elastic relaxation energy U(x,y).

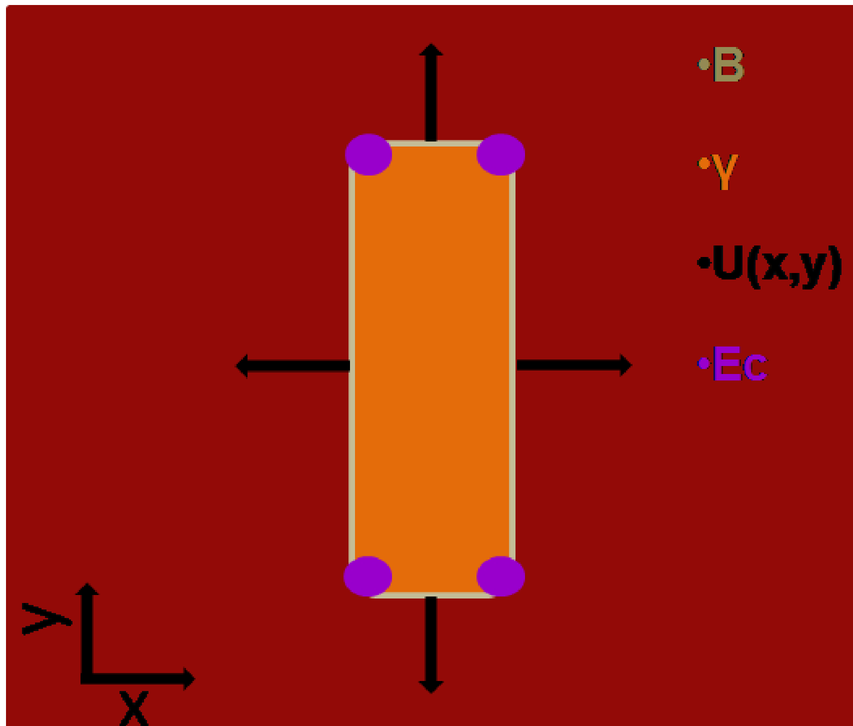

Figure 4.4: Schematic of a rectangular shaped reconstruction in a background matrix of a dissimilar reconstruction.

4.5 Discussion

This section details the importance of the elastic relaxation term in the thermodynamic model. The stability of the coexistence is compared in the model using both small and large elastic relaxation terms. A discussion of the effect anisotropy in the boundary energy term has on the geometry of the domains is also considered along with a comparison of the thermodynamic model with experimental data.

4.5.1 Importance of elastic relaxation in the thermodynamic model

Inspection of Eqn. 4.5 shows that the coexistence of reconstruction domains may be induced by the addition of elastic relaxation at the boundaries. Because the elastic relaxation term in Eqn. 4.5 is negative, this term will act to lower the total free energy of the system for $F_0>0$. Figure 4.5(a) is a contour plot of the total free energy as a function of the domain width and length for $\Delta\gamma=1$ meV/Å^2, $\beta=1$ meV/Å, $F_0=10$ meV/Å (Appendix A). The darker shades represent lower total free energies. Figure 4.5(a) shows that for small values of F_0, the positive surface energy and boundary energy terms dominate and there is a tendency for the domain to shrink (i.e. the coexistence is not favored). Figure 4.5(b) shows a plot of the total free energy as a function of the length (or width) of the domain for increasing domain areas (D=20 Å^2, 55 Å^2, 100 Å^2) (Appendix B). These values were chosen arbitrarily in order to illustrate the behavior of these equations. Black squares on the plot indicate where the domain shape is square. For small areas (D=20 Å^2 in Fig. 4.5a) the minimum energy occurs for a single value of the length (or width), that is, for square domains. As the domain size increases, the overall energy of the domain increases due to the increase in surface area and boundary length. Above some critical size, which is solely based upon the ratio of the boundary energy (β) and the elastic relaxation energy (F_0),[81] the stable shape becomes multivalued in length (or width), thus resulting in a rectangular domain. In fact

for domains with an area confined to D=55 Å^2 and 100 Å^2 as seen in Fig. 4.5(b), the square shaped domains sit at a local maximum. In the case of small values of F_0, the only way to observe the coexistence of reconstruction domains is if the kinetics of the system are such that global equilibrium cannot be achieved. This may be the case if the system is quenched, thus freezing in the metastable state, or if other kinetic factors, such as anisotropic diffusivity, prevent the system from reaching equilibrium.

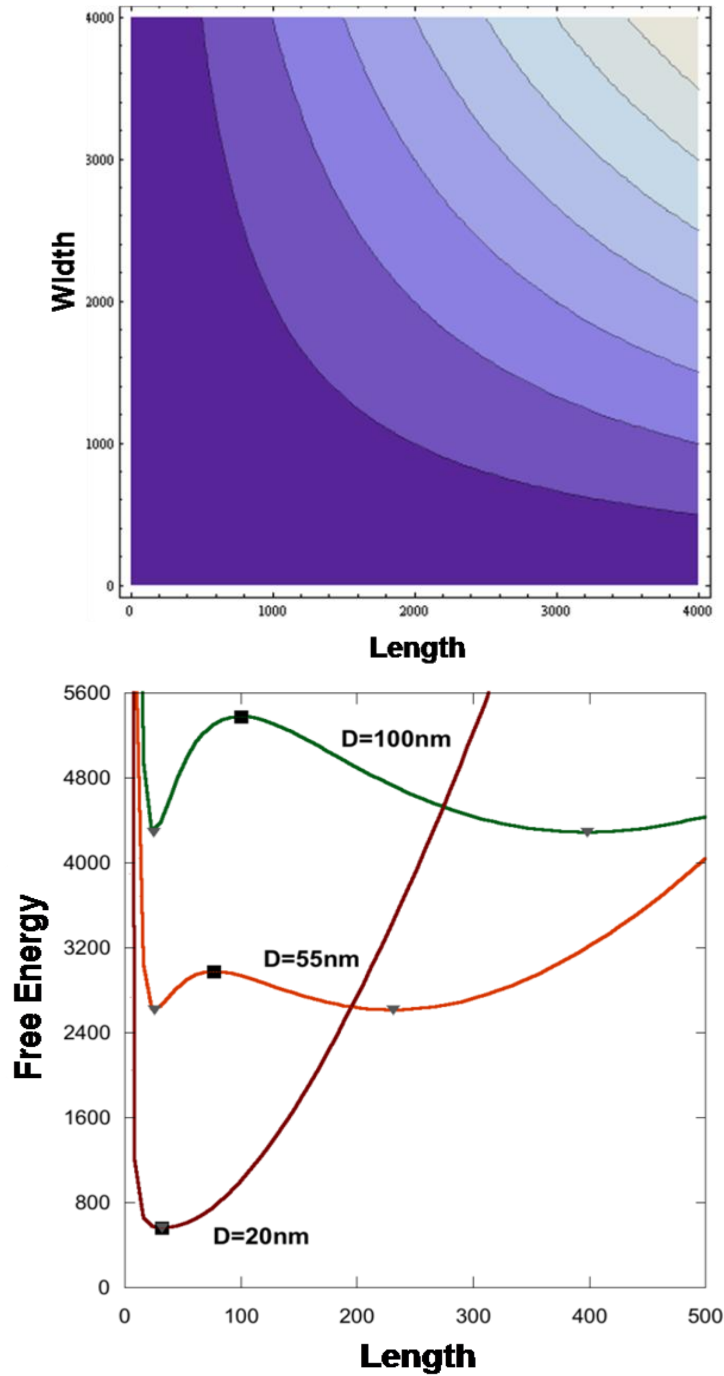

Figure 4.5: (a) Contour plot of the total free energy as a function of the domain width and length for $\Delta\gamma$=1 meV/Å^2, β=1 meV/Å, F_0=10 meV/Å. The darker shades represent lower total free energies. (b) Plot of the total free energy as a function of the length (or width) for increasing domain areas (D=20 Å^2, 55 Å^2, 100 Å^2). These values were chosen arbitrarily in order to illustrate the behavior of these equations. Black squares and gray triangles on the plot indicate where the domain shape is square and rectangular, respectively.

For larger values of F_0 the elastic relaxation is such that the coexistence of the surface reconstruction domains is globally stable. Figure 4.6(a) is a contour plot of the total free energy as a function of the domain width and length for $\Delta\gamma$=1 meV/Å^2, β=1 meV/Å, F_0=30 meV/Å (Appendix A). Again, the darker shades represent lower total free energies. Figure 4.6(a) shows that for larger values of F_0, the elastic relaxation energy terms dominate and the coexistence of domains is stabilized when the reconstruction takes on a rectangular shape. Figure 4.6(b) shows a plot of the total free energy as a function of the length or width of the domain for increasing domain areas (Appendix B). Overall, the energy decreases with increasing domain area, indicating that larger domain sizes are more stable, and that coexistence of reconstruction domains is thermodynamically favored. As before, there is a critical size above which rectangular domains are stabilized, as indicated by the square dots in Fig. 4.6(b). If the system is allowed to reach equilibrium, the domains would continue to grow in area, and take on a shape that is infinitely long and vanishing narrow. In other words, the equilibrium reconstruction domain shape is a quantum wire.

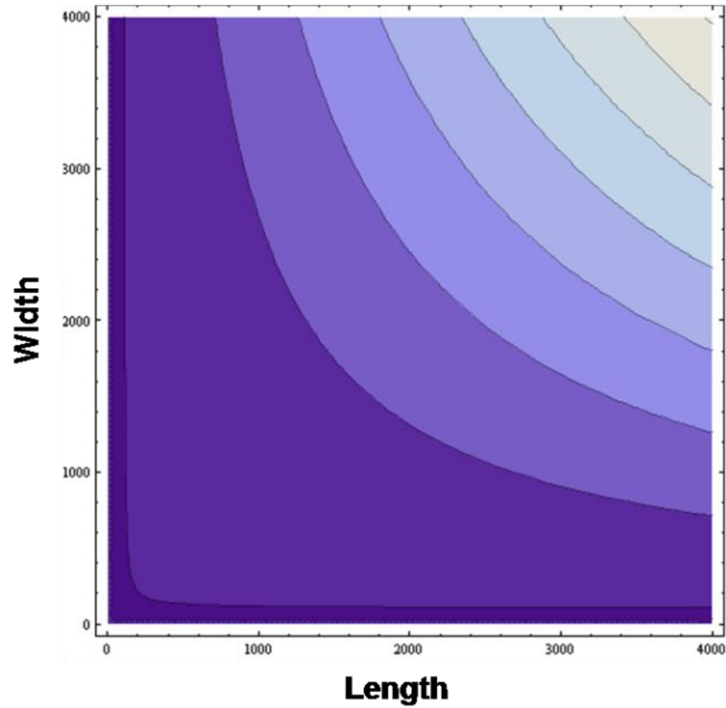

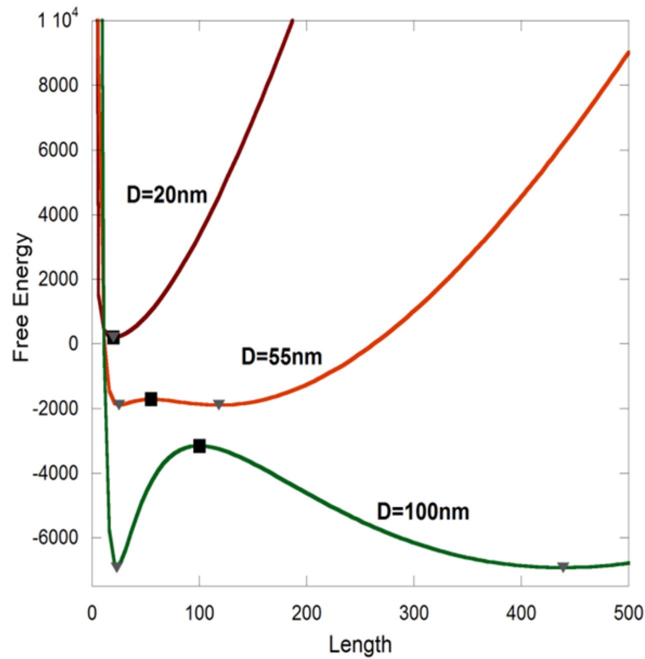

Figure 4.6: (a) Contour plot of the total free energy as a function of the domain width and length for $\Delta\gamma$=1 meV/Å^2, β=1 meV/Å, F_0=30 meV/Å. The darker shades represent lower total free energies. (b) Plot of the total free energy as a function of the length (or width) for increasing domain areas (D=20 Å^2, 55 Å^2, 100 Å^2). These values were chosen arbitrarily in order to illustrate the behavior of these equations. Black squares and gray triangles on the plot indicate where the domain shape is square and rectangular, respectively.

4.5.2 Anisotropy in the boundary energy term

In the discussion so far, the boundary energy is assumed to be isotropic; anisotropy in this term, however, eliminates the appearance of square domains all together. Figure 4.7 shows plots of the length and width of the domains as a function of domain size for $\Delta\gamma$=1 meV/Å^2, F_0=30 meV/Å, β_x=1 meV/Å, and varying β_y. For an isotropic boundary energy ($\beta_x = \beta_y$ indicated by the solid line in Fig. 4.7), the length and width are equal for sizes below the critical domain size. For large domains, however, the length and width take on dissimilar values (rectangular domains) with increasing size, and the aspect ratio (domain length/domain width) also increases with increasing size. This reflects the ability of the elastic relaxation term to lower the total energy of the system. For anisotropic boundary energy, that is when ($\beta_x \neq \beta_y$ indicated by the hashed lines in Fig. 4.7), square domains are not stable for any domain size. Instead, the length and width of the domains are never equal, and the aspect ratio always increases with size.

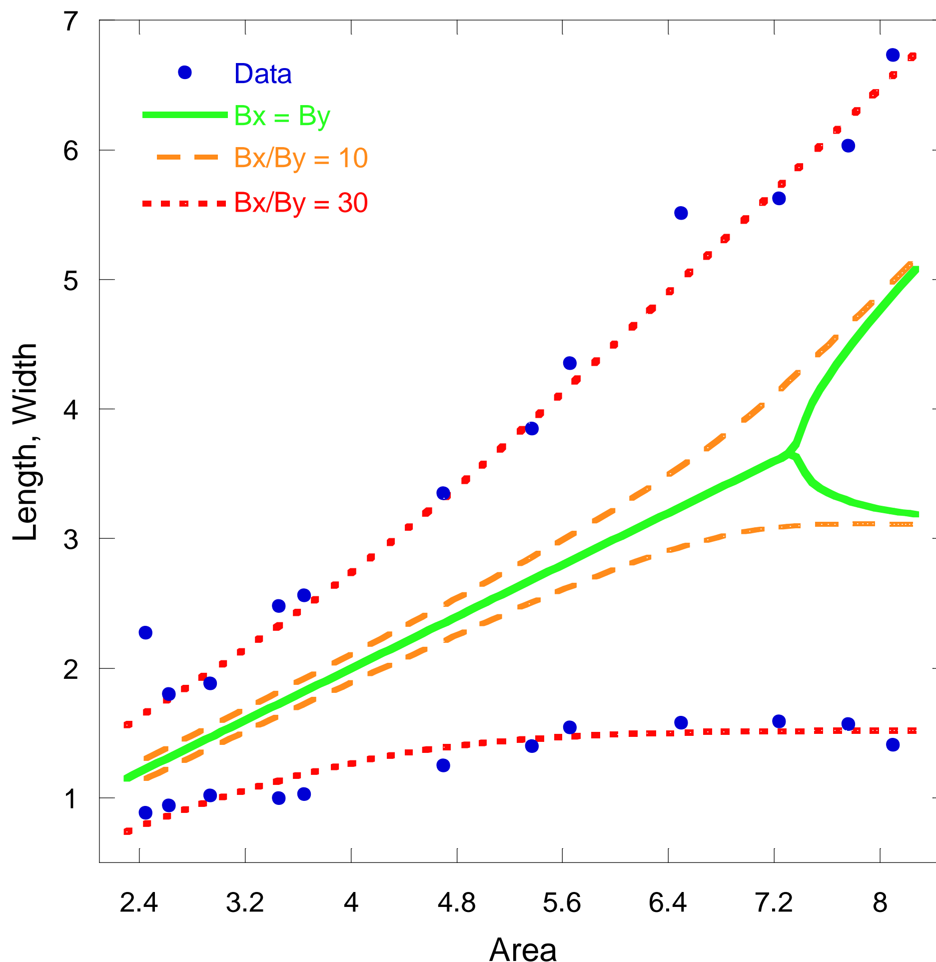

Figure 4.7: Plot of the experimental data (dots) for the dependence of the length and width of the domains as a function of area for films deposited at T=505°C, R_{Ga}= 0.5 ML/s, h=20 ML, and V/III flux= 5. The solid line was produced using the model for isotropic domains with $\Delta\gamma$=1 meV/Å^2, β_x=1 meV/Å, β_y=1 meV/Å, F_0=30 meV/Å, a=1.9 Å, ν=0.3. Dashed lines were produced using the model for anisotropic boundary energies ($B_{x/}$ B_y=10 and $B_{x/}$ B_y=30).

Our experimental results are consistent with this thermodynamic picture. Figure 4.7 also plots the experimental data for the dependence of the length and width of the domains as a function of area for films deposited at T=505°C. The experimental data agrees well with the model for $\Delta\gamma$=1 meV/Å^2, β_x=1

meV/Å, β_y=30 meV/Å, F_0=30 meV/Å, a=1.9 Å, ν=0.3. These values were chosen as a best fit of our data, however, they are consistent with those found for other systems. For example, the unit strain energy for the coexistence of the (1x1) and (7x7) reconstructions in Si was found to be 35.65 meV/Å,[82] close to the value of 30.0 meV/Å used for the model that best fits our experimental data. The value for the change in the surface energy between the (nx3) and the β2(2x4) is not known, however, the dependence of the domain shape is not very sensitive to this value. A more precise determination of the β and F_0 will require additional experiments and *ab initio* calculations. Nonetheless, these results show that the form of the equation predicts the shape distribution of the reconstruction domains reasonably well.

The boundary anisotropy varies with the growth temperature. Figure 4.8 is a plot of the boundary energy anisotropy of the β2(2x4) reconstructions as a function of temperature. The points were obtained by fitting the experimental data to Eqn. 1, assuming that $\Delta\gamma$=1 meV/Å^2, β_x=1 meV/Å, F_0=30 meV/Å, and varying β_y. Figure 4.8 shows that the anisotropy of the boundary energy more than doubles over a 70° temperature increment. This temperature dependence of the boundary energy is consistent with results for the stiffness of silicon steps,[83] and indicates that the configurational entropy along the $[1\bar{1}0]$ direction is higher than for the [110].

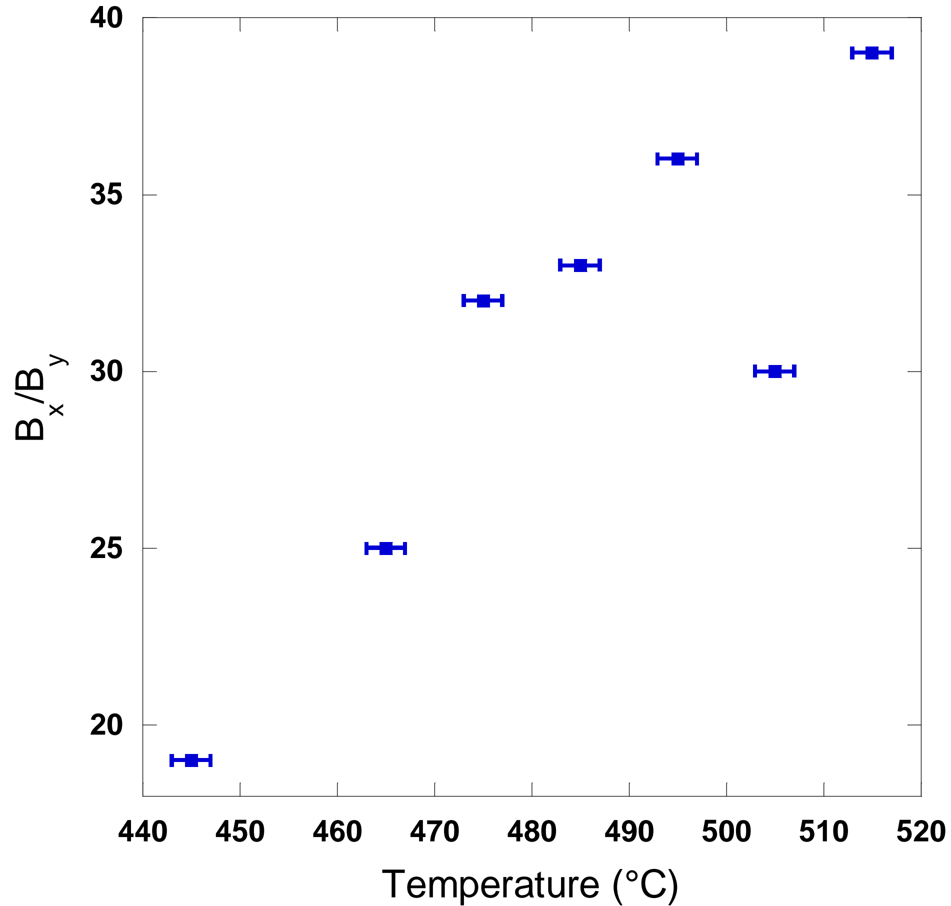

Figure 4.8: Plot of the boundary energy anisotropy as a function of growth temperature. The points were obtained by fitting the experimental data to Eqn. 4.5, assuming that $\Delta\gamma$=1 meV/Å^2, β_y=1 meV/Å and F_0=30 meV/Å.

Ultimately, the β2(2x4) domains want to reach an equilibrium shape that will provide the greatest amount of elastic relaxation. As a result of the boundary energy anisotropy, this shape will tend towards domains that are infinitely long along the $[1\bar{1}0]$ and vanishingly narrow along the [110]. This would effectively result in the self-assembly of a nanoscale 1D pattern on the surface of $In_{0.81}Ga_{0.19}As$/GaAs films. Prior work has shown that long and narrow reconstruction domains associated with lateral composition modulation

do form, and persist on very rough surfaces as well[84] suggesting that controlling the shape and distribution of these domains can result in nanostructure formation. More work will be needed in this area to better understand under what conditions this 1D pattern formation is allowed to form.

4.6 Conclusions

The deposition of InGaAs, strained 1.9% in compression with respect to the substrate, leads to a surface composed of a (nx3) reconstruction with domains of β2(2x4). The conclusions of this chapter are summarized as follows:

(1) This work shows that a combination of thermodynamic models from Li and Tromp may be applied to the size distribution of reconstructions in heteroepitxial films.

(2) This demonstrates the importance of the boundary anisotropy on the formations of nanostructures in the plane of the terrace.

(3) For large unit strain energy, this coexistence is globally stable with an equilibrium domain shape that is infinitesimally narrow and infinitely long.

(4) Experimental data is consistent with this picture, showing that the shape of the domains becomes more anisotropic with increasing domain size and growth temperature.

Chapter 5

Pit Nucleation During the Growth of Compressively Strained $In_{0.81}Ga_{0.19}As$/InP(001) Layers

5.1 Introduction

The growth of heteroepitaxial films with a moderate (~2%) lattice mismatch usually occurs in the Stranski-Krastanov (SK) mode,[85] where planar wetting layers initially form followed by the nucleation and growth of coherent three-dimensional (3D) features above some critical thickness. Theoretically, both islands and pits can relieve strain,[86] but experimentally only islands are typically observed as the initial mechanism of strain relief.[87] The difficulty associated with the formation and growth of pits is in their ability to reach a critical size for stable growth. Because the growth of a pit requires that atoms are removed, a growth flux tends to annihilate the pit before it reaches a critical size. The formation of pits on the surface has been observed to occur under certain circumstances nonetheless. Pits have been shown to form on the surface of $In_{0.27}Ga_{0.73}As$/GaAs(001) films, but not until after island nucleation.[88] In this case, the islands act as sinks for atoms on the surface, reducing the average number of adatoms in their vicinity thus increasing the

likelihood of pit formation. Pits also have been reported in the SiGe systems under kinetically limited growth conditions; that is, at relatively high growth rates and low temperatures.[89] Bouville and coworkers have shown that materials parameters such as lattice mismatch and surface energy, or growth conditions such as temperature and growth rate can significantly impact the type of 3D features present on the surface and its subsequent development.[86]

The aim of this study is to show that there is a growth regime in lattice mismatched films of $In_{0.81}Ga_{0.19}As$/InP(001) where pits rather than islands form on the surface above a critical thickness. This result demonstrates experimentally that islands and pits are analogous structures and that the SK growth mode can result in different types of morphological feature evolution, depending on the materials parameters and growth conditions. The ability to control the type of features that assemble during growth will provide new pathways for achieving novel nanostructures.

The remainder of this chapter is structured as follows. **Section 5.2 ("Background")** presents a comprehensive overview of Stranski Krastanov growth in strained heteroepitaxial films. **Section 5.3 ("Experimental Procedure")** details the film growth and sample characterization procedures for the InGaAs films used for this study. **Section 5.4 ("Pit Nucleation During the Growth of Compressively Strained $In_{0.81}Ga_{0.19}As$/InP(001) Layers")**

presents in detail the experimental results and statistical analysis of nucleation and growth of pits during the growth of thin films of $In_{0.81}Ga_{0.19}As$. Particular attention is given to the surface coverage and geometry of the pits and its dependence on total film thickness (Section 5.4.1), growth temperature (Section 5.4.2), and growth rate (Section 5.4.3). The experimental results from Section 3.4 are the discussed in detail in **Section 5.5 ("Discussion")** paying particular attention to strain relaxation, surface energy and their correlation with the nucleation and growth of pits. The main conclusions of this chapter are summarized in **Section 5.6 ("Conclusions")**.

5.2 Background

The deposition of thin films on crystalline substrates using MBE can occur in one of three primary growth modes: Frank-van der Merwe, Volmer-Weber, or Stranski-Krastanov. Frank-van der Merwe growth describes two-dimensional layer-by-layer growth in films with little to no lattice mismatch. Volmer-Weber describes the three-dimensional growth of highly mismatched or otherwise dissimilar thin films. For films grown with similar materials and a moderate lattice mismatch a two step Stranski-Krastanov growth mode is common. In the case of the SK growth mode flat two-dimensional layers are initially deposited followed by a transition to three-dimensional growth above a

critical thickness (t_{SK}). This growth mode has been the subject of numerous studies involving metal and semiconducting materials, including $In_xGa_{1-x}As$ alloys.

The SK growth mode has been observed experimentally for a variety of $In_xGa_{1-x}As$ alloys.[14, 46, 54, 74, 90-93] The SK transition is an energetically driven, but kinetically limited process. The islands form from a planar surface in order to reduce the strain energy of the film, when the amount of energy relieved surpasses the cost associated with the creation of new surface. In fact, the SK transition can be eliminated altogether in $In_xGa_{1-x}As$ alloys grown on GaAs(001) substrates when $x<0.20$ as a result of the low misfit.[14, 91] In $In_xGa_{1-x}As$ alloys where the SK transition does occur typically only islanding is observed above the critical thickness.[87] Figure 5.1 shows a three-dimensional view of quantum sized islands that have nucleated on the surface of $In_{0.25}Ga_{0.75}As$/GaAs(001) above the SK transition.[90] Similar observations of SK growth has been observed in other $In_xGa_{1-x}As$/GaAs(001) alloys with a moderate lattice mismatch.

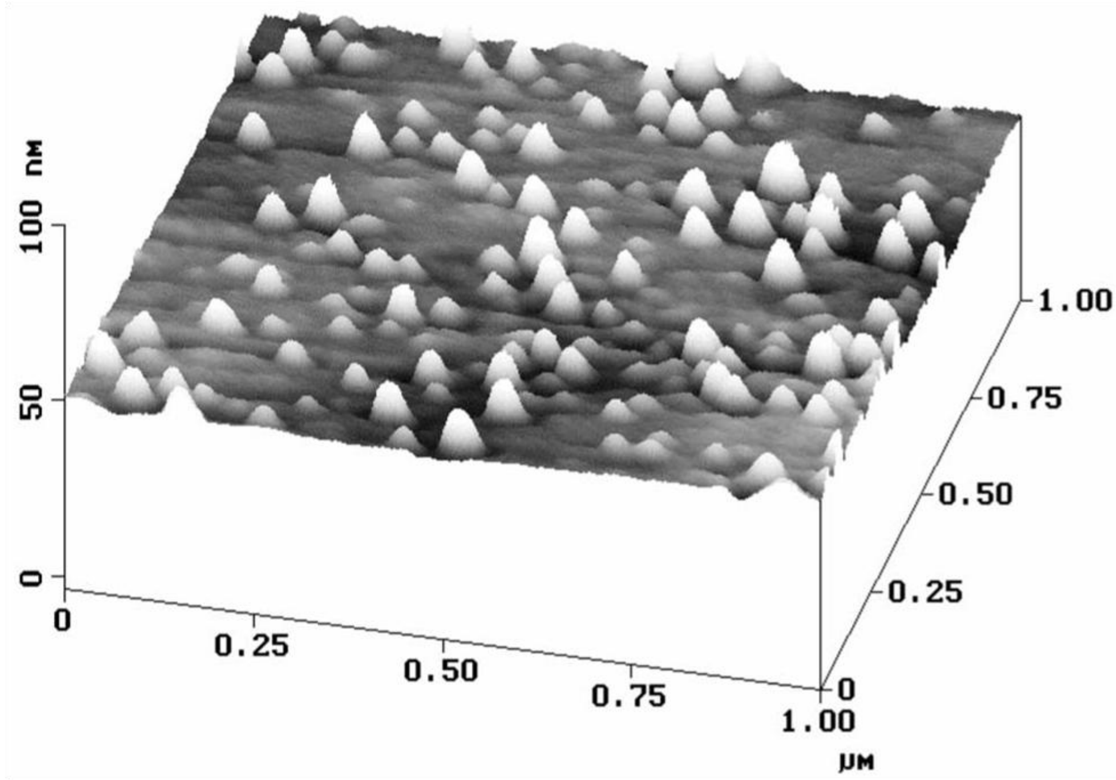

Figure 5.1: 3D AFM image of pits forming on the surface of $In_{0.25}Ga_{0.75}As/GaAs(001)$ above t_{SK}.[90]

Theoretically, both islands and pits can relieve strain. Figure 5.2 is a cross section of the shapes assumed for islands or pits above t_{SK}. The shape of pits are geometrically the inverse of islands and the effect of strain relaxation in the film is similar as well.[87] The morphological development during deposition would also be similar, with flat layer-by-layer growth followed by the nucleation and growth of islands above a critical thickness.

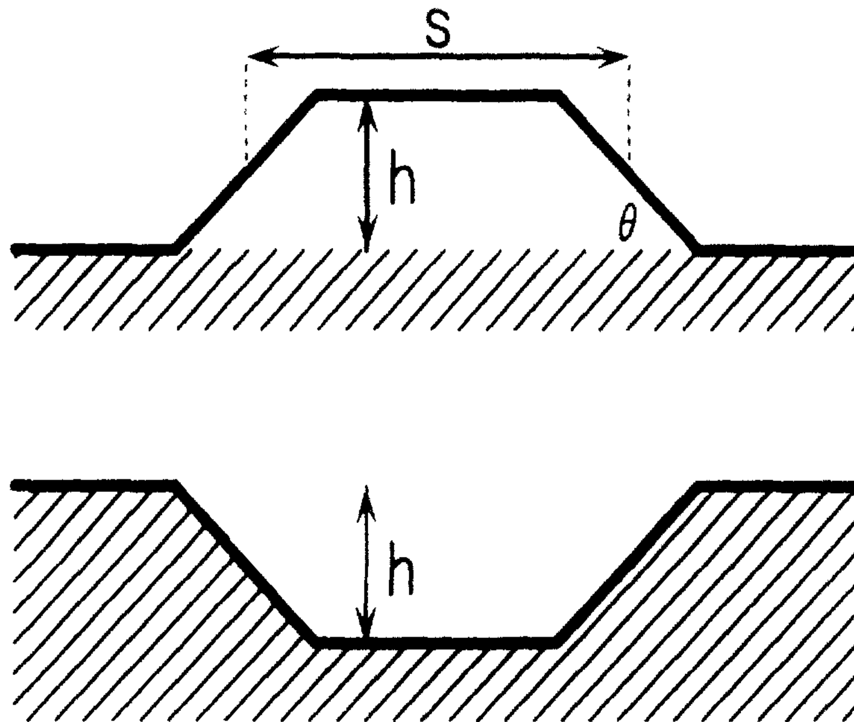

Figure 5.2: Cross-sectional view of the shape assumed for islands or pits on the surface of moderately strained films above t_{SK}. Length and height are denoted by s and h, respectively. Edges are oriented at an angle θ with respect to the surface of the film. [87]

The difficulty for pit formation is in their ability to reach the critical size during growth. Because the growth of a pit requires that atoms are removed, a growth flux tends to annihilate the pit before it reaches a size that is stable. Nonetheless, the formation of pits on the surface has been observed to occur under certain circumstances. Pits have been shown to form on the surface of $In_{0.27}Ga_{0.73}As$/GaAs(001) films, but typically they do not appear until after island nucleation. Figure 5.3 a-c shows a typical sequence in the evolution of the surface morphology of $In_{0.27}Ga_{0.73}As$/GaAs(001) grown at different

thicknesses. The morphology of the film at h=31 ML (Fig. 5.3(a)) consists of a flat wetting layer, on top of which 3D islands have begun to nucleate, indicating that the critical thickness for island formation already has been exceeded. At h=42 ML (Fig. 5.3(b)) the density of 3D islands increases, and the islands begin to coalesce locally. At h=47 ML (Fig. 5.3(c)) the surface is contains a high density of close-packed islands. Also apparent in this image are the pits that form only adjacent to clusters of islands. At even greater thicknesses (not shown), the islands and pits coalesce into ripple arrays aligned along the $[1\bar{1}0]$.[88] Thus, the nucleation and growth of pits in this system occurs only after islands have developed on the surface.

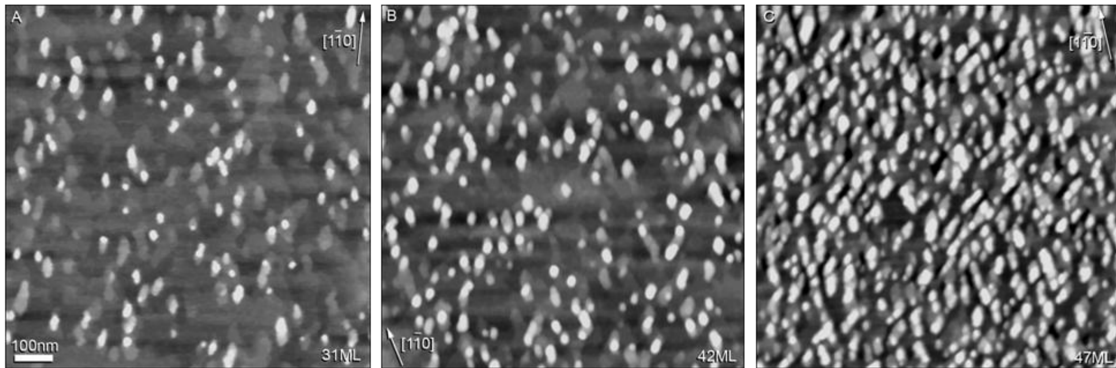

Figure 5.3: 1x1 μm AFM images of $In_{0.27}Ga_{0.73}As/GaAs$ films grown at grown at T=485°C, R=1.1 ML/s, and V/III flux ratio=4 at film thicknesses as noted. The height scale is 15 nm for (a) and (b) and 20 nm for (c).[94]

Pitting prior to island nucleation has been reported in other material systems such as SiGe, but typically these pits are only observed under kinetically limited growth conditions, that is at relatively high growth rates and low temperatures.[89] Nonetheless, a theoretical model by Bouville *et. al.* has shown that materials parameters such as lattice mismatch and surface energy, or growth conditions such as temperature and growth rate can significantly impact the type of 3D features present on the surface at equilibrium and predicts that there is a growth regime where pits should nucleate before islands.[86]

Adatom concentration (η) is the key to understanding the nucleation of pits on the surface of III-V films grown at equilibrium. Figure 5.4 shows how

η varies between two islands separated by a distance $2l$. The adatom concentration is lowest at the edge of an island (η_{edge}) because the islands act as a sink for the adatoms impinging on the surface during deposition. If the adatom concentration is too high then pits will not nucleate and grow before incoming adatoms fill the void. Thus pits cannot nucleate or grow at adatom concentrations above a threshold value, defined as η_{ceil}. If η_{ceil} is lower than η_{edge} pitting is precluded everywhere on the surface. If η_{ceil} is higher than η_{edge} but lower than η_{mid} (defined as the adatom concentration midway between two islands) pitting will occur on the surface but only adjacent to islands. When η_{ceil} is higher than the adatom concentration everywhere on the surface then pitting is delocalized and can nucleate and grow even in the absence of islands.[86]

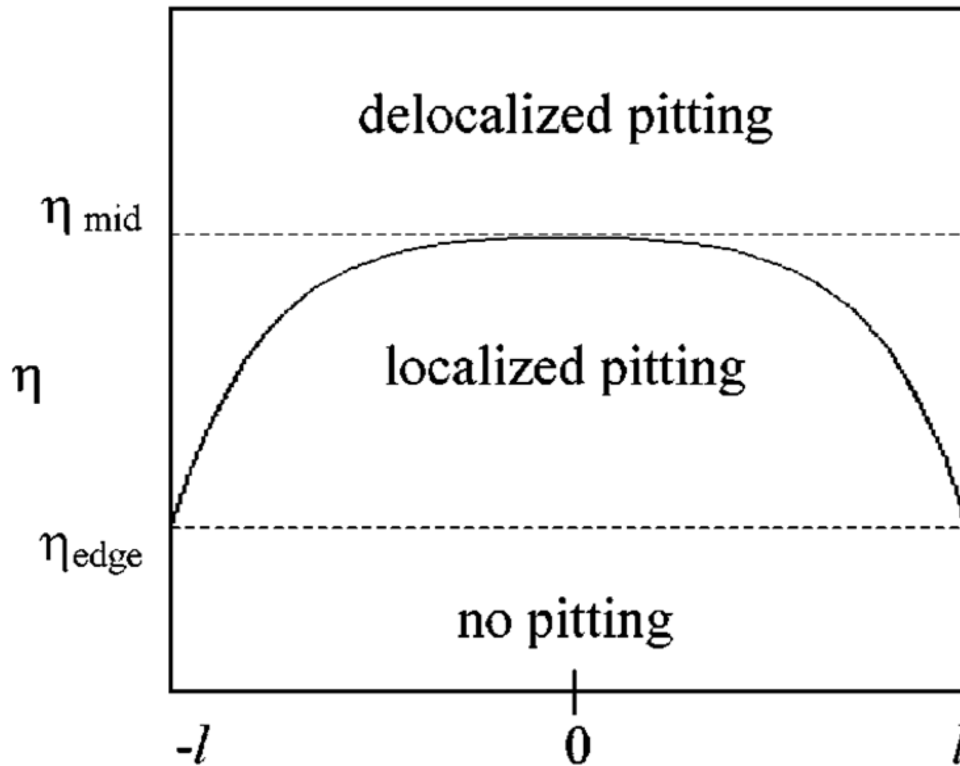

Figure 5.4: Graph showing the variation of the adatom concentration η between two islands separated by a distance 2*l*, as a function of position.[86]

Material parameters and growth conditions such as lattice mismatch and surface energy can also impact the surface morphology and the ability for pits to form on the surface. Figure 5.5 shows where different morphological regimes will form as a function of surface and strain energy. At low mismatch and high surface energies neither islands nor pits nucleate and the film remains planar (regime 0). As the surface energy decreases pits can form but only adjacent to pits (regime IA) and at even lower surface energies pitting can occur delocalized to any island formation (ID). As the surface energy

continues to decrease pits can nucleate and grow even before islands form (regime P). Thus, this model predicts that there is a regime where pits will nucleate and grow on the surface before islands as the primary mechanism of strain relaxation in films above t_{SK}.[86] The model also predicts that material systems with a high mismatch are more likely to form pits as the driving force (elastic energy relaxation) is higher. However, films grown with a high lattice mismatch also have a low critical thickness such as InAs/GaAs where the t_{SK} is on the order of 1-2 ML. Therefore, pitting may be prevented in highly mismatched films due to a lack of material to support the pit.[95]

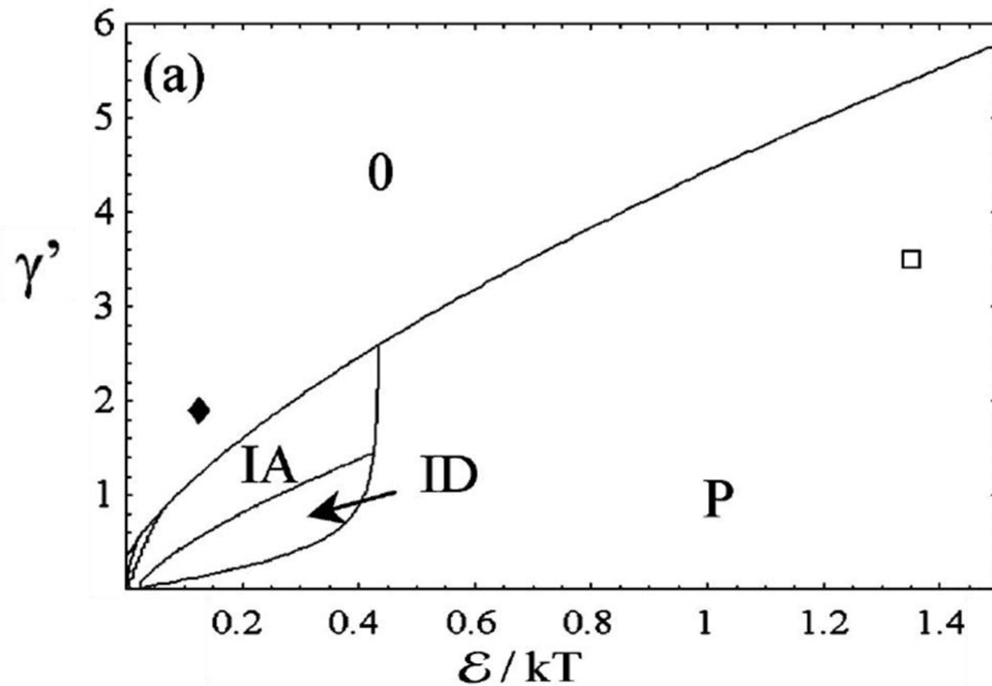

Figure 5.5: Graph showing predicted domains of several morphological regimes as a function of surface and strain energy. Two experimental systems are denoted for comparison, $In_{0.27}Ga_{0.73}As$/GaAs (♦) and InSb/InAs (□). The geometry of the pits is accounted for in the evaluation of the surface energy.[86]

Deposition rate and growth temperature can also affect the surface morphology. Figure 5.6 is a graph showing the predicted experimental growth regimes as a function of deposition rate and growth temperature for a single materials system. The model predicts several different surface morphologies for a given set of growth conditions. For the lowest growth rates and temperatures the film is expected to remain planar with neither pits nor islands nucleating on the surface. As the growth temperature increases and the

deposition rate remains low, the nucleation and growth of pits alone is expected.[86]

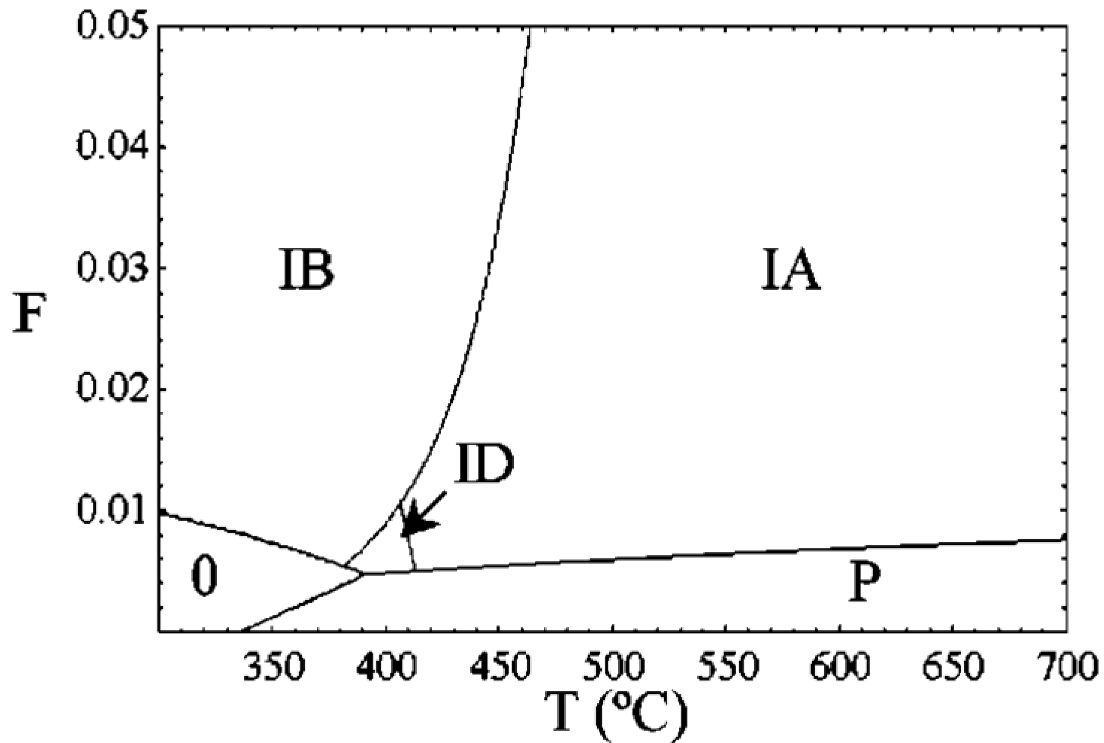

Figure 5.6: Graph showing various predicted morphology regimes as a function of growth temperature and deposition rate.[86]

Thus pitting is predicted to nucleate instead of islands on the surface of strained thin films as the initial strain relief mechanism although experimentally only islands are typical seen first. Pits are known to grow on the surface, but only after islands have developed or during kinetically limited growth.

5.3 Experimental Procedure

Samples were grown using a molecular beam epitaxy system with solid source In and Ga cells and a valved cell for As_4. The growth rates were calibrated using reflection high-energy electron diffraction (RHEED) intensity oscillations, and growth temperature was monitored using a pyrometer, calibrated by observing the temperature at which the oxide desorption for an InP(001) substrate occurs. The substrates were initially heated to a temperature T=530°C under a typical As_4 growth flux of F_{As4} = 2.2 monolayers per second (ML/s) to remove the oxide layer, after which the temperature was immediately lowered to T=485 °C. A 0.5 μm thick $In_{0.53}Ga_{0.47}As$ buffer layer lattice matched to InP(001) was deposited at a total group III growth rate R=0.5 ML/s, which results in a planar surface morphology as verified by *ex situ* atomic force microscopy (AFM). After deposition of the buffer layer, the samples were annealed for 20 minutes while ramping to the In cell temperature required for the deposition of the strained InGaAs films. The $In_{0.81}Ga_{0.19}As$ films, which possess a lattice mismatch of 1.9% in compression with respect to the substrate ($f = (a_f - a_s)/a_s$ being the lattice misfit with a_f and a_s representing the lattice parameter of the film or substrate, respectively) were grown to thicknesses $40<h<70$ ML, as noted. Growth temperatures for the $In_{0.81}Ga_{0.19}As$ films vary between $475 \leq T \leq 515$ °C and growth rates vary between $0.5 \leq R \leq 1.25$ ML/sec, as noted. The film composition for both the lattice-matched buffer

layer and the $In_{0.81}Ga_{0.19}As$ film was verified post growth by characterizing thick samples using X-ray diffraction (XRD).

The $In_{0.27}Ga_{0.73}As$ films, which also possess a lattice mismatch of 1.9% in compression relative to the GaAs(001) substrate, were grown on top of a GaAs buffer layer at T=485°C, R=1.1 ML/sec, and to thicknesses $31<h<47$ ML as noted. At the end of growth, all samples were quenched under the same As_4 flux used during growth resulting in a film possessing the same RHEED pattern upon cooling as the film possesses during deposition. This procedure was found to maintain the gross features of the surface structure present during growth.[84] Once cooled the samples were transferred *in vacuo* to a scanning tunneling microscope (STM) (-2.88 V, 100 pA) for analysis. All the samples were also characterized *ex situ* using AFM.

5.4 Pit Nucleation During the Growth of Compressively Strained $In_{0.81}Ga_{0.19}As$/InP(001) Layers

This section presents results from the nucleation and growth of pits on the surface of $In_{0.81}Ga_{0.19}As$. The presence of these pits are observed as a function of film thickness, growth temperature, and growth rate. Information about the surface coverage, density, and size statistics are also presented in this section.

5.4.1 Dependence on Film Thickness

The surface energy, which in the case of InGaAs is altered by the In composition, dictates whether islands or pits appear above the critical thickness for a given lattice mismatch. A comparison of the island sizes and densities of the $In_{0.27}Ga_{0.73}As$/GaAs(001) films grown at different thicknesses shown in Fig. 5.3 is given in Table 5.1. Both the island surface coverage and the island density increase more than three-fold when the film thickness increases from 31 ML to 47 ML. The average island length in the $[1\bar{1}0]$ increases slightly while the vertical aspect ratio (defined as the height or depth in the [001] divided by the length in the $[1\bar{1}0]$) remains nominally constant. The lateral aspect ratio, defined as the length of the pit or island in the $[1\bar{1}0]$ relative to the [110], increases with increasing thickness as a result of island coalescence. Pits appear on these films for h = 47 ML, but only adjacent to the islands. These pits are small relative to the islands and cover less than one percent of the surface. At even greater thicknesses (not shown), the islands and pits coalesce into ripple arrays aligned along the $[1\bar{1}0]$.[93, 96] Even though it has been shown theoretically that pits are just as efficient at relieving lattice mismatch strain as islands,[97] the formation of pits is hampered during deposition as the incoming flux tends to annihilate the pits before they reach critical size. This tendency may be overcome in the vicinity of islands where the adatom

concentration is depleted,[93] thus resulting in morphologies consisting of both islands and pits as seen in Fig. 5.3(c).

	31ML	**42ML**	**47ML**
Density	115±10.9 um^{-1}	191±4.2um^{-1}	358±5.0um^{-1}
Coverage	10.5±1.2%	22.8±1.7%	50.8±0.6%
Length $[1\bar{1}0]$	32.9±7.1nm	34.2±3.3 nm	41.4±3.1 nm
Lateral Aspect Ratio	2.5±0.56	2.49±0.32	2.9±0.43
Vertical Aspect Ratio	0.46±0.07	0.44±0.06	0.48±0.05

Table 5.1: Comparison of islands on the surface of $In_{0.27}Ga_{0.73}As$ shown in Figure 5.3 (a)-(c).

$In_{0.81}Ga_{0.19}As$/InP films have the same lattice mismatch (f=1.9%) as the $In_{0.27}Ga_{0.73}As$ /GaAs films, but exhibit a completely different morphological evolution in keeping with an “inverse” SK growth mode. While both the $In_{0.27}Ga_{0.73}As$/GaAs and $In_{0.81}Ga_{0.19}As$/InP samples are planar below the critical thickness, the $In_{0.81}Ga_{0.19}As$ films favor 3D pitting instead of 3D island formation at higher thicknesses. Figure 5.7 shows a series of AFM micrographs of $In_{0.81}Ga_{0.19}As$/InP(001) films deposited with increasing thickness from 40 ML $\leq$ h $\leq$ 50 ML. The dimensions and density of the pits seen on the surface in

Fig. 5.7 are given in Table 5.2. At thicknesses just above the SK transition (Fig. 5.7(a)) the surface is comprised of a flat wetting layer onto which a couple of small pits have begun to nucleate.

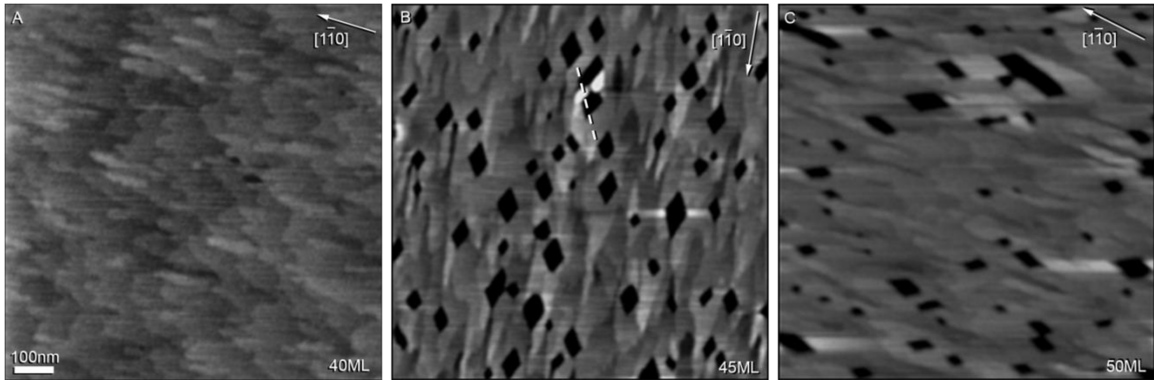

Figure 5.7: A series of 1x1μm AFM images comparing the development of the surface morphology on the surface of $In_{0.81}Ga_{0.19}As$ grown at T=515°C, R=1.2 ML/s, and V/III flux ratio=4 for various thicknesses as noted. Dashed line (b) denotes the location of line scan shown in Fig. 5.8.

	40ML	**45ML**	**50ML**
Density	0.33±0.09um^{-1}	55.2±4.91um^{-1}	72.7±6.23um^{-1}
Coverage	0.10±0.07%	8.46±0.56%	9.81±0.44%
Length [$1\bar{1}0$]	16.1±2.8nm	65.4±4.4nm	111.9±17.2nm
Lateral Aspect Ratio	1.37±0.23	2.65±0.34	3.94±0.38
Vertical Aspect Ratio	0.23±0.04	0.19±0.01	0.12±0.03

Table 5.2: Comparison of pits on the surface of $In_{0.81}Ga_{0.19}As$ shown in Figure 5.7.

At higher thicknesses, many diamond-shaped pits are observed with the side walls 26° away from the [$1\bar{1}0$]. Figure 5.8 is a line scan of pits and an island shown in Fig. 5.7(b). This, combined with other line scans, reveal that

interior walls make angles of ~81° or ~98° angles with respect to the (001) plane. Together this data suggests that the pit walls are {136}, in agreement with previous reports of the shape of islands and pits in the $In_xGa_{1-x}As$ system.[96]

The surface coverage of the pits increases with increasing thickness, in this case by two orders of magnitude to almost 10% of the surface at 50 ML. At higher thicknesses (Fig. 5.7(c)) the pits begin to coalesce along the $[1\bar{1}0]$ direction, as can be seen with the islands in Fig. 5.3(c). This morphological evolution is analogous to the nucleation, growth, and coalescence observed for material systems for which islands initially nucleate. One possible explanation for the formation of pits is the presence of threading dislocations in the strained film either coming up from the buffer layer or originating in the film itself. However X-ray diffraction confirms that the buffer layer is lattice matched to the substrate.

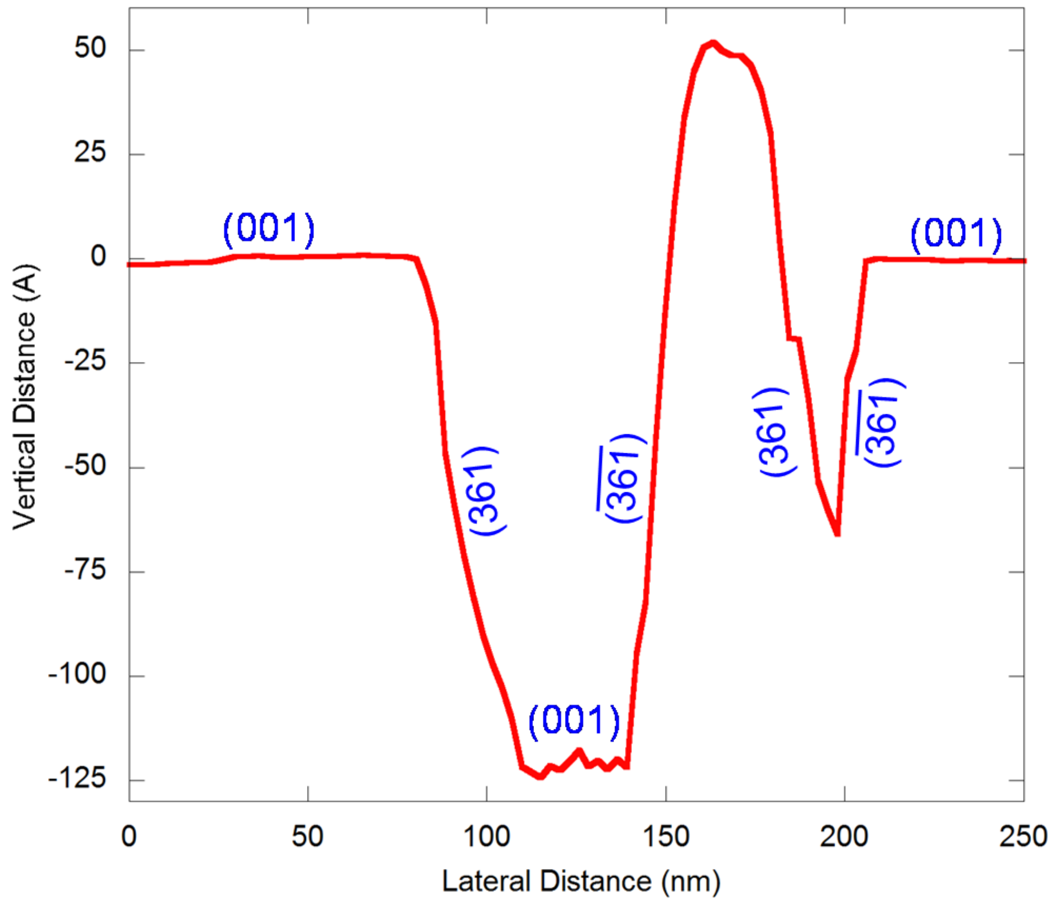

Figure 5.8: Line scan of the island and pits denoted by the dashed line in Fig. 5.7(b). Facets are indicated in blue.

Transmission electron microscopy (TEM) was used to determine if the pits are a result of dislocations in the film. Figure 5.9 is a cross-sectional TEM image of a 0.5 µm thick $In_{0.81}Ga_{0.19}As$ layer grown at T=505°C, R=1.2 ML/s, and V/III flux ratio=4. This image shows a large pit that has formed in the $In_{0.81}Ga_{0.19}As$ as denoted by the arrow. This pit terminates a few monolayers before the buffer layer begins, consistent with previous observations. A portion

of the $In_{0.53}Ga_{0.47}As$ buffer layer is also shown in Fig. 5.9 in the lighter grey regions. This, combined with other cross-sectional TEM images, do not show any evidence dislocations under the pits. This suggests that these pits are not the result of dislocations and are the result of some other phenomena that will be discussed in Section 5.5.

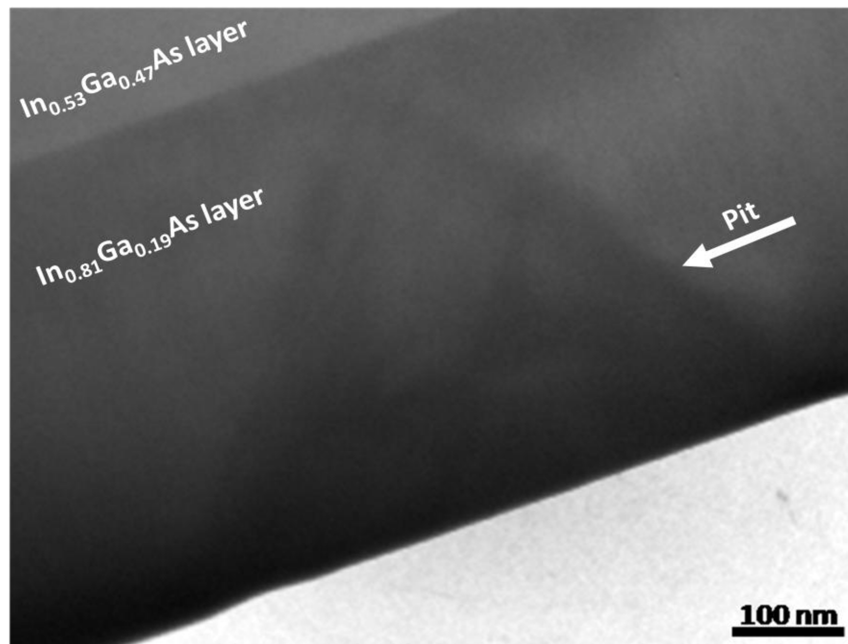

Figure 5.9: Cross-sectional TEM image of a 0.5 μm thick $In_{0.81}Ga_{0.19}As$ layer grown at T=505°C, R=1.2 ML/s, and V/III flux ratio=4.

5.4.2 Dependence on Growth Temperature

In addition to material properties, growth conditions impact the appearance of pits in a mechanism similar to strain-induced islanding. A series of films were grown as a function of growth temperature in order to study its

effect on the critical thickness for pit formation and pit nucleation. Figure 5.10 is a series of AFM micrographs of $In_{0.81}Ga_{0.19}As$ films deposited at 475 °C ≤ T ≤ 505 °C. Table 5.3 compares the pits shown in Fig. 5.10 and demonstrates that growth temperature affects the surface coverage, size, and shape of the pits on the surface. At low temperature no pits are seen and the surface remains relatively smooth. By 495 °C over 11% of the surface is covered with pits. At 505 °C the pits cover almost 18% of the surface, due not only to an increase in the number of pits on the surface but also because the pits are larger at higher temperatures. These trends are to be expected given that mass transport is enhanced as temperature increases and mimic the effect of growth temperature on the critical thickness for island formation.

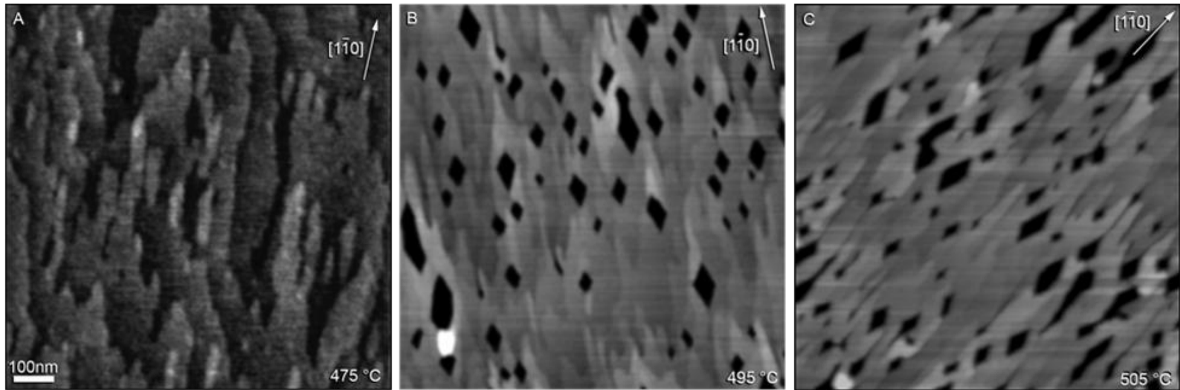

Figure 5.10: 1x1μm AFM images of $In_{0.81}Ga_{0.19}As$ films grown at h=60 ML, R=1.2 ML/s, and V/III flux ratio=4, for (a) T=475°C (b) T=495°C (c) T=505°C.

	475°C	**495°C**	**505°C**
Density	---	86.8±9.3um^{-1}	108±8.8um^{-1}
Coverage	0%	11.2±0.7%	17.7±2.2%
Length [$1\bar{1}0$]	---	84.4±6.2nm	115.1±7.3nm
Lateral Aspect Ratio	---	2.92±0.23	3.18±0.44
Vertical Aspect Ratio	---	0.18±0.01	0.14±0.01

Table 5.3: Comparison of pits on the surface of $In_{0.81}Ga_{0.19}As$ shown in Figure 5.9.

5.4.3 Dependence on Growth Rate

Growth rate also alters the onset of pitting in a manner similar to what is observed for islanding. Figure 5.11 shows two AFM images of $In_{0.81}Ga_{0.19}As$ films grown at R = 0.5 ML/sec and R = 1.25 ML/sec. Both images have

multiple pits on the surface with an occasional island although the pits and islands in Fig. 5.11(a) are larger than the 3D features in the film grown at a higher growth rate in Fig. 5.11(b). This is consistent with longer diffusion lengths of adatoms at slow deposition rates.[98] It should be noted that the depth of the pits in Fig. 5.10 and Fig. 5.11 terminates a few monolayers before the buffer resulting in a vertical aspect ratio less than 0.23, similar to the pits shown in Fig. 5.7(b) and Fig. 5.7(c). Line scans show the sides of the 3D island adjacent to two pits in Fig. 5.10(b) is bound by the {136} family of facets, similar to the line scan of the island shown in Fig. 5.8.

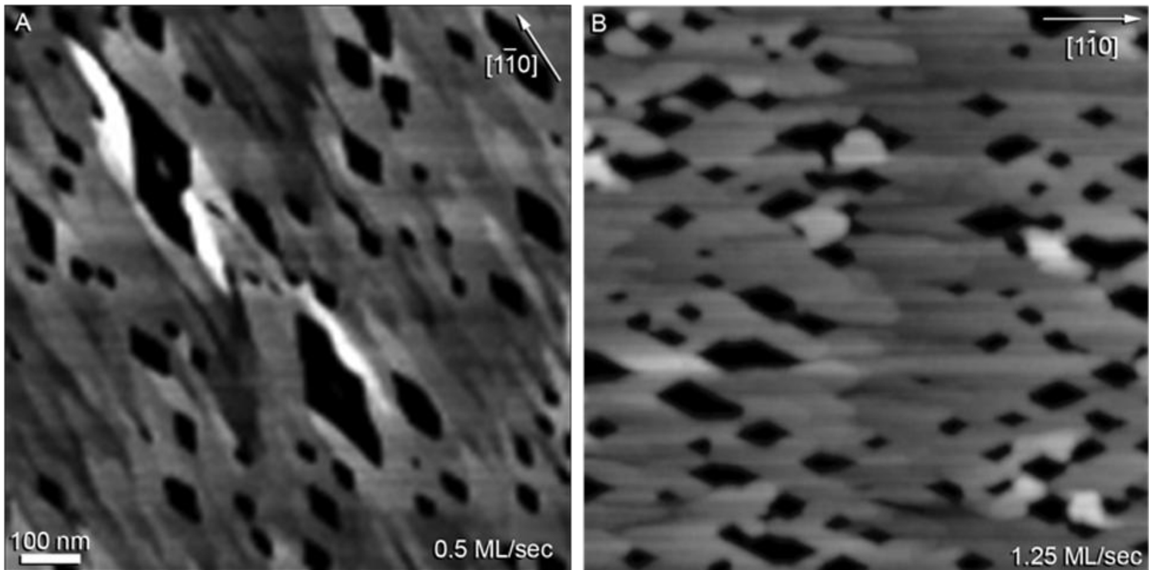

Figure 5.11: 1x1μm AFM images of $In_{0.81}Ga_{0.19}As$ films grown at T=505°C, h=55 ML, and V/III flux ratio=4, for (a) R=0.5 ML/sec and (b) R=1.25ML/sec.

	0.5ML/sec	1.25ML/sec
Density	104±6.9um^{-1}	97.2±8.1um^{-1}
Coverage	15.40±1.0%	17.70±0.5%
Length [$1\bar{1}0$]	163.1±8.4nm	131.2±5.3nm
Lateral Aspect Ratio	3.2±0.11	2.94±0.13
Vertical Aspect Ratio	0.10±0.02	0.12±0.01

Table 5.4: Comparison of pits on the surface of $In_{0.81}Ga_{0.19}As$ shown in Figure 5.10.

5.5 Discussion

In contrast to the islands shown in Fig. 5.3 on $In_{0.27}Ga_{0.73}As$, the pits present on the surface of $In_{0.81}Ga_{0.19}As$ elongate in the $[1\bar{1}0]$ with increasing thickness. This is most likely due to anisotropy in the diffusion of adatoms arising from the surface reconstructions on these surfaces.[99, 100] The vertical aspect ratio was observed to decrease with increasing thickness. At 40 ML (Fig. 5.7(a)) the nascent pits possess a sharp apex at their bottom, and the vertical aspect ratio is ~0.23, consistent with expectations for {136} facets pits.[101] As the pits continue to grow line scans reveal that although the interior walls maintain their {136} facets, the base of the pits truncate to the (001). As a result, the vertical aspect ratio decreases to ~0.19 at 45 ML and further decreases to ~0.12 at 50 ML. Figure 5.8 shows one of the pits in the 45

ML $In_{0.81}Ga_{0.19}As$ film terminating at 123 Å or ~40 ML. The depth of this pit is about 5 ML from the end of the $In_{0.81}Ga_{0.19}As$ film and the start of the buffer layer. In addition the (001) base of the pit can clearly be seen in this line scan. This in contrast to the smaller, more shallow pit that forms a sharp apex at its base and terminates halfway through the $In_{0.81}Ga_{0.19}As$ film. This suggests that the thickness of the $In_{0.81}Ga_{0.19}As$ film itself is a physical constraint to the depth of the pits. This may due to the fact that the buffer layer has a lower concentration of indium which increases the surface energy. Thus exposure of the buffer layer is energetically unfavorable.

This morphological evolution is distinctly different than what is observed in other pit-forming systems such as SiGe deposited at low temperatures and high growth rates.[89] In that system, pits and islands nucleate adjacent to one another. In these experiments using $In_{0.81}Ga_{0.19}As$, islands only occasionally form next to pits, as seen in Fig. 5.7(b). Because the growth temperature is relatively high and the growth rate is relatively low, the adatoms released from the pits as they grow have a large diffusion length and thus can migrate away from pits.

Analogous to island formation, pits develop in order to relieve lattice mismatch strain in the film. RHEED can be used to determine the in-plane lattice parameter of the films during growth by measuring the separation of the

diffraction rods and has been used to show that islanding relieves lattice mismatch strain.[66, 102] Figure 5.12 shows a plot of the in-plane lattice parameter measured during the deposition of an $In_{0.81}Ga_{0.19}As$ film grown at T=475 °C. AFM analysis of films grown at this temperature between $10<h<70$ ML shows that the onset of pit formation occurs at approximately 60 ML. The RHEED experiment shows that the in-plane lattice parameter of the $In_{0.81}Ga_{0.19}As$ film during growth remains near the lattice parameter of the InP substrate (5.8686 Å) for the majority of growth. The in-plane lattice parameter increases abruptly at 55 ML to a value of 5.94 ±0.01Å, close to the 5.9801 Å lattice parameter of a relaxed $In_{0.81}Ga_{0.19}As$ film, after which the growth was stopped. An AFM image taken of the film post growth is included in Fig. 5.12 and shows that pits did nucleate on the surface of this film. Together this data demonstrates that the appearance of pits is related to the relaxation of the in-plane lattice parameter, similar to the behavior of strain relaxation by islanding. [66, 102]

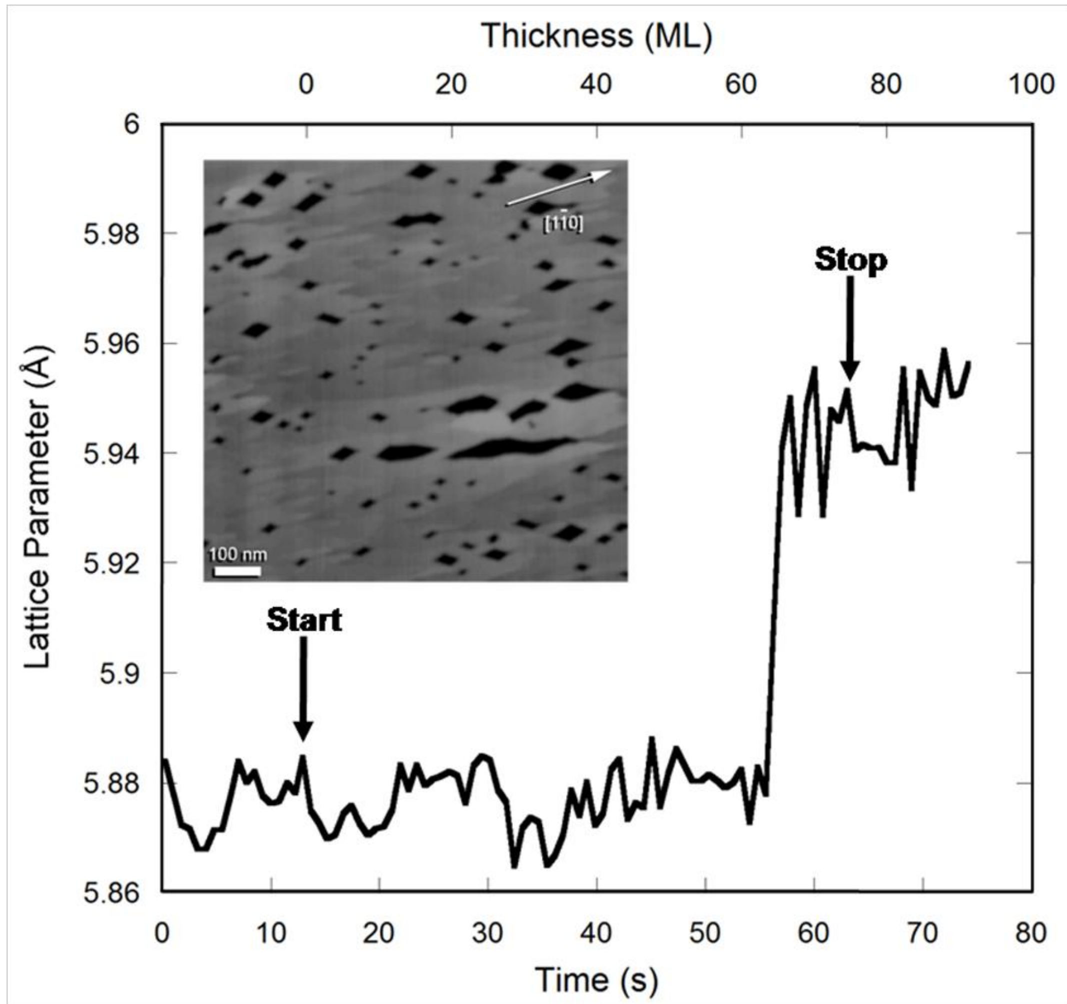

Figure 5.12: Plot of the lattice parameter obtained by measuring the separation of the RHEED diffraction rods during the deposition of an $In_{0.81}Ga_{0.19}As$ film grown at T=475 °C and R=1.2 ML/sec. Arrows denote the beginning and end of growth. Inset is a 1x1μm AFM image taken after growth showing pits on the surface of this sample.

Even though pit nucleation has rarely been reported for lattice mismatched films in the absence of islanding, models predict that for the

appropriate residual strain or surface energy pits will form prior to the nucleation of islands.[86] Bouville *et. al.* showed that the type of 3D features that appear on the growing surface depends on both the strain and surface energies of the film. For a given strain, islands form at high surface energy, pits at low surface energies, and a combination of islands and pits at intermediate values. While the precise values of the surface energy of InGaAs alloys is not known, it is reasonable to predict that the surface energy decreases with increasing In content based on the lower cohesive energy of InAs compared to GaAs.[103] Furthermore, it is known that In surface segregates in these systems,[51, 62] also compatible with the notion that In lowers the surface energy of the film. Rigorous calculation of the surface energy of these alloyed surfaces require detailed understanding of the atomic surface structure of these films, which can be quite complex. Nonetheless, all of these observations, including now the fact that higher In content films form pits prior to islands, are consistent with the decrease of surface energy as In content increases.

The presence of reconstructions on the surface can also impact the nucleation and growth of pits and islands on the surface. It is known that both (nx3) and β2(2x4) reconstructions coexist on the surface of $In_{0.81}Ga_{0.19}As$/InP films.[18] Figure 5.13 is a set of two filled state 500 x 500 Å STM images of a h = 50ML $In_{0.81}Ga_{0.19}As$/InP film in the vicinity of a pit (Fig. 5.13(a)) and away

from any pits (Fig. 5.13(b)). The atomic structure of this alloy surface consists of two distinct reconstructions: a disordered (nx3) surface with domains of β2(2x4).[18, 49]

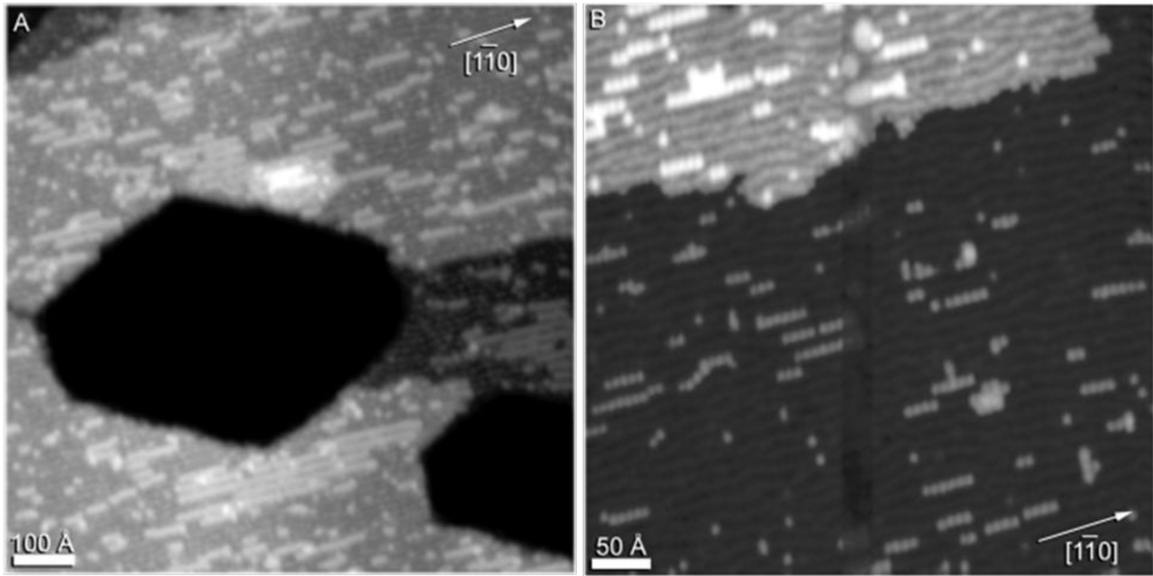

Figure 5.13: Filled state (-2.88 V, 100 pA) 500 x 500 Å STM images of a h=50ML $In_{0.81}Ga_{0.19}As$/InP film deposited at T=505°C, R=0.5 ML/s, F_{As4}=2.2 ML/s, and V/III flux ratio=4. Images were taken (a) near island/pit formations and (b) isolated from any 3D growth.

The distribution of the different reconstruction domains varies in the vicinity of the pits. Figure 5.13 shows that the area surrounding the pit is clustered with β2(2x4) reconstructions, while areas of the same sample further away from the pits have far fewer and smaller β2(2x4) domains, suggesting that their surface energy favors pit formation. Surface coverage data was averaged over six different regions near pits as well as fourteen different regions that are

at least 1000 Å from the nearest pit and showed that away from the pits, the coverage of the β2(2x4) is 15.7%, while close to the pits it is 29.6%. Recent β2(2x4) reconstruction models suggest that this reconstruction is indium enriched relative to the rest of the surface.[88] A nascent island can be seen forming on top of the β2(2x4) reconstruction, suggesting that this reconstruction may also act as a nucleation point for islands. Therefore, the type of reconstructions present on the growing surface of the films may affect the physical characteristics of the island and pit formations on the surface.

5.6 Conclusions

In summary, the nucleation of pits on the surface of $In_{0.81}Ga_{0.19}As$ during MBE growth was investigated. The conclusions of this chapter are as follows:

(1) An "inverse" SK growth mode was discovered where pitting is favored instead of islanding above the critical thickness. This is due to a higher surface energy of this film compared to the strain energy.

(2) The morphological evolution of pits is completely analogous to that of islands, in that the feature density increases proportionally with film thickness, and the critical thickness increases with decreasing growth temperature and increasing growth rate. These pits form on

the surface before islands, consistent with previous models but rarely seen experimentally.

(3) These results show that other pathways are available to achieve novel assemblies of nanostructures.

Chapter 6

Summary and Conclusions

Surfaces of $In_{0.81}Ga_{0.19}As/InP$ grown by molecular beam epitaxy and imaged by *in vacuo* scanning tunneling microscopy and atomic force microscopy were investigated in this work. The focus of this research entails the study of the coexistence of surface reconstruction domains on strained heteroepitaxial films, a thermodynamic model of the coexistence of (nx3) and β2(2x4) reconstructions, and pit nucleation during the growth of compressively strained $In_{0.81}Ga_{0.19}As/InP(001)$ layers. The ultimate goal of the research is to develop a quantitative understanding of the connection between surface reconstructions on $In_{0.81}Ga_{0.19}As/InP$ and film thickness, growth conditions, surface energy, and morphological evolution.

The surface of $In_{0.81}Ga_{0.19}As$ films was observed to consist of small anisotropic regions of a β2(2x4) reconstruction in a matrix of a disordered (nx3) reconstruction. It was shown that the presence of β2(2x4) is stable across a range of growth conditions and material properties including growth temperature and total film thickness. Surface coverage data shows that growth temperature may affect the nucleation and growth of the β2(2x4)

reconstruction. This indicates that indium segregation length may play a role in domain stability and the resulting surface coverage of β2(2x4). Surface coverage data also shows that the total film thickness may also play a role in the stability of β2(2x4) domains. AFM images and surface roughness analysis shows that there is a transition from vicinal to mounded growth at thicknesses coinciding with a decrease in the β2(2x4) coverage. This suggests that the β2(2x4) domains are strain stabilized and their surface coverage depends on the residual strain in the film.

A thermodynamic model shows that elastic relaxation at the boundaries stabilize the mixed domains by lowering the total free energy. This work shows that this model may be applied to the size distribution of reconstructions in heteroepitxial films, and demonstrates the importance of the boundary anisotropy on the formations of nanostructures in the plane of the terrace. For large unit strain energy, this coexistence is globally stable with an equilibrium domain shape that is infinitesimally narrow and infinitely long. Experimental data is consistent with this picture, showing that the shape of the domains becomes more anisotropic with increasing domain size and growth temperature.

Finally, the nucleation of pits on the surface of $In_{0.81}Ga_{0.19}As$ during growth was investigated and an “inverse” SK growth mode was discovered where pitting is favored instead of islanding above the critical thickness. This

is due to a higher surface energy of this film compared to the strain energy. The morphological evolution of pits is completely analogous to that of islands, in that the feature density increases proportionally with film thickness, and the critical thickness increases with decreasing growth temperature and increasing growth rate. These pits form on the surface before islands, consistent with previous models but rarely seen experimentally. These results show that other pathways are available to achieve novel assemblies of nanostructures.

Appendix A

Mathematica code for a thermodynamic model that outputs a contour plot of the total free energy as a function of the domain width and length.

(*A set of materials parameters*)

(* materials constants *)

g=1. (* surface energy *);

bs= 1. (* boundary energy along s *);

bt=1. (* boundary energy along t *);

F=30. (*elastic force*);

a=.4(* cutoff *);

v=0.3 (* poisson ratio *);

(* elastic energy component *)

elastic[s_,t_]:=F (-2 (1-v) s Log[s/E a]-2 (1-v) t Log[t/E a]+2 (s+t)-4 (1-v) $\sqrt{s^2+t^2}$ +t (1-v) Log[($\sqrt{s^2+t^2}$ +t)/($\sqrt{s^2+t^2}$ -t)]+s (1-v) Log[($\sqrt{s^2+t^2}$ +s)/($\sqrt{s^2+t^2}$ -s)]);

(* surface energy component *)

surface[s_,t_]:= g s t ;

(* boundary energy component *)

boundary[s_, t_]:= 2 s bs + 2 t bt;

```
(* total free energy, neglecting energy contribution of the corners *)

energy[s_, t_]:= elastic[s,t]+surface[s,t]+boundary[s,t]


(* below is the procedure to find the position in s of the energy minimum for a
given value of area .  An initial guess for the minimum is required *)


(*First guess*)

areamin=10.; (*min value of t *)

areamax=4000.; (* max value of t *)

darea=100. ; (*increment in t*)

guess=.1; (* initial guess for the local minimum in s *)


(* this finds the minima in the energy for a given area and returns an array of
the energy and the root (minimum) *)


sol=Table[FindMinimum[energy[s,area/s],{s,guess}, Method→
Newton],{area,areamin,areamax,darea }];

arealist=Table[area,{area,areamin,areamax,darea }];


(*this converts the root to a usable number.  Resulting list is of the minimum
energy, value of s at that energy, and the area*)

solPoints=Table[{sol[[t,1]],s/.sol[[t,2]]},{t,1,Length[sol]}];
```

```
(*this is a list of the min energy, the value of s at that energy, and the area for the small guess*)

solPointsall1=Table[{solPoints[[t,1]],solPoints[[t,2]],arealist[[t]]},{t,1,Length[sol]}];


(*Second guess*)

areamin=10.; (*min value of t *)

areamax=4000.; (* max value of t *)

darea=100. ; (*increment in t*)

guess=2000.; (* initial guess for the local minimum in s *)


(* this finds the minima in the energy for a given area and returns an array of the energy and the root (minimum) *)


sol=Table[FindMinimum[energy[s,area/s],{s,guess}, Method→Newton],{area,areamin,areamax,darea }];

arealist=Table[area,{area,areamin,areamax,darea }];


(*this converts the root to a usable number.  Resulting list is of the minimum energy, value of s at that energy, and the area*)

solPoints=Table[{sol[[t,1]],s/.sol[[t,2]]},{t,1,Length[sol]}];


(*this is a list of the min energy, the value of s at that energy, and the area for the high guess*)

solPointsall2=Table[{solPoints[[t,1]],solPoints[[t,2]],arealist[[t]]},{t,1,Length[sol]}];
```

```
(*solPointsall=Table[{If[solPointsall1[[t,1]]<solPointsall2[[t,1]],solPointsall1[[
t,1]],solPointsall2[[t,1]]],If[solPointsall1[[t,1]]<solPointsall2[[t,1]],solPointsall
1[[t,2]],solPointsall2[[t,2]]],arealist[[t]]},{t,1,Length[sol]}];*)


arearec1251=Table[{solPointsall1[[t,3]],solPointsall1[[t,2]]},{t,1,Length[sol]}]
;

arearec2251=Table[{solPointsall1[[t,3]],(solPointsall1[[t,3]]/solPointsall1[[t,2]]
)},{t,1,Length[sol]}];

areasq25=Table[{s s,s},{s,1,Length[sol]}];


arearec1252=Table[{solPointsall2[[t,3]],solPointsall2[[t,2]]},{t,1,Length[sol]}]
;

arearec2252=Table[{solPointsall2[[t,3]],(solPointsall2[[t,3]]/solPointsall2[[t,2]]
)},{t,1,Length[sol]}];


alogarearec1F1001=Table[{Log[arearec1251[[t,1]]],Log[arearec1251[[t,2]]]},
{t,1,Length[sol]}];

alogarearec2F1001=Table[{Log[arearec2251[[t,1]]],Log[arearec2251[[t,2]]]},
{t,1,Length[sol]}];

logarearec1F1002=Table[{Log[arearec1252[[t,1]]],Log[arearec1252[[t,2]]]},
{t,1,Length[sol]}];

logarearec2F1002=Table[{Log[arearec2252[[t,1]]],Log[arearec2252[[t,2]]]},
{t,1,Length[sol]}];


MultipleListPlot[alogarearec1F1001, alogarearec2F1001]
```

contour=ContourPlot[energy[s,t], {s, 0.01,400}, {t, 0.01,400}]

(*another set of materials parameters*)

(* materials constants *)

g=1. (* surface energy *);

bs= 1. (* boundary energy along s *);

bt=10. (* boundary energy along t *);

F=30. (*elastic force*);

a=.4(* cutoff *);

v=0.3 (* poisson ratio *);

(* elastic energy component *)

elastic[s_,t_]:=F (-2 (1-v) s Log[s/E a]-2 (1-v) t Log[t/E a]+2 (s+t)-4 (1-v) $\sqrt{s^2+t^2}$ +t (1-v) Log[($\sqrt{s^2+t^2}$ +t)/($\sqrt{s^2+t^2}$ -t)]+s (1-v) Log[($\sqrt{s^2+t^2}$ +s)/($\sqrt{s^2+t^2}$ -s)]);

(* surface energy component *)

surface[s_,t_]:= g s t ;

(* boundary energy component *)

boundary[s_, t_]:= 2 s bs + 2 t bt;

(* total free energy, neglecting energy contribution of the corners *)

energy[s_, t_]:= elastic[s,t]+surface[s,t]+boundary[s,t]

(* below is the procedure to find the position in s of the energy minimum for a given value of area . An initial guess for the minimum is required *)

(*First guess*)

areamin=10.; (*min value of t *)

areamax=4000.; (* max value of t *)

darea=100. ; (*increment in t*)

guess=.1; (* initial guess for the local minimum in s *)

(* this finds the minima in the energy for a given area and returns an array of the energy and the root (minimum) *)

sol=Table[FindMinimum[energy[s,area/s],{s,guess}, Method→Newton],{area,areamin,areamax,darea }];

arealist=Table[area,{area,areamin,areamax,darea }];

(*this converts the root to a usable number. Resulting list is of the minimum energy, value of s at that energy, and the area*)

solPoints=Table[{sol[[t,1]],s/.sol[[t,2]]},{t,1,Length[sol]}];

(*this is a list of the min energy, the value of s at that energy, and the area for the small guess*)

solPointsall1=Table[{solPoints[[t,1]],solPoints[[t,2]],arealist[[t]]},{t,1,Length[sol]}];

```
(*Second guess*)

areamin=10.; (*min value of t *)

areamax=4000.; (* max value of t *)

darea=100. ; (*increment in t*)

guess=2000.; (* initial guess for the local minimum in s *)


(* this finds the minima in the energy for a given area and returns an array of
the energy and the root (minimum) *)


sol=Table[FindMinimum[energy[s,area/s],{s,guess},
Method→Newton],{area,areamin,areamax,darea }];

arealist=Table[area,{area,areamin,areamax,darea }];


(*this converts the root to a usable number.  Resulting list is of the minimum
energy, value of s at that energy, and the area*)

solPoints=Table[{sol[[t,1]],s/.sol[[t,2]]},{t,1,Length[sol]}];


(*this is a list of the min energy, the value of s at that energy, and the area for
the high guess*)

solPointsall2=Table[{solPoints[[t,1]],solPoints[[t,2]],arealist[[t]]},{t,1,Length[s
ol]}];
```

```
(*solPointsall=Table[{If[solPointsall1[[t,1]]<solPointsall2[[t,1]],solPointsall1[[
t,1]],solPointsall2[[t,1]]],If[solPointsall1[[t,1]]<solPointsall2[[t,1]],solPointsall
1[[t,2]],solPointsall2[[t,2]]],arealist[[t]]},{t,1,Length[sol]}];*)


arearec1251=Table[{solPointsall1[[t,3]],solPointsall1[[t,2]]},{t,1,Length[sol]}]
;

arearec2251=Table[{solPointsall1[[t,3]],(solPointsall1[[t,3]]/solPointsall1[[t,2]]
)},{t,1,Length[sol]}];

areasq25=Table[{s s,s},{s,1,Length[sol]}];


arearec1252=Table[{solPointsall2[[t,3]],solPointsall2[[t,2]]},{t,1,Length[sol]}]
;

arearec2252=Table[{solPointsall2[[t,3]],(solPointsall2[[t,3]]/solPointsall2[[t,2]]
)},{t,1,Length[sol]}];


blogarearec1F1001=Table[{Log[arearec1251[[t,1]]],Log[arearec1251[[t,2]]]},
{t,1,Length[sol]}];

blogarearec2F1001=Table[{Log[arearec2251[[t,1]]],Log[arearec2251[[t,2]]]},
{t,1,Length[sol]}];

logarearec1F1002=Table[{Log[arearec1252[[t,1]]],Log[arearec1252[[t,2]]]},
{t,1,Length[sol]}];

logarearec2F1002=Table[{Log[arearec2252[[t,1]]],Log[arearec2252[[t,2]]]},
{t,1,Length[sol]}];


MultipleListPlot[blogarearec1F1001, blogarearec2F1001]
```

contour=ContourPlot[energy[s,t], {s, 0.01,400}, {t, 0.01,400}]

(*another set of materials parameters*)

(* materials constants *)

g=1. (* surface energy *);

bs= 1. (* boundary energy along s *);

bt=45. (* boundary energy along t *);

F=30. (*elastic force*);

a=.4(* cutoff *);

v=0.3 (* poisson ratio *);

(* elastic energy component *)

elastic[s_,t_]:=F (-2 (1-v) s Log[s/E a]-2 (1-v) t Log[t/E a]+2 (s+t)-4 (1-v) $\sqrt{s^2+t^2}$ +t (1-v) Log[($\sqrt{s^2+t^2}$ +t)/($\sqrt{s^2+t^2}$ -t)]+s (1-v) Log[($\sqrt{s^2+t^2}$ +s)/($\sqrt{s^2+t^2}$ -s)]);

(* surface energy component *)

surface[s_,t_]:= g s t ;

(* boundary energy component *)

boundary[s_, t_]:= 2 s bs + 2 t bt;

(* total free energy, neglecting energy contribution of the corners *)

energy[s_, t_]:= elastic[s,t]+surface[s,t]+boundary[s,t]

(* below is the procedure to find the position in s of the energy minimum for a given value of area . An initial guess for the minimum is required *)

```
(*First guess*)

areamin=10.; (*min value of t *)

areamax=4000.; (* max value of t *)

darea=100. ; (*increment in t*)

guess=.1; (* initial guess for the local minimum in s *)
```

(* this finds the minima in the energy for a given area and returns an array of the energy and the root (minimum) *)

```
sol=Table[FindMinimum[energy[s,area/s],{s,guess},
Method→Newton],{area,areamin,areamax,darea }];

arealist=Table[area,{area,areamin,areamax,darea }];
```

(*this converts the root to a usable number. Resulting list is of the minimum energy, value of s at that energy, and the area*)

```
solPoints=Table[{sol[[t,1]],s/.sol[[t,2]]},{t,1,Length[sol]}];
```

(*this is a list of the min energy, the value of s at that energy, and the area for the small guess*)

```
solPointsall1=Table[{solPoints[[t,1]],solPoints[[t,2]],arealist[[t]]},{t,1,Length[sol]}];


(*Second guess*)

areamin=10.; (*min value of t *)

areamax=4000.; (* max value of t *)

darea=100. ; (*increment in t*)

guess=2000.; (* initial guess for the local minimum in s *)


(* this finds the minima in the energy for a given area and returns an array of the energy and the root (minimum) *)


sol=Table[FindMinimum[energy[s,area/s],{s,guess}, Method→Newton],{area,areamin,areamax,darea }];

arealist=Table[area,{area,areamin,areamax,darea }];


(*this converts the root to a usable number.  Resulting list is of the minimum energy, value of s at that energy, and the area*)

solPoints=Table[{sol[[t,1]],s/.sol[[t,2]]},{t,1,Length[sol]}];


(*this is a list of the min energy, the value of s at that energy, and the area for the high guess*)

solPointsall2=Table[{solPoints[[t,1]],solPoints[[t,2]],arealist[[t]]},{t,1,Length[sol]}];
```

```
(*solPointsall=Table[{If[solPointsall1[[t,1]]<solPointsall2[[t,1]],solPointsall1[[
t,1]],solPointsall2[[t,1]]],If[solPointsall1[[t,1]]<solPointsall2[[t,1]],solPointsall
1[[t,2]],solPointsall2[[t,2]]],arealist[[t]]},{t,1,Length[sol]}];*)

arearec1251=Table[{solPointsall1[[t,3]],solPointsall1[[t,2]]},{t,1,Length[sol]}]
;

arearec2251=Table[{solPointsall1[[t,3]],(solPointsall1[[t,3]]/solPointsall1[[t,2]]
)},{t,1,Length[sol]}];

areasq25=Table[{s s,s},{s,1,Length[sol]}];

arearec1252=Table[{solPointsall2[[t,3]],solPointsall2[[t,2]]},{t,1,Length[sol]}]
;

arearec2252=Table[{solPointsall2[[t,3]],(solPointsall2[[t,3]]/solPointsall2[[t,2]]
)},{t,1,Length[sol]}];

clogarearec1F1001=Table[{Log[arearec1251[[t,1]]],Log[arearec1251[[t,2]]]},
{t,1,Length[sol]}];

clogarearec2F1001=Table[{Log[arearec2251[[t,1]]],Log[arearec2251[[t,2]]]},
{t,1,Length[sol]}];

logarearec1F1002=Table[{Log[arearec1252[[t,1]]],Log[arearec1252[[t,2]]]},
{t,1,Length[sol]}];

logarearec2F1002=Table[{Log[arearec2252[[t,1]]],Log[arearec2252[[t,2]]]},
{t,1,Length[sol]}];
```

```
MultipleListPlot[clogarearec1F1001, clogarearec2F1001]

contour=ContourPlot[energy[s,t], {s, 0.01,400}, {t, 0.01,400}]

MultipleListPlot[alogarearec1F1001, alogarearec2F1001, blogarearec1F1001,
blogarearec2F1001,clogarearec1F1001, clogarearec2F1001]
```

Appendix B

Mathematica code for a thermodynamic model that outputs a contour plot of the total free energy as a function of

```
<<"BarCharts`";<<"Histograms`";<<"PieCharts`"; <<"ErrorBarPlots`"

(g=1.`;) (bs=1.`;) (bt=1.`;) (F=27.`;) (a=0.4`;) (v=0.3`;)

(elastic[s_,t_]:=F (-2 (1-v) s Log[(s a)/\[ExponentialE]]-2 (1-v) t Log[(t
a)/\[ExponentialE]]+2 (s+t)-4 (1-v) Sqrt[s^2+t^2]+t (1-v)
Log[(Sqrt[s^2+t^2]+t)/(Sqrt[s^2+t^2]-t)]+s (1-v)
Log[(Sqrt[s^2+t^2]+s)/(Sqrt[s^2+t^2]-s)]);)

 (surface[s_,t_]:=g s t;)

(boundary[s_,t_]:=2 s bs+2 t bt;)

(energy[s_,t_]:=elastic[s,t]+surface[s,t]+boundary[s,t])

(areamin=10.`;areamax=4000.`;darea=100.`;guess=100.`;sol=Table[FindMinim
um[energy[s,area/s],{s,guess},Method->Newton], {area,areamin, areamax,
darea}];)  (arealist=Table[area,{area,areamin,areamax,darea}];)
(solPoints=Table[{sol[[t,1]],s/.sol[[t,2]]},{t,1,Length[sol]}];)
(solPointsall1=Table[{solPoints[[t,1]],solPoints[[t,2]],arealist[[t]]},{t,1,Length[
```

```
sol]}];)
(minenpoints1=Table[{solPointsall1[[t,2]],solPointsall1[[t,1]]},{t,1,Length[sol]
}];)
(minenpoints1n=Table[{solPointsall1[[t,3]]/solPointsall1[[t,2]],solPointsall1[[t,
1]]},{t,1,Length[sol]}];)
(arearec125=Table[{solPointsall[[t,3]],solPointsall[[t,2]]},{t,1,Length[sol]}];)
(arearec225=Table[{solPointsall[[t,3]],solPointsall[[t,3]]/solPointsall[[t,2]]},{t,
1,Length[sol]}];) (areasq25=Table[{s s,s},{s,1,Length[sol]}];)
(logarearec1=Table[{Log[arearec125[[t,1]]],Log[arearec125[[t,2]]]},{t,1,Lengt
h[sol]}];)
(logarearec2=Table[{Log[arearec225[[t,1]]],Log[arearec225[[t,2]]]},{t,1,Lengt
h[sol]}];)
(logareasq=Table[{Log[areasq25[[t,1]]],Log[areasq25[[t,2]]]},{t,1,Length[sol]
}];)


 ListPlot[{logarearec1,logarearec2}] ListPlot[{arearec125,arearec225}]
(contour=ContourPlot[energy[s,t],{s,0.01`,400},{t,0.01`,400}])


Plot[{energy[s,s]},{s,1,400}]


compare=Plot[{energy[s,400/s],energy[s,1000/s], energy[s,3000/s],
energy[6000/s,s], energy[10000/s,s]},{s,10,400},PlotStyle-
>{{Hue[0.0]},{Hue[0.1]}, {Hue[.4]}, {Hue[.6]}, {Hue[.8]}}, PlotRange->{-
7000,2000}]


areapoints=List[{√400. ,energy[√400. ,√400. ]}, {√1000. ,energy[√1000. ,
√1000. ]},{√3000. ,energy[√3000. ,√3000. ]},{√6000. ,energy[√6000. ,
√6000. ]},{√10000. ,energy[√10000. ,√10000. ]},{√20000. ,energy[√20000.
,√20000. ]},
   {√30000. ,energy[√30000. ,√30000. ]}   ];
```

```
areapoints2plot=ListPlot[areapoints]


DisplayTogether[Plot[{ energy[s,400/s],energy[s,1000/s],
energy[s,3000/s],energy[6000/s,s], energy[10000/s,s],energy[20000/s,s],
energy[30000/s,s]},{s,1,1000},PlotStyle->{{Hue[0.0]},{Hue[0.1]}, {Hue[.4]},
{Hue[.6]}, {Hue[.8]}}], ListPlot[areapoints,PlotStyle->PointSize[.01]]]


Plot[{energy[s,s]},{s,1,1000}]

axs= Table[{s},{s,1,1000}];

rec400=Table[{energy[s,400/s]},{s,1,1000}];

rec1000=Table[{energy[s,1000/s]},{s,1,1000}];

rec3000=Table[{energy[s,3000/s]},{s,1,1000}];

rec6000=Table[{energy[s,6000/s]},{s,1,1000}];

rec10000=Table[{energy[s,10000/s]},{s,1,1000}];

rec20000=Table[{energy[s,20000/s]},{s,1,1000}];

rec30000=Table[{energy[s,30000/s]},{s,1,1000}];

Export["energyvarealF27.xls",{axs, rec400, rec1000,
rec3000,rec6000,rec10000, rec20000, rec30000, areapoints}]
```

References

1. De Laurentis, M., A. Irace, and G. Breglio, *Electrically induced Bragg Reflectors in InP/InGaAsP waveguides as ultrafast optoelectronic modulators.* Journal of the European Optical Society-Rapid Publications, 2008. **3**: p. 4.
2. Joyce, H.J., et al. *Growth, Structural and Optical Properties of III-V Nanowires for Optoelectronic Applications*. in *7th IEEE Conference on Nanotechnology*. 2007. Hong Kong, PEOPLES R CHINA: Ieee.
3. May-Arrioja, D.A., et al. *Intermixing of InP-based multiple quantum wells for integrated optoelectronic devices*. in *Workshop on Recent Advances on Low Dimensional Structures and Devices*. 2008. Nottingham, ENGLAND: Elsevier Sci Ltd.
4. Singh, A.K., et al., *Effects of morphology and doping on the electronic and structural properties of hydrogenated silicon nanowires.* Nano Letters, 2006. **6**(5): p. 920-925.
5. Xue, Q.K., T. Hashizume, and T. Sakurai, *Scanning tunneling microscopy of III-V compound semiconductor (001) surfaces.* Progress in Surface Science, 1997. **56**(1-2): p. 1-131.
6. Ohtake, A., *Surface reconstructions on GaAs(001).* Surface Science Reports, 2008. **63**(7): p. 295-327.
7. Yang, K. and L.J. Schowalter, *SURFACE RECONSTRUCTION PHASE-DIAGRAM AND GROWTH ON GAAS(111)B SUBSTRATES BY MOLECULAR-BEAM EPITAXY.* Applied Physics Letters, 1992. **60**(15): p. 1851-1853.
8. Ratsch, C., et al., *Surface reconstructions for InAs(001) studied with density-functional theory and STM.* Physical Review B, 2000. **62**(12): p. R7719-R7722.
9. Tang, Z., et al., *Bi- and Au-induced reconstructions on GaAs(001)-2x4 surface.* Chinese Physics Letters, 2008. **25**(8): p. 2977-2980.
10. Saranin, A.A., et al., *Analysis of surface structures through determination of their composition using STM: Si(100)4x3-In and Si(111)4x1-In reconstructions.* Physical Review B, 1999. **60**(20): p. 14372-14381.
11. Lafemina, J.P., *TOTAL-ENERGY CALCULATIONS OF SEMICONDUCTOR SURFACE RECONSTRUCTIONS.* Surface Science Reports, 1992. **16**(4-5): p. 133-260.
12. Gomyo, A., et al., *OBSERVATION OF A NEW ORDERED PHASE IN ALXIN1-XAS ALLOY AND RELATION BETWEEN ORDERING STRUCTURE AND SURFACE RECONSTRUCTION DURING*

MOLECULAR-BEAM-EPITAXIAL GROWTH. Physical Review Letters, 1994. **72**(5): p. 673-676.
13. Jo, Y.C., et al. *Optical properties of 1 by 16 highly sensitive InP/InGaAs heterojunction phototransistor arrays*. in *IEEE Sensors 2004 Conference*. 2004. Vienna, AUSTRIA: Ieee.
14. Cullis, A.G., A.J. Pidduck, and M.T. Emeny, *Growth morphology evolution and dislocation introduction in the InGaAs/GaAs heteroepitaxial system.* Journal of Crystal Growth, 1996. **158**(1-2): p. 15-27.
15. Yastrubchak, O., et al. *Misfit-dislocation induced surface morphology of InGaAs/GaAs heterostructures*. in *8th Workshop of the European-Microbeam-Analysis-Society*. 2003. Chiclana de la Frontera, SPAIN: Springer-Verlag Wien.
16. Sauvagesimkin, M., et al., *COMMENSURATE AND INCOMMENSURATE PHASES AT RECONSTRUCTED (IN,GA)AS(001) SURFACES - X-RAY-DIFFRACTION EVIDENCE FOR A COMPOSITION LOCK-IN.* Physical Review Letters, 1995. **75**(19): p. 3485-3488.
17. SauvageSimkin, M., et al., *Reconstruction and chemical ordering at the surface of strained (In, Ga) As epilayers.* Applied Surface Science, 1996. **104**: p. 646-651.
18. Millunchick, J.M., et al., *Surface reconstructions of InGaAs alloys.* Surface Science, 2004. **550**(1-3): p. 1-7.
19. Tromp, R.M. and J.B. Hannon, *Thermodynamics of nucleation and growth.* Surface Review and Letters, 2002. **9**(3-4): p. 1565-1593.
20. Sears, L.E., J.M. Millunchick, and C. Pearson, *The coexistence of surface reconstruction domains on strained heteroepitaxial films.* Journal of Vacuum Science & Technology B, 2008. **26**(6): p. 1948-1951.
21. Nosho, B.Z., et al., *Effects of surface reconstruction on III-V semiconductor interface formation: The role of III/V composition.* Applied Physics Letters, 1999. **74**(12): p. 1704-1706.
22. Farrell, H.H., J.P. Harbison, and L.D. Peterson, *MOLECULAR-BEAM EPITAXY GROWTH MECHANISMS ON GAAS(100) SURFACES.* Journal of Vacuum Science & Technology B, 1987. **5**(5): p. 1482-1489.
23. Ward, R.C.C., E.J. Grier, and A.K. Petford-Long. *MBE growth of (110) refractory metals on a-plane sapphire*. in *Annual Conference on British-Association-for-Crystal-Growth (BACG)*. 2002. Liverpool, England: Kluwer Academic Publ.
24. Onojima, N., J. Suda, and H. Matsunami. *Heteroepitaxial growth of insulating AlN on 6H-SiC by MBE*. in *International Conference on*

Silicon Carbide and Related Materials. 2001. Tsukuba, Japan: Trans Tech Publications Ltd.
25. Dehne, A., *Scanning Tunneling Microscopy Tip Project* 2006, University of Michigan: Ann Arbor. p. 6.
26. Bracker, A.S., et al., *Surface reconstruction phase diagrams for InAs, AlSb, and GaSb.* Journal of Crystal Growth, 2000. **220**(4): p. 384-392.
27. Zhang, S.B. and A. Zunger, *Method of linear combination of structural motifs for surface and step energy calculations: Application to GaAs(001).* Physical Review B, 1996. **53**(3): p. 1343-1356.
28. Chizhov, I., G. Lee, and R.F. Willis, ***GaAs(001) ''233'' surface studied by scanning tunneling microscopy***. Physical Review B, 1997. **56**(3).
29. Riposan, A., J.M. Millunchick, and C. Pearson, *Strain mediated reconstructions and indium segregation on InGaAs/GaAs(001) alloy-surfaces at intermediate lattice mismatch.* Journal of Vacuum Science & Technology A, 2006. **24**(6): p. 2041-2048.
30. Xue, Q.K., et al., *Indium-rich 4x2 reconstruction in novel growth of InAs on the GaAs(001).* Science Reports of the Research Institutes Tohoku University Series a-Physics Chemistry and Metallurgy, 1997. **44**(2): p. 153-156.
31. Yamaguchi, H. and Y. Horikoshi, *UNIFIED MODEL FOR STRUCTURE TRANSITION AND ELECTRICAL-PROPERTIES OF INAS (001) SURFACES STUDIED BY SCANNING-TUNNELING-MICROSCOPY.* Japanese Journal of Applied Physics Part 2-Letters, 1994. **33**(10A): p. L1423-L1426.
32. Laukkanen, P., et al., *Electronic and structural properties of GaAs(100)(2x4) and InAs(100)(2x4) surfaces studied by core-level photoemission and scanning tunneling microscopy.* Physical Review B, 2005. **72**(4).
33. Chakrabarti, A., P. Kratzer, and M. Scheffler, *Surface reconstructions and atomic ordering in InxGa1-xAs(001) films: A density-functional theory study.* Physical Review B, 2006. **74**(24).
34. Heller, E.J. and M.G. Lagally, *INSITU SCANNING TUNNELING MICROSCOPY OBSERVATION OF SURFACE-MORPHOLOGY OF GAAS(001) GROWN BY MOLECULAR-BEAM EPITAXY.* Applied Physics Letters, 1992. **60**(21): p. 2675-2677.
35. Garreau, Y., et al., *Atomic structure and faulted boundaries in the GaAs(001) beta(2x4) surface as derived from x-ray diffraction and line-shape analysis.* Physical Review B, 1996. **54**(24): p. 17638-17646.
36. Ichimiya, A., Y. Nishikawa, and M. Uchiyama. *Surface structures of the GaAs(001)2 x 4 studied by RHEED rocking curves*. in *International*

Symposium on Surface and Interface: Properties of Different Symmetry Crossing 2000. 2000. Nagoya, Japan: Elsevier Science Bv.
37. Ohtake, A., et al., *Real-time analysis of adsorption processes of Zn on the GaAs(001)-(2 x 4) surface.* Physical Review B, 1999. **60**(12): p. 8713-8718.
38. Northrup, J.E. and S. Froyen, *STRUCTURE OF GAAS(001) SURFACES - THE ROLE OF ELECTROSTATIC INTERACTIONS.* Physical Review B, 1994. **50**(3): p. 2015-2018.
39. McCoy, J.M., U. Korte, and P.A. Maksym, *Determination of the atomic geometry of the GaAs(001)2x4 surface by dynamical RHEED intensity analysis: the beta 2(2x4) model.* Surface Science, 1998. **418**(1): p. 273-280.
40. Schmidt, W.G. and F. Bechstedt, *Geometry and electronic structure of GaAs(001)(2x4) reconstructions.* Physical Review B, 1996. **54**(23): p. 16742-16748.
41. Schmidt, W.G. and F. Bechstedt, *Atomic structures of GaAs(100)-(2x4) reconstructions.* Surface Science, 1996. **360**(1-3): p. L473-L477.
42. Srivastava, G.P. and S.J. Jenkins, *Atomic geometry and bonding on the GaAs(001)-beta 2(2x4) surface from ab initio pseudopotential calculations.* Physical Review B, 1996. **53**(19): p. 12589-12592.
43. Takahasi, M., et al., *Domain boundaries in the GaAs(001)-2x4 surface.* Physical Review B, 2003. **68**(8): p. 5.
44. Riposan, A., *Surface Reconstructions and Morphology of InGaAs Compound Semiconductor Alloys*, in *Materials Science and Engineering*. 2004, University of Michigan: Ann Arbor. p. 255.
45. Penev, E., et al., *Anisotropic diffusion of In adatoms on pseudomorphic InxGa1-xAs films: First-principles total energy calculations.* Physical Review B, 2004. **69**(11): p. 10.
46. Belk, J.G., et al., *Surface alloying at InAs-GaAs interfaces grown on (001) surfaces by molecular beam epitaxy.* Surface Science, 1997. **387**(1-3): p. 213-226.
47. Pashley, M.D., *ELECTRON COUNTING MODEL AND ITS APPLICATION TO ISLAND STRUCTURES ON MOLECULAR-BEAM EPITAXY GROWN GAAS(001) AND ZNSE(001).* Physical Review B, 1989. **40**(15): p. 10481-10487.
48. Barvosa-Carter, W., et al., *Structure of III-Sb(001) growth surfaces: The role of heterodimers.* Physical Review Letters, 2000. **84**(20): p. 4649-4652.
49. Bone, P.A., et al., *Surface reconstructions of InGaAs alloys.* Surface Science, 2006. **600**(5): p. 973-982.

50. Chattopadhyay, K., et al., *Electroreflectance study of effects of indium segregation in molecular-beam-epitaxy-grown InGaAs/GaAs.* Journal of Applied Physics, 1997. **81**(8): p. 3601-3606.
51. Moran, M., et al., *Indium segregation in (111)B GaAs-InxGa1-xAs quantum wells determined by transmission electron microscopy.* Journal of Physics D-Applied Physics, 2001. **34**(13): p. 1943-1946.
52. Gerard, J.M. and C. Danterroches. *GROWTH OF INGAAS/GAAS HETEROSTRUCTURES WITH ABRUPT INTERFACES ON THE MONOLAYER SCALE*. in *8th International Conference on Molecular Beam Epitaxy*. 1994. Toyonaka, Japan: Elsevier Science Bv.
53. Evans, K.R., et al., *SURFACE-CHEMISTRY EVOLUTION DURING MOLECULAR-BEAM EPITAXY GROWTH OF INGAAS.* Journal of Vacuum Science & Technology B, 1995. **13**(4): p. 1820-1823.
54. Moison, J.M., et al., *SURFACE SEGREGATION OF 3RD-COLUMN IN GROUP III-V ARSENIDE COMPOUNDS - TERNARY ALLOYS AND HETEROSTRUCTURES.* Physical Review B, 1989. **40**(9): p. 6149-6162.
55. Ni, W.X., et al., *KINETICS OF DOPANT INCORPORATION USING A LOW-ENERGY ANTIMONY ION-BEAM DURING GROWTH OF SI(100) FILMS BY MOLECULAR-BEAM EPITAXY.* Physical Review B, 1989. **40**(15): p. 10449-10459.
56. Mozume, T. and I. Ohbu, *DESORPTION OF INDIUM DURING THE GROWTH OF GAAS/INGAAS/GAAS HETEROSTRUCTURES BY MOLECULAR-BEAM EPITAXY.* Japanese Journal of Applied Physics Part 1-Regular Papers Short Notes & Review Papers, 1992. **31**(10): p. 3277-3281.
57. Muraki, K., et al., *SURFACE SEGREGATION OF IN ATOMS DURING MOLECULAR-BEAM EPITAXY AND ITS INFLUENCE ON THE ENERGY-LEVELS IN INGAAS/GAAS QUANTUM-WELLS.* Applied Physics Letters, 1992. **61**(5): p. 557-559.
58. Froyen, S. and A. Zunger, *Surface segregation and ordering in III-V semiconductor alloys.* Physical Review B, 1996. **53**(8): p. 4570-4579.
59. Duplessis, J. and G.N. Vanwyk, *A MODEL FOR SURFACE SEGREGATION IN MULTICOMPONENT ALLOYS .2. COMMENT ON OTHER SEGREGATION ANALYSES.* Journal of Physics and Chemistry of Solids, 1988. **49**(12): p. 1451-1458.
60. Duplessis, J. and G.N. Vanwyk, *A MODEL FOR SURFACE SEGREGATION IN MULTICOMPONENT ALLOYS .5. THE KINETICS OF SURFACE SEGREGATION IN MULTICOMPONENT ALLOYS.* Journal of Physics and Chemistry of Solids, 1989. **50**(3): p. 251-257.

61. Gumen, L.N., et al., *Surface segregation of interacting atoms: analytical approach using a thermodynamic model.* Surface Science, 2000. **445**(2-3): p. 526-534.
62. Karpov, S.Y. and Y.N. Makarov, *Indium segregation kinetics in InGaAs ternary compounds.* Thin Solid Films, 2000. **380**(1-2): p. 71-74.
63. Martini, S., et al., *Real-time determination of the segregation strength of indium atoms in InGaAs layers grown by molecular-beam epitaxy.* Applied Physics Letters, 2002. **81**(15): p. 2863-2865.
64. People, R. and J.C. Bean, *BAND ALIGNMENTS OF COHERENTLY STRAINED GEXSI1-X/SI HETEROSTRUCTURES ON LESS-THAN-001-GREATER-THAN GEYSI1-Y SUBSTRATES.* Applied Physics Letters, 1986. **48**(8): p. 538-540.
65. Cullis, A.G., A.J. Pidduck, and M.T. Emeny. *Morphology and strain relief in the InGaAs/GaAs epitaxial system*. in *Institute-of-Physics Conference on Microscopy of Semiconducting Materials 1995*. 1995. Oxford, England: Iop Publishing Ltd.
66. Whaley, G. and P. Cohen, *Relaxation of strained InGaAs during molecular beam epitaxy.* Applied Physics Letters, 1990. **57**: p. 144.
67. Yoon, S.F., *SURFACE-ROUGHNESS OF STRAINED IN0.1GA0.9AS FILMS GROWN ON GAAS SUBSTRATES BY MOLECULAR-BEAM EPITAXY.* Thin Solid Films, 1993. **223**(2): p. 320-326.
68. Kavanagh, K.L., et al., *ASYMMETRIES IN DISLOCATION DENSITIES, SURFACE-MORPHOLOGY, AND STRAIN OF GAINAS/GAAS SINGLE HETEROLAYERS.* Journal of Applied Physics, 1988. **64**(10): p. 4843-4852.
69. Berger, P.R., et al., *ROLE OF STRAIN AND GROWTH-CONDITIONS ON THE GROWTH FRONT PROFILE OF INXGA1-XAS ON GAAS DURING THE PSEUDOMORPHIC GROWTH REGIME.* Applied Physics Letters, 1988. **53**(8): p. 684-686.
70. Price, G.L., *GROWTH OF HIGHLY STRAINED INGAAS ON GAAS.* Applied Physics Letters, 1988. **53**(14): p. 1288-1290.
71. Whaley, G.J. and P.I. Cohen, *THE GROWTH OF STRAINED INGAAS ON GAAS - KINETICS VERSUS ENERGETICS.* Journal of Vacuum Science & Technology B, 1988. **6**(2): p. 625-626.
72. Barvosa-Carter, W., et al., *Atomic scale structure of InAs(001)-(2 x 4) steady-state surfaces determined by scanning tunneling microscopy and density functional theory.* Surface Science, 2002. **499**(1): p. L129-L134.
73. Millunchick, J.M., et al., *Surface reconstructions of In-enriched InGaAs alloys.* Applied Physics Letters, 2003. **83**(7): p. 1361-1363.
74. Dehaese, O., X. Wallart, and F. Mollot, *KINETIC-MODEL OF ELEMENT-III SEGREGATION DURING MOLECULAR-BEAM*

EPITAXY OF III-III'-IV-SEMICONDUCTOR COMPOUNDS. Applied Physics Letters, 1995. **66**(1): p. 52-54.

75. Ohkouchi, S. and A. Gomyo, *Scanning tunneling microscopy observations of surface structures on ordered GaInAs layers grown on InP.* Applied Surface Science, 1998. **130**: p. 447-451.
76. Mori, T., et al., *Surface structure of InGaAs/InP(001) ordered alloy during and after growth.* Applied Surface Science, 2004. **237**(1-4): p. 230-234.
77. Vanhaesendonck, C., et al. *NANOLITHOGRAPHIC PATTERNING OF AU FILMS WITH A SCANNING TUNNELING MICROSCOPE*. in *3rd International Conference on Nanometer-Scale Science and Technology*. 1994. Denver, Co: Amer Inst Physics.
78. Wi, J.S., et al., *Guided formation of a sub-10 nm silicide dot array on an area patterned by electron-beam lithography.* Advanced Materials, 2007. **19**(21): p. 3469-+.
79. Aid, K., et al., *Atomic structure of the (2 x 4) In0.53Ga0.47As/InP(001) reconstructed surface. A study of average strain and growth temperature effects on the indium segregation.* Surface Science, 1999. **425**(2-3): p. 165-173.
80. Bickel, J.E., et al., *Atomic size mismatch strain induced surface reconstructions.* Applied Physics Letters, 2008. **92**(6): p. 3.
81. Li, A., F. Liu, and M.G. Lagally, *Equilibrium shape of two-dimensional islands under stress.* Physical Review Letters, 2000. **85**(9): p. 1922-1925.
82. Twesten, R.D. and J.M. Gibson, *MEASUREMENT OF SI(111) SURFACE STRESS BY A MICROSCOPIC TECHNIQUE.* Physical Review B, 1994. **50**(23): p. 17628-17631.
83. Bartelt, N.C., R.M. Tromp, and E.D. Williams, *STEP CAPILLARY WAVES AND EQUILIBRIUM ISLAND SHAPES ON SI(001).* Physical Review Letters, 1994. **73**(12): p. 1656-1659.
84. Pearson, C., et al., *Imaging the evolution of lateral composition modulation in strained alloy superlattices.* Physical Review Letters, 2004. **92**(5): p. 4.
85. Stranski, I. and L. Krastanov, *Theory of orientation separation of ionic crystals.* Sitzungsber. Akad. Wiss. Wien, Math.-Naturwiss. Kl., Abt. 2B, 1938. **146**: p. 797–810.
86. Bouville, M., J.M. Millunchick, and M.L. Falk, *Pit nucleation in the presence of three-dimensional islands during heteroepitaxial growth.* Physical Review B, 2004. **70**(23): p. 9.

87. Tersoff, J. and F.K. Legoues, *COMPETING RELAXATION MECHANISMS IN STRAINED LAYERS.* Physical Review Letters, 1994. **72**(22): p. 3570-3573.
88. Riposan, A., et al., *The effect of island density on pit nucleation in In0.27Ga0.73As/GaAs films.* Surface Science, 2003. **525**(1-3): p. 222-228.
89. Gray, J.L., R. Hull, and J.A. Floro, *Formation of one-dimensional surface grooves from pit instabilities in annealed SiGe/Si(100) epitaxial films.* Applied Physics Letters, 2004. **85**(15): p. 3253-3255.
90. Walther, T., et al., *Nature of the Stranski-Krastanow transition during epitaxy of InGaAs on GaAs.* Physical Review Letters, 2001. **86**(11): p. 2381-2384.
91. Cullis, A.G., et al., *Stranski-Krastanow transition and epitaxial island growth.* Physical Review B, 2002. **66**(8): p. 4.
92. Joyce, B.A., T.S. Jones, and J.G. Belk, *Reflection high-energy electron diffraction scanning tunneling microscopy study of InAs growth on the three low index orientations of GaAs: Two-dimensional versus three-dimensional growth and strain relaxation.* Journal of Vacuum Science & Technology B, 1998. **16**(4): p. 2373-2380.
93. Chokshi, N., M. Bouville, and J.M. Millunchick, *Pit formation during the morphological evolution of InGaAs/GaAs.* Journal of Crystal Growth, 2002. **236**(4): p. 563-571.
94. Riposan, A., et al. *Island and pit formation during growth and annealing of InGaAs/GaAs films*. in *Symposium on Current Issues in Heteroepitaxial Growth-Stress Relaxation and Self Assembly held at the 2001 MRS Fall Meeting*. 2001. Boston, Ma: Materials Research Society.
95. Jesson, D.E., M. Kastner, and B. Voigtlander, *Direct observation of subcritical fluctuations during the formation of strained semiconductor islands.* Physical Review Letters, 2000. **84**(2): p. 330-333.
96. Chokshi, N.S. and J.M. Millunchick, *Cooperative nucleation leading to ripple formation in InGaAs/GaAs films.* Applied Physics Letters, 2000. **76**(17): p. 2382-2384.
97. Vanderbilt, D. and L.K. Wickham. *ELASTIC ENERGIES OF COHERENT GERMANIUM ISLANDS ON SILICON*. in *Symp on the Evolution of Thin-Film and Surface Microstructure*. 1990. Boston, Ma.
98. Theis, W. and R.M. Tromp, *Nucleation in Si(001) homoepitaxial growth.* Physical Review Letters, 1996. **76**(15): p. 2770-2773.
99. Park, S.J., et al., *Surface morphology of InGaAs on GaAs(100) by chemical beam epitaxy using unprecracked monoethylarsine, triethylgallium and trimethylindium.* Surface Science, 1996. **350**(1-3): p. 221-228.

100. Kim, D.J., E.A. Everett, and H. Yang, *Annealing induced transition of flat strained InGaAs epilayers into three-dimensional islands.* Journal of Applied Physics, 2007. **101**(10).
101. Lee, H., et al., *Determination of the shape of self-organized InAs/GaAs quantum dots by reflection high energy electron diffraction.* Applied Physics Letters, 1998. **72**(7): p. 812-814.
102. Millunchick, J. and S. Barnett, *Suppression of strain relaxation and roughening of InGaAs on GaAs using ion-assisted molecular beam epitaxy.* Applied Physics Letters, 1994. **65**: p. 1136.
103. Glazov, V.M., A.S. Pashinkin, and L.M. Pavlova, *Thermal expansion and some characteristics of the interatomic bond strength in gallium and indium phosphides.* High Temperature, 2002. **40**(3): p. 369-378.